EFFECTS OF THE INTERNAL MAGNETIC FIELD ON THE MAGNETO-MECHANICAL PROPERTIES OF MAGNETIC SHAPE MEMORY ALLOYS

by

Anthony Hobza

A dissertation

submitted in partial fulfillment

of the requirements for the degree of

Doctor of Philosophy in Materials Science and Engineering

Boise State University

December 2017

BOISE STATE UNIVERSITY GRADUATE COLLEGE

DEFENSE COMMITTEE AND FINAL READING APPROVALS

of the dissertation submitted by

Anthony Hobza

Dissertation Title: Effects of the Internal Magnetic Field on the Magneto-Mechanical Properties of Magnetic Shape Memory Alloys

Date of Final Oral Examination: 26 July 2017

The following individuals read and discussed the dissertation submitted by student Anthony Hobza, and they evaluated his presentation and response to questions during the final oral examination. They found that the student passed the final oral examination.

Peter Müllner, Ph.D.	Chair, Supervisory Committee
Lan Li, Ph.D.	Member, Supervisory Committee
Charles B. Hanna, Ph.D.	Member, Supervisory Committee
Carlos J. García-Cervera, Ph.D.	Member, Supervisory Committee

The final reading approval of the dissertation was granted by Peter Müllner, Ph.D., Chair of the Supervisory Committee. The dissertation was approved by the Graduate College.

DEDICATION

I dedicate this work to my wife, Kelly, and daughter, Camille.

ACKNOWLEDGEMENTS

I would like to thank my advisor, Dr. Peter Müllner, who is a fantastic teacher and mentor. I would like to thank Dr. Paul Lindquist for help and guidance throughout my studies. I thank Dr. Nader Rafla and Dr. Kari Ullakko for their insight and contribution to my work.

I thank all members of the Müllner research group who have assisted my research and understanding, listed in no particular order: Link Patrick, Justina Freilich, Tammy Jackson, Andrew Armstrong, Brittany Muntifering, Nikki Kucza, Ted Lawrence, Jeff Huntsinger, Danielle Nichols, Eric Rhoads, Alex Mussel, Sam Barker, Miranda Buttram, Andrew Morrison, Brittni Blessie, Carl Rustad, Aaron Smith.

I thank Micron Technology and NanoSteel Corporation for donation of equipment. I thank Dr. Karthik Chinnathambi for help and training in characterization, and Phil Boysen for machining as well as donating parts to the torque apparatus.

I thank Idaho's Higher Education Research Council and the Micron School of Materials Science and Engineering for funding my studies.

ABSTRACT

Shape memory alloys are a class of functional material which recover from large strains without permanent deformation. The strain is accommodated by the displacement of twin boundaries in the martensite phase. The shape memory alloy Ni-Mn-Ga is also ferromagnetic. Ni-Mn-Ga preferentially magnetizes along a certain crystallographic axis. This direction of easy magnetization changes across twin boundaries, such that the directions in neighboring twin domains are nearly perpendicular.

The interaction of magnetic moments and interfaces including the crystal surface and twin boundary interfaces has a large role in the magnetization process of the material. The goal of this study is to characterize the relative influence of twin boundaries on the magnetization of the material, and the dependence of the magnetization on the twin domain microstructure.

The torque on a single crystal specimen in a homogeneous external magnetic field was characterized with experimental methods. The torque is the negative first derivative of the magnetic energy as a function of angle between the specimen and magnetic field. The torque and magnetic energy strongly depends on the twin domain microstructure. For specimen with two twin boundaries at 3% strain in an external magnetic field of 50 mT, one twin microstructure required 1.7 times more torque to rotate than another twin microstructure. At fields above 100 mT, the torque was asymmetric depending on the direction the direction the sample was rotated.

Numerical micromagnetic simulations were performed to gain a qualitative understanding of the difference in magnetization and magnetic energy in different twin microstructures. At low fields, the continuity of magnetization across the twin boundary results in one twin microstructure having completely saturated twin domains, while the other microstructures contained 180° magnetic domains. At larger fields, the asymmetry in torque was due to the angle of the twin boundary with the crystal surface.

Both the dependence on magnetization and torque asymmetry are due to the internal magnetic field at the twin boundary. The interaction of magnetic moments across the twin boundary drives the internal magnetic field and magnetization. The twin domain microstructure can be manipulated to drive the magnetization process in order to optimize the performance of the material in a device. The role of the internal magnetic field and specimen magnetization is discussed regarding a low power strain sensing measurement technique.

TABLE OF CONTENTS

DEDICATION iv

ACKNOWLEDGEMENTS v

ABSTRACT vi

LIST OF TABLES xii

LIST OF FIGURES xiii

LIST OF ABBREVIATIONS xx

CHAPTER ONE: INTRODUCTION 1

CHAPTER TWO: BACKGROUND 6

2.1 Magnetism 6

2.1.1 Exchange energy 7

2.1.2 Magnetocrystalline anisotropy energy 9

2.1.3 Zeeman (external field) energy 10

2.1.4 Stray field (internal field) energy 10

2.2 Micromagnetism 12

2.2.1 Background 12

2.2.2 Towards a mathematical description of micromagnetism 13

2.2.3 Dynamic equation for time-dependent magnetization 16

2.3 Micromagnetism of magnetic shape memory alloys 16

2.3.1 Analytical studies 18

2.3.2 Experimental studies 20
2.3.3 Numerical Modeling 25
2.4 Heusler alloys 28
2.4.1 Martensitic Structure 30
2.4.2 Twinning and Deformation 33
CHAPTER THREE: SENSING STRAIN WITH NI-MN-GA 37
3.1 Abstract 38
3.2 Introduction 39
3.3 Experimental Setup 41
3.4 Results 47
3.5 Analysis of Results 51
3.6 Discussion 54
3.7 Summary and Conclusion 58
3.8 Acknowledgements 59
3.9 References 59
CHAPTER FOUR: MAGNETIC TORQUE IN SINGLE CRYSTAL NI-MN-GA 62
4.1 Abstract 63
4.2 Introduction 63
4.3 Experimental Procedure 66
4.4 Results 70
4.5 Discussion 73
4.5.1 Zeeman Energy 75
4.5.2 Magnetocrystalline Anisotropy 77

4.5.3 Internal Field 79
4.5.4 Comparison of different energy contributions to magnetic torque ... 82
4.6 Conclusion 84
4.7 Acknowledgements 85
4.8 References 86
4.9 Supplemental Materials 87
CHAPTER FIVE: TWIN ENHANCED MAGNETIC TORQUE 93
5.1 Abstract 94
5.2 Introduction 94
5.3 Micromagnetism 97
5.4 Experimental Procedure 99
5.5 Micromagnetic Simulation 103
5.6 Experimental Results 105
5.7 Simulation Results 109
5.7.1 Two Twin Boundaries 109
5.7.2 Single Twin Boundary 114
5.8 Discussion 117
5.9 Conclusions 128
5.10 Acknowledgements 129
5.11 References 129
CHAPTER SIX: DISCUSSION 132
6.1 Strain Sensing 142
CHAPTER SEVEN: CONCLUSIONS AND OUTLOOK 146

References.....150

LIST OF TABLES

Table 2.1 Crystallographic positions for Ni, Mn and Ga elements in the austenitic Heusler structure shown in Figure 8. 29

Table 2.2 Twinning elements for compound twins in the tetragonal lattice and Type II twins in the monoclinic lattice of 10M Ni-Mn-Ga. For Type I twins, K_2 and η_1 are irrational, while for Type II twins, K_1 and η_2 are irrational [111] 35

Table 4.1 Torque contributions from the Zeeman energy, magnetocrystalline anisotropy energy, and shape anisotropy energy, as well as the measured torque. For relative strains of $\boldsymbol{\epsilon} = 0$, 0.5 and 1 the symbolic equation for each contribution is given along with the calculated maximum value, angle of maximum torque, and angle for which the torque vanishes. The angle refers to γ, which is the angle between the long axis of the sample and the magnetic field. The calculated values are given for an external field H_a = 75 mT, saturation magnetization M_s = 0.6 T, and magnetocrystalline anisotropy energy of K_u = 2.45 x 10^5 J/m^3. The torque values given are normalized by the volume, and have the units kNm/m^3 = kPa..... 82

Table 5.1 Numeric values of magnetic energy constants for 10M Ni-Mn-Ga for micromagnetic simulations 104

Table 5.2 Derivative of the specific torque as a function of γ near the equilibrium angle. The experimental results showed nearly linear (constant slope) increase in torque close to the equilibrium angle. A quadratic function was fit to the simulated energy. The second derivative of the quadratic function is a constant which gives the rate of change of the torque with increasing γ. 114

LIST OF FIGURES

Figure 2.1 Spontaneous alignment of magnetic moments in paramagnetic, ferromagnetic, and anti-ferromagnetic materials. 7

Figure 2.2: Ferrite oxide powder shows 180° magnetic domains through the interaction of the stray field with particles [44] 13

Figure 2.3: Landau and Lifshitz assumed a domain structure where domains were much larger than domain walls and closure domains preserved zero divergence of magnetization at the surface of the crystal [49]..... 14

Figure 2.4: Domain walls move in twin variants with AEM parallel to the magnetic field. Domain walls do not move in the variant with the AEM perpendicular to the magnetic field. The continuity of domain walls across the twin boundary is broken, which results in large stray field and internal field energy (volume magnetic charges due to magnetization divergence in the bulk) [74] 21

Figure 2.5: MOIF shows contrast between magnetic domains before mechanically-induced twin boundary motion (a,d) and after. Magnetic domain walls bend (b, e) to preserve continuity across the twin boundary when the twin boundary moves under mechanical stress. This also leads to magnetization divergence and a large stray field. To minimize the internal field energy, magnetic domains split into finer domains (c, f) [40,75]..... 22

Figure 2.6 (a) Topography of the thin film from AFM and (b) magnetic domains from MFM are shown along with the proposed structure of twin and magnetic domains (c). The authors calculated for the equilibrium magnetic domain width as a function of film thickness; the results agreed with experimental data (d) [61]..... 23

Figure 2.7 Transmission electron microscopy images of 180° domain walls viewed parallel to the AEM under external magnetic fields of -103 Oe (a), -201 Oe (b), and -480 Oe (c) [81] 24

Figure 2.8 Heusler phase of Ni-Mn-Ga. Ga atoms occupy corner and face centers (green), Mn atoms occupy edge sites (red), and Ni atoms (blue occupy each quadrant of the unit cell. 30

Figure 2.9 Martensitic transformation temperature (Ms) and Curie temperature (TC) for the different Ni-Mn-Ga alloys as a function of electron concentration (*e/a*). Diamonds represent the Curie temperatures of all alloys. Circles refer to alloys with 25 atomic % Mn, triangles to alloys with 21 atomic % Ga, and pluses to alloys with 50 atomic % Ni. Uncertainty for each symbol is shown by horizontal limiting bar. [100] 31

Figure 2.10 Martensite structure shown as a function of composition. Circles have 10M strucutre, triangles are mixed 10M/14M, and squares are 14M. Solid lines indicate martensite transformation temperatures and the dashed line indicates compositions with 50 atomic % Ni. Compositions were taken from Jin et al. [101]..... 31

Figure 2.11 Monoclinic distortion for alloys with 10M phase at 298 K as a function of martensitic transformation temperature. (a) Difference of parameters *a* and *b* and (b) deviation of the angle γ from 90° [105]..... 32

Figure 2.12 Twinning elements: K_1 is the invariant twinning plane with η_1 the twinning direction parallel to K_1., K_2 is the conjugate twinning plane with η_2 the conjugate twinning direction parallel to K_2. The shear plane *s* contains the twinning directions and intersects the twinning planes. [110]..... 34

Figure 3.1 Magneto-Mechanical Test Apparatus (MMTA) with a variable-field electromagnet (a), voice coil motor (b), linear-variable differential transformer (c), micrometer (d), piezoelectric force transducer (e), springs to tune the resonant frequency of the motor (f), and Ni-Mn-Ga specimen (g). 43

Figure 3.2 Difference in RMS output voltage as a function of drive frequency for a fully compressed and fully elongated sample in an external field of 0.4 T. The RMS output voltage has a maximum at 4 kHz, which was chosen as drive frequency for all experiments. 47

Figure 3.3 The root-mean-square of the raw voltage data from the pickup coil is shown (a) at a frequency of 50 Hz and stroke of 150 μm with an applied field of 0.4T. Time is calculated by applying a sampling rate factor to the sample number. A band-pass filter was applied to let through only the 4 kHz excitation voltage and suppress all noise components. The resulting voltage waveform shows an amplitude modulation with only the harmonics present in the sample strain (b). 48

Figure 3.4 The MatLab script applied a band-pass filter to both the input and output voltage data, and then calculated a running RMS for each voltage waveform (a). A ratio of the output RMS to input RMS is taken to account for the modulation of the input voltage waveform (b). The motor displacement was measured using the LVDT and the MatLab program

applied a low-pass filter with a 12 kHz cutoff frequency to suppress noise from the excitation voltage of the LVDT. Strain was calculated using the filtered LVDT signal, initial position of the LVDT and initial strain of the sample (c). The RMS Ratio was plotted against the strain to analyze the voltage-strain relationship of the measurement coils (d). 49

Figure 3.5 Stress vs. Strain curves recorded at 50 Hz, with 0.4 T applied field and stroke varying from 50 to 350 μm. Each loop contains data of ten full loading cycles. The piezoelectric force transducer measures relative stress, not absolute stress. The relative stress from the transducer was shifted to the appropriate compressive stress by performing a manual test using the compression from the LVDT and spring constant of springs in Figure 1. 50

Figure 3.6 RMS ratio vs. Strain was taken for magnetic fields from a maximum of 0.8 T down to 0.2 T. The inset shows the ratio range (maximum – minimum). The full scale of the ratio decreases with increasing perpendicular field. 52

Figure 3.7 As the frequency increases, the slope of the linear fit increases by 15% while the voltage intercept decreases by less than 2%. The dependence of the slope on the magnetic field is consistent across all frequencies tested, with slope increasing with magnetic field. The slop of the fit for 100 Hz at 0.3 T decreases because the magnetic field does not accelerate the strain of the sample as quickly as the motor unloads the sample..... 53

Figure 3.8 At a constant actuation frequency of 50 Hz and applied magnetic field of 0.4 T, the hysteresis in the RMS-strain relationship increases quadratically with increasing strain. 54

Figure 3.9 A sample is depicted containing one twin boundary and two twin domains, A and B, with axis of easy magnetization in the *x* and *y* direction, respectively. The external magnetic field is parallel to the *y* direction, and the axis of the coils is parallel to the *x* direction. The external magnetic field causes the magnetic moments in domain A to rotate at an angle α away from the axis of easy magnetization. 56

Figure 4.1 The magnetic samples (a) were placed in a round Teflon sample holder (b). The sample holder had a shoulder machined to press-fit into the inner bore of a non-magnetic ZrO2 ceramic bearing (c). A groove was machined at the circumference and a string (d) was wrapped around the sample holder in this groove. The string was connected to a spring force gauge (not shown) to apply a tangential force (torque) to the sample holder and sample. 67

Figure 4.2 (a) A digital image was captured using a Canon PowerShot A3000 digital camera. A compass was placed in between the poles of the electromagnet.

The North-South pole aligned parallel to the magnetic field, and the East-West pole was perpendicular to the magnetic field. Using the angle tool in ImageJ, the angle γ between the poles of the compass and the *x* axis of the sample was measured. The magnetic field direction is the reference direction and γ increases clock wise. (b) White lines highlight the kink between adjacent domains. Lines across the sample connect the kinks on the surfaces and indicate the location of twin boundaries. Thick white lines in each domain denote the direction of the easy axis of magnetization.... 68

Figure 4.3 Equilibrium angle γ_{eq} between the sample's long axis and magnetic field as a function of strain at different magnetic fields. At 100 mT, twin boundaries moved for strains higher than 3% and so data past 3% was not obtained. The arrow shows the strain for the data point at 3% strain and 100 mT may have decreased, changing the equilibrium angle. Equation 7 is plotted as a dashed line..... 71

Figure 4.4 (a) Torque as a function of angle γ between the sample's long axis and magnetic field at 6% strain for different applied magnetic fields. (b) Interpolated torque values from empirically fit equations as a function of external field at -75°, -60°, and -45°..... 72

Figure 4.5 Torque as a function of angle γ between the sample's long axis and magnetic field at 75 mT applied field for different values of strain. The maximum measured torque decreased by a factor of 6 from 0% to 6% strain..... 72

Figure 4.6 A magnetic material subjected to an external magnetic field at an angle γ to the sample edge experiences a magnetization M at an angle α to the sample edge..... 75

Figure 4.7 Specimen containing two domains, A and B, with easy axis of magnetization parallel to the *x* and *y* directions, respectively. As the strain is increased, the fraction of domain B increases and domain A shrinks... 76

Figure 4.8 Torque in a field of 25, 50, and 100 mT as a function of angle γ between the magnetic field and the direction of the long axis of the sample for (a) the Alnico 8 permanent magnet and (b) the soft magnetic iron. The permanent magnet (a) rotated by much more than the soft iron (b) because the permanent magnet had only one equilibrium angle at $\gamma = 0°$ while the soft iron had two equilibrium angles at $\gamma = 0°$ and 180°. The main torque contributor in the permanent magnet is the Zeeman energy, while in the soft iron it is the shape anisotropy energy. 88

Figure 5.1 The platform of the experimental apparatus was made from a nylon block which was press fit in between the pole pieces of the electromagnet. (a) Two ceramic bearings were press fit into the nylon block. The inner

diameters of the bearings guided the shaft of the Teflon sample holder into the optical encoder wheel, which was attached with a set screw. The Ni-Mn-Ga sample was laid in a groove on the sample holder. A groove was cut around the circumference of the sample holder, into which a string was tied and wrapped to apply the torque. (b) The initial angle, γ, of the sample to the external magnetic field was determined by comparing the edge of the sample to the angle of a compass deflected by the magnetic field. .. 100

Figure 5.2 A sample containing two twin boundaries may have either microstructure, denoted by "ABA" (a) or "BAB" (b). The axis of easy magnetization is parallel and perpendicular to the lateral surface in twin domains A and B, respectively. 101

Figure 5.3 Experimental results for the maximum specific torque as a function of strain for a single twin as well as ABA and BAB twin microstructures at an external field of 50 mT (a). The equilibrium angle is shown as a function of sample strain (b). Results for the ABA and BAB microstructures are denoted with blue stars and open green circles, respectively. Results for samples with a single twin boundary are shown in solid maroon squares..... 106

Figure 5.4 Experimental data for the normalized torque as a function of the change in γ from the equilibrium angle for a sample with one twin boundary at 2% strain (a). Data is given for 100 mT, 200 mT, 500 mT, 1000 mT, and 1500 mT in both the positive and negative g directions. Positive γ is in the clockwise direction, and negative γ is the counterclockwise direction. For magnetic fields above 200 mT, the torque decreased after ~15° rotation in the clockwise direction. The sample holder spun to a new angle, hence the abrupt jump in angle. The decrease in torque is shown in (b) for 500 mT. The jumps in angle represent show the bifurcation, since the stimulus to the sample was torque and there are multiple possible angles at the same torque. The dotted black line approximates the torque in the intermediate angle range. The sample for 2% strain is shown, containing the location of the twin boundary (dashed blue line) at the equilibrium angle at a magnetic field of 50 mT(c). 108

Figure 5.5 Experimental results for the equilibrium angle as a function of external magnetic field for a sample with one twin boundary at 2% strain (a) and 4% strain (b). Dashed lines indicate the equilibrium angles for the fields plotted in Figure 5.4a. At fields 250 mT and larger, two unique equilibrium angles existed for the sample at 4% strain. 109

Figure 5.6 Simulation results for the magnetic energy as a function of angle is given for the ABA twin structure at a strain of 3%. The total energy is given as a function of -γ (a) and separated in its contributions in (b) as a difference to

its respective minimum value. The equilibrium magnetic domain structure is shown for -γ = 30 ° (c) and -γ = 80 ° (d). 110

Figure 5.7 Simulation results for the ABA twin microstructure giving the total area of the blue and green magnetic domains (a) and the net magnetization (b) plotted against -γ. 111

Figure 5.8 Simulated results for the change in total energy with respect to the minimum energy is given as a function of -γ for the ABA and BAB microstructures (a) along with the equilibrium magnetic domain structure at an angle of $-\gamma$ = 30° (b). The ABA microstructure (top) has 180° magnetic domains in both twin domains, while the BAB microstructure (bottom) has fully saturated domains. The simulated samples are both at 3% strain with an external magnetic field of 75 mT..... 113

Figure 5.9 The total energy is given as a function of -γ (a) along with the equilibrium magnetic structure at the lowest energy for a sample at 3% strain and 75 mT with one twin boundary (a). The magnetic domain structure at -γ = 20° (b) shows a fully saturated A twin domain while the B twin domain has two demagnetizing 180° magnetic domains which extend from lateral surface to lateral surface without intersecting the twin boundary. To avoid intersecting the twin boundary, the outermost left 180° magnetic domain curves to the right..... 115

Figure 5.10 Simulated results for the energy as a function of γ at 2% strain and 500 mT for a sample with one twin boundary (a). The arrows mark the bifurcation of the stable position under torque as displayed in Figrue 4b. The change in magnetization normal to the twin boundary (b) and the divergence of the magnetization normal to the twin boundary (c) are given as a function of γ. The change in energy from the minimum for each individual energy component is given as a function of γ (d). 117

Figure 6.1 A schematic of magnetic domain nucleation in the BAB twin microstructure with a continuous magnetic domain wall. If a small demagnetizing magnetic domain nucleates in the left B twin domain, 180° magnetic domain with large area must also nucleate in the A domain and in the right B twin domain. 134

Figure 6.2 The change in perpendicular magnetization (a) at the twin boundary and the divergence of the magnetization (b) are given as a function of gamma. The units of magnetization are the normalized magnitude of the magnetic vector. The simulation was done for a sample at 2% strain containing one twin boundary in an external magnetic field of 500 mT. While the change in magnetization perpendicular to the twin boundary is nearly symmetric about γ = 0°, the divergence has an absolute minimum near γ = -45° and a maximum near γ = +45°..... 136

Figure 6.3 Simulation results for the magnetization of a sample with one twin boundary at 2% strain in an external magnetic field of 500 mT is given for $\gamma = +40°$ (a) and $\gamma = -40°$ (b). For $\gamma = +40°$, the external magnetic field is nearly parallel to the twin boundary and the divergence of the magnetization at the twin boundary is close to a maximum (Figure 6.2b). At $\gamma = -40°$ the external magnetic field is nearly perpendicular to the external magnetic field and the divergence of mangetization is nearly zero. For both angles, the direction of magnetic vectors across the twin boundary are shown in a location denoted by the red box in the color plot. 137

Figure 6.4 A sample containing one twin boundary at 3% strain in an external field of 75 mT at an angle of $\gamma = -30°$ 139

Figure 6.5 The maximum torque as a function of external magnetic field for a sample with one twin boundary at 3 different strains. 139

Figure 6.6 The demagnetizing factor for twin domain A in a single twin boundary specimen is given as a function of sample strain. At 0% strain, the sample contains only twin domain A, and at 6% strain twin domain A does not exist. The demagnetizing factor and stray field increase with increasing strain. The demagnetizing factor was calculated based on the continuous function given by Equation 1 in Ref. 118. 144

Figure 7.1 A sample containing two non-parallel twin boundaries would have a large divergence in magnetization at one twin boundary, depicted by negative signs on the right twin boundary. 148

LIST OF ABBREVIATIONS

Å	Angstroms
AEM	Axis of easy magnetization
AFM	Atomic force microscopy
Al	Aluminum
APB	Anti-phase boundary
B	Bain distortion
$\mathbf{B}$	Magnetic flux density
C_{ex}	Exchange energy constant
Cu	Copper
E_{anis}	Magnetocrystalline anisotropy energy
E_{ex}	Exchange Energy
e/a	Electrons per atom
Ga	Gallium
$\boldsymbol{\mathcal{H}}$	Effective magnetic field vector
$\mathbf{H_{int}}$	Internal magnetic field vector
$\mathbf{H_e}$	External magnetic field vector
J	Joules
K	Kelvin
K_u	Magnetocrystalline anisotropy energy constant
m	Meter

m	Magnetic vector
M	Net magnetization vector
M_s	Saturation magnetization
meV	milli-Electron volts
MFIS	Magnetic field induced strain
MFM	Magnetic force microscopy
Mn	Manganese
MOIF	Magneto optical indicator foil
MPa	Mega-Pascal
Ms	Martensite transformation start temperature
mT	milli-Tesla
N_d	Demagnetization factor
Ni	Nickel
Oe	Oersted
$\mathbf{P_1}$	Invariant plane strain
$\mathbf{P_2}$	Lattice invariant shear
R	Rotation
s	Shear plane
S	Magnetic moment magnitude
SMAs	Shape memory alloys
TC	Curie temperature
W	Spin wave stiffness
V	Volume

α	Damping factor
γ_0	Gyromagnetic ratio
K_1	Invariant twinning plane
K_2	Conjugate twinning plane
η_1	Twinning direction
η_2	Conjugate twinning direction

CHAPTER ONE: INTRODUCTION

Magnetic energy is the driving force for twin boundary motion in magnetic shape memory alloys. The internal magnetic field due to material and twin boundary interfaces is, generally, vastly oversimplified or ignored in the analysis of magnetic energy. This research aims to characterize the influence of the internal magnetic field. The goal of this research is to investigate the influence of the internal magnetic field on the magnetic energy and magnetization of a single crystal of the magnetic shape memory alloy Ni-Mn-Ga. The study characterizes the dependence of the magnetization and internal magnetic field on twin domain microstructure using experimental techniques and numerical simulations.

Shape memory alloys (SMAs) are a class of functional materials which have large reversible strains. Thermally activated SMAs such as NiTi strain by deformation in the martensite phase. Recovery occurs by heating the martensite through the transformation temperature to the austenite phase. In the austenite phase, the material returns to its original shape it had prior to deformation.

Chernenko *et al.* thought that, in ferromagnetic martensites, the thermoelastic strains of SMAs could be replicated with the application of a magnetic field [1]. In 1996, Ullakko *et al.* reported a magnetic field induced strain (MFIS) of 0.2% in a single crystal of off-stoichiometric Ni-Mn-Ga [2]. Murray *et al.* reported an increased MFIS of 6% in 2000 [3], and MFIS was increased to 9.6% in 2002 by tuning the composition and

microstructural training [4,5]. Through the addition of a small fraction of cobalt and copper, Sozinov *et al.* reported MFIS of 12% in 2013 [6].

Actuation in magnetic shape memory alloys is not limited by kinetics of heat transfer as in thermally activated SMAs [7]; MFIS can occur at kHz frequencies [8-10]. The recoverable strain is two orders of magnitude larger than the largest strain of magnetostrictive materials, such as Terfenol-D, which strain at up to 0.24% [11]and piezoelectric materials which strain at 0.1% [12]. Fast actuation and large stroke alloy MSMAs the potential for application in actuators [2,4,13], sensors [14-16], and energy harvesting devices [15-17].

The martensite phase of MSMAs has an anisotropic crystallographic lattice with a magnetic moment tied strongly to one crystallographic direction termed the axis of easy magnetization. This crystallographic direction changes across twin boundaries. A magnetic field or mechanical stress energetically favors a certain twin domain. Twin boundaries move to increase the volume fraction of this twin domain.

The magnetic and mechanical properties of Ni-Mn-Ga shape memory alloys are highly sensitive to twin microstructure. Single crystals of Ni-Mn-Ga with densely twinned microstructure achieve a long fatigue life but at limited stroke, while samples with coarsely twinned microstructures achieve near maximum stroke but have a short lifetime [18-21]. The twin microstructure also affects the twinning stress [22] as well as the critical field required to induce MFIS [23].

The magneto-mechanical response also depends on the specimen shape. Specimen with a large length to width ratio tend to bend when an external magnetic field is applied perpendicular to the sample length [24-26]. Bending was first reported in 2001 on a thin

film in an inhomogeneous magnetic field [26]. Zheng *et al.* reported bending in an oligocrystalline wire sample in a homogeneous field, and attributed the bending to magnetic field induced torque [25]. Kucza *et al.* demonstrated the increase in bending strain with increasing length to width ratio in a single crystal [24]. The authors qualitatively explained the torque induced bending with the interplay between the magnetic energies which occur in a ferromagnetic material in a magnetic field.

Just as the mechanical properties depend on the complex twin domain microstructure, the magneto-mechanics depend additionally on the complex magnetic microstructure. Magnetic energies have been used to describe the driving force for MFIS [4,27-29] and the magneto-mechanical response of Ni-Mn-Ga in a magnetic field and under mechanical stress [30-32]. The critical field required to induce twin boundary motion depends on the relative magnetic energies of neighboring twin domains. Analogously, the electromagnetic energy harvested depends on the change in magnetic energy as the twin boundaries move.

Magnetic energy calculations are based on physical models representing the structure of twin boundaries and magnetic domains. The magnetic energies used in the analytical calculations vary; some only include Zeeman and magnetocrystalline anisotropy [4,28,33] while others include these as well as the stray field energy [23,34,35] or exchange energy [36,37] but not both. The complexity of the magnetic structure in the physical models varies as well, some take into account magnetization rotation [4,38] and some include magnetic domains [38,39]. Models which include magnetic domains force domain wall continuity across a twin boundary [34,38,39]. This minimizes the divergence in magnetization and internal field (Section 2.1.4) at the twin

boundary, but the domain structure in real specimen may deviate from such a configuration when exposed to a magnetic field [40].

The interaction of magnetization, twin boundaries, and the specimen shape determine the behavior in a magnetic field. A detailed understanding of the magnetic energy is required in order to quantitatively predict magneto-mechanical properties. The magnetic energy is not adequately described by assuming homogeneous magnetization in twin domains, or continuous magnetic domain walls. A bending specimen presents a complex system with multiple twin boundaries which are not necessarily parallel. The angle between the axis of easy magnetization and magnetic field varies across the length of the sample. An understanding of the interaction between magnetic and twin domain structures would benefit analysis and design.

This study aims to qualitatively describe the interaction of magnetic and twin domain structure and the effect on magnetic energy using both experimental methods and numerical micromagnetic simulations. This study investigates this interaction and the role of each type of magnetic energy as it relates to the torque in systematic experiments with a single crystal with defined twin boundary microstructures. The study shows that different twin domain microstructures magnetize differently. In a sample with two twin boundaries, equivalent strain and magnetic field, simulations showed that one microsctructure had fully saturated twin domains while the other contained 180° magnetic domains. I argue that designers should target a specific twin microstructure to optimize the performance of the material in a device. The twin domain microstructure is never accounted for in device design, but represents an important and easily manipulated

variable. Based on the results of these studies we interpret experiments in a setting relevant to sensing applications.

As a result of this research, I will publish three first author papers and two papers on which I am a co-author. These results have been presented in a poster at the annual spring meeting of The Minerals, Metals and Materials Society in February 2017 and in a talk at the International Conference on Martensitic Transformations in July 2017.

CHAPTER TWO: BACKGROUND

2.1 Magnetism

Magnetic fields are created by moving charges. In the Bohr model of an atom, electrons orbit around the nucleus. The moving electrons create a magnetic field, which is quantified by their angular momentum and has a direction based on the sign of the electron spin. The local magnetic field is viewed as a magnetic moment with a magnitude described in terms of Bohr magnetons, which is the magnitude of the magnetic moment of a hydrogen atom.

There exist four main classes of materials with respect to the spontaneous alignment of magnetic moments. Paramagnetic materials have a random alignment of magnetic moments and magnetize weakly in an external magnetic field. Diamagnetic materials have no magnetic moment. Here, a magnetic field evokes a magnetic field antiparallel to an external magnetic field due to eddy currents. Ferromagnetic materials have magnetic moments aligned mutually parallel, a result of an exchange interaction. Antiferromagnetic materials have neighboring magnetic moments which align antiparallel. An illustration of the spontaneous alignment of magnetic moments in paramagnetic, ferromagnetic and anti-ferromagnetic materials is given in Figure 2.1.

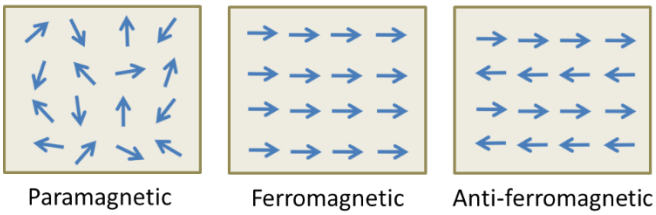

Figure 2.1 Spontaneous alignment of magnetic moments in paramagnetic, ferromagnetic, and anti-ferromagnetic materials.

2.1.1 Exchange energy

The exchange interaction is a quantum mechanical interaction which includes both the normal Coulomb interaction as well as the Pauli exclusion principle. The exchange interaction is described with the exchange integral, which gives information about the relative proximity of electrons to each other. The Hamiltonian operator for the exchange interaction in a two-electron system is given in Equation 1.

$$\hat{H}_{ex} = -2J_{ex}\hat{S}_1\hat{S}_2 \tag{2.1}$$

J_{ex} is the exchange integral; $\hat{S}_1$ and $\hat{S}_2$ are the spin operators for electrons 1 and 2. The spin can be positive or negative. Depending on the sign of the exchange integral, energy is minimized for either same or opposite spins. If the exchange integral is positive, energy is minimized for parallel spins. If the spins of neighboring electrons are parallel, the material is ferromagnetic. At some temperature, called the Curie temperature (*TC*), the energy is minimized by increasing the entropy of the system. The Curie temperature describes the transition from ordered magnetic moments to disordered magnetic moments, or the material transition to paramagnetism.

In ferromagnetic materials, the exchange energy has a minimum when the moments align parallel. The exchange energy depends on the relative orientation between neighboring magnetic moments. The exchange energy in ferromagnetic materials is typically represented as an energy penalty when moments are not parallel. The exchange

energy, E_{ex}, is given by an energy constant, C_{ex}, calculated from the exchange integral (derived from quantum mechanics) multiplied by the square of the gradient of magnetization **M** integrated over the entire sample volume (V):

$$E_{ex} = C_{ex} \int_V |\nabla \mathbf{M}|^2 \, dV \tag{2.2}$$

If moments are parallel, the gradient is zero and the exchange energy is minimal. If the gradient is non-zero, the deviation from parallel alignment increases the energy. The energy is minimized for parallel alignment and maximized for anti-parallel alignment. Equation (2.2) is computed over the entire sample volume to find the total exchange energy.

The exchange energy works to keep magnetic moments aligned in parallel. This is sometimes referred to as exchange "stiffness". Equation 2.2 is analogous to the energy of a spring, which is proportional to the square of the absolute deformation of the spring and the spring constant. The exchange energy constant C_{ex} corresponds to the spring constant. A larger exchange energy constant means a "stiffer" spring, or stronger interaction between neighboring magnetic moments.

Spin waves describe the time-dependent fluctuation in the direction of neighboring magnetic moments. Magnon is the term for a quantized spin wave. Magnons are analogous to phonons. Phonons are waves which describe fluctuation in the distance between atoms, magnons describe fluctuation in the orientation of magnetic moments. The probability distribution of magnons can be measured with neutron diffraction [41], from which a spin wave stiffness is derived. The spin wave stiffness can be used to calculate, experimentally, the exchange constant with Equation (2.3).

$$C_{ex} = \frac{WSN}{2V} \tag{2.3}$$

W is the spin wave stiffness, *S* is the magnitude of magnetic moments in Bohr magnetons, *N* is the number of magnetic moments per unit cell, and *V* is the volume of the unit cell.

2.1.2 Magnetocrystalline anisotropy energy

The crystallographic lattice of the material causes magnetic anisotropy. The magnetocrystalline anisotropy refers to the preference of alignment of magnetic moments in different crystallographic directions. The energy required to rotate the magnetic moment perpendicular to the axis of easy magnetization (AEM) is the magnetocrystalline anisotropy energy. When the magnetic moment lies in the AEM the energy is minimal. As the moment rotates away from the AEM the energy increases to a maximum perpendicular to the AEM.

Uniaxial symmetry is the simplest case where a material has only one AEM. The energy has even symmetry and can be expressed as an expansion with the form $E_{anis} = K_0 + K_1 \sin^2\varphi + K_2 \sin^4\varphi + K_3 \sin^6\varphi$. Typically, only K_1 and K_2 are needed to adequately describe the energy. The angle φ is the angle between the magnetic moment and the axis of easy magnetization. In the case of cubic anisotropy each of the three principal directions, <100>, <110>, and <111> are AEMs with different anisotropy energy constants.

The 10M modulated martensite phase of Ni-Mn-Ga has a nearly tetragonal lattice, and uniaxial magnetocrystalling anisotropy; the martensitic phase has one axis of easy magnetization coinciding with the crystallographic *c*-axis of the tetragonal lattice. The magnetocrystalline anisotropy energy constant (K_u) has been measured [42,43]; for

calculations, we use a value of 2.45 x 10^5 J/m^3 [43]. The magnetocrystalline anisotropy energy is calculated as

$$E_{anis} = \int_V K_u \sin^2\varphi \, dV \tag{2.4}$$

2.1.3 Zeeman (external field) energy

In an external magnetic field, the minimum energy occurs when a magnetic moment is parallel to the external field. The Zeeman energy gives the energy of a magnetic moment in an external field

$$E_z = -\mu_0 \mathbf{M} \cdot \mathbf{H}_{\text{ext}} \tag{2.5}$$

M is the net magnetization of a specimen, μ_0 is the magnetic permeability of free space, and $\mathbf{H_{ext}}$ is the external field. The Zeeman energy is often called external field energy. The dot product in Equation (2.5) is maximal when $\mathbf{M} \| \mathbf{H_{ext}}$. Magnetic moments rotate to align in parallel to the magnetic field in order to minimize the Zeeman energy.

2.1.4 Stray field (internal field) energy

If moments align such that a specimen has a net magnetization, the specimen creates a magnetic field. The magnetic field can be visualized with filings as demonstrated in the experiments of Bitter [44]. The net magnetization also creates a magnetic field internal to the specimen, in the opposite direction of the net magnetization. The stray field energy associated with magnetic moments of a magnetized specimen in its own internal field is positive (Equation 2.6).

$$E_s = \frac{\mu_0}{2} \int_V |\nabla U|^2 \, dV \tag{2.6}$$

The stray field energy E_s is the square of the gradient of the magnetic potential, U. The energy due to the internal field is analogous to the energy of an electric dipole in an electric field. The method for calculating this energy is to find the internal field, then

apply Equation (4.5) using H_{int} instead of H_{ext}. Poisson's equation in electrostatics relates the potential field with an electric charge density. Magnetostatics is an analogous situation where the magnetic potential U is related to an effective magnetic charge density ρ by the Poisson relation given in Equation 4.7.

$$\nabla^2 U = \rho \tag{2.7}$$

The charge density ρ is either a surface charge density due to a normal component of the magnetization at the surface or a volume charge density due to a divergence of magnetization in the bulk of the specimen.

Given the Maxwell relations

$$\mathbf{B} = \mu_0(\mathbf{M} + \mathbf{H}) \tag{2.8}$$

and

$$\nabla \cdot \mathbf{B} = 0 \tag{2.9}$$

then

$$\nabla \cdot \mathbf{H} = -\nabla \cdot \mathbf{M} = -\rho \tag{2.10}$$

H is sum of the external and internal magnetic fields. The internal magnetic field is calculated by

$$\mathbf{H_{int}} = -\nabla U \tag{2.11}$$

where $\mathbf{H_{int}}$ is the internal field. This calculation is true because $\nabla \times \mathbf{H_{int}} = 0$. $\mathbf{H_{int}}$ results from a divergence of magnetization in the bulk of the crystal, or from a component of the magnetization normal to the crystal surface.

Often, the internal field is described in terms of a demagnetizing field, which has a magnitude $N_d M$, where M is the average magnetization and N_d is a geometry-dependent factor for each Cartesian coordinate such that

$$N_x + N_y + N_z = 1 \tag{2.12}$$

The factor N_d is largest for the direction normal to the specimen face with the largest area. This approach assumes a homogeneous magnetization. It captures the interaction of magnetization normal to the surface but ignores magnetization divergence in the bulk and magnetic domains.

2.2 Micromagnetism

2.2.1 Background

Micromagnetism refers to the study of magnetism between the 1 nm and 1 μm length scales. Below 1 nm, quantum mechanics solves for the fundamental magnetic properties of a material (exchange energy, Curie temperature) using interactions of electrons in overlapping wavefunctions of neighboring atoms. Above the length scale of micromagnetism, domain theory describes the structure and configuration of domains assuming homogeneous saturation of each domain. For most practical situations, it is impossible to find a closed form analytical expression for the magnetization of a material. Computational methods are carried out such that the continuum conditions of Maxwell's equations are preserved across interfaces, or energy calculations are done over a vector matrix of magnetic moments.

In micromagnetism, we assign a net magnetization vector to each mesoscopic volume element. We use relevant energy terms of mesoscopic magnetic vectors to find the free energy related to magnetization in a material. Micromagnetic principles are applied to ferromagnetic materials to find the internal magnetic structure of domains and domain walls. Energy minimization schemes are combined with dynamic magnetization behavior described with the Landau-Lifshitz-Gilbert equation to minimize the total free

energy. This gives the equilibrium structure of mesoscopic magnetic vectors in a specimen.

In 1907 Weiss suggested the theory of domains we know today, where sections of material are homogeneously magnetized [45]. Weiss postulated neighboring magnetic moments were held in parallel by the "Weiss field". The origin of this field was explained by quantum mechanics with the exchange energy in 1926 [46,47].

In the 1930s, Sixtus demonstrated experimentally the nucleation of magnetic domains in nickel wires [48] and Bitter showed the geometry of magnetic structures on the surface of bulk cobalt [44]. Bitter mixed ferrite oxide powder into a colloidal suspension and poured the solution over the surface of cobalt. The stray field from neighboring magnetic domains forced the magnetic particles to form patterns displaying the domain structure (Figure 2.2).

Figure 2.2 Ferrite oxide powder shows 180° magnetic domains through the interaction of the stray field with particles [44]

2.2.2 Towards a mathematical description of micromagnetism

In 1935, Landau and Lifshitz published the seminal paper laying the foundation for micromagnetic energy calculations [49]. The paper attempted to describe the

difference in magnetic permeability depending on the relative orientation of the external magnetic field and domain walls. The authors achieved a few milestones in the paper. They combined the exchange and magnetocrystalline anisotropy energies to describe the width and energy of a domain wall. In order to minimize the internal field energy, the authors constructed a domain configuration which included closure domains (Figure 2.3). Also, by combining the internal field energy with the domain wall energy, the authors derived an equilibrium size for magnetic domains. This allowed them to show the shape of domains is plate-like, rather than thread or needle-like as other researchers hypothesized [50,51]. Finally, the authors derived a time-dependent equation for magnetization, known as the Landau-Lifshitz equation.

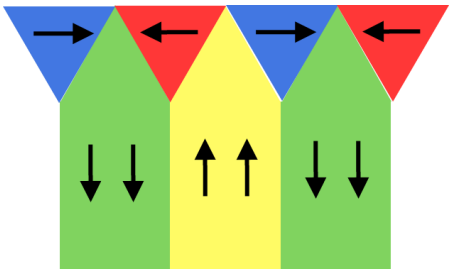

Figure 2.3 Landau and Lifshitz assumed a domain structure where domains were much larger than domain walls and closure domains preserved zero divergence of magnetization at the surface of the crystal [49]

Landau and Lifshitz still failed to include the internal field energy in their calculations. They assumed that, by constructing an equilibrium magnetic domain structure, the stray field energy approached zero and could be ignored. The Stoner-Wohlfarth model was proposed in 1948 [52]. The model assumed that all magnetic moments align in parallel, *i.e.* no closure domains exist. The model made it possible to analytically find an expression for the magnetization since the internal field energy can be calculated for a homogeneously magnetized particle.

The assumption of homogeneous magnetization made it possible to explicitly solve for the internal field energy by defining a geometry-dependent demagnetizing field. With an analytical expression, Stoner and Wohlfarth calculated the coercive field and the remanence of a magnetized particle [52] However, in 1938 Elmore experimentally showed the existence of domains on the surface of a particle in an external magnetic field thought large enough to saturate [53]. It turned out that the basic assumption of homogeneous magnetization is inherently false except for very small particles. The criteria for uniform magnetization and a closed form expression for magnetization was still elusive.

Scientists create a physical model, such as the Stoner-Wohlfarth model, on which they base analytical expressions. The model assumes homogeneous magnetization, which restricts the magnetic microstructure available to the system, *i.e.* magnetic domains. Often, the assumptions of a physical model are not revisited to re-asses these restrictions indeed minimize the energy. This problem dates back to the seminal investigation of micromagnetic energy by Landau and Lifshitz [49]. The authors created a magnetic microstructure which included closure domains to minimize the internal field energy. Further calculations were done without considering this energy, although by calculating the time dependent magnetization the internal field energy would inherently increase. The Stoner-Wohlfarth model assumes a homogeneously magnetized particle, but this assumption is only valid in a very small range of particle sizes.

The father of micromagnetism, William F. Brown, was critical of those approaches which assume a magnetic microstructure [54]. In 1957, Brown created the theory of nucleation fields and found a solution to the criteria for uniform magnetization

[55]. Brown analytically calculated the size range where a particle magnetizes homogeneously. Within short time, the few analytically accessible problems were solved. It was not until 1987 that computational methods were powerful enough to solve more complex micromagnetic problems [56].

2.2.3 Dynamic equation for time-dependent magnetization

The Landau-Lifshitz equation [49] gives the time-dependent magnetization:

$$\frac{d\mathbf{m}}{dt} = \gamma_0 \mathbf{m} \times \boldsymbol{\mathcal{H}} - \frac{\alpha\gamma_0}{M_s} \mathbf{m} \times (\mathbf{m} \times \boldsymbol{\mathcal{H}}) \tag{2.13}$$

The vectors **m** and $\boldsymbol{\mathcal{H}}$ are the magnetic moment and effective magnetic field, respectively. The constant α is the damping coefficient and γ_0 is the gyromagnetic ratio. The effective magnetic field is computed from the free energy functional (sum of all energy contributions)

$$\boldsymbol{\mathcal{H}} = -\frac{\delta E}{\delta M} = \frac{2C_{ex}}{M_S^2} |\nabla \mathbf{M}|^2 - \frac{2K_u}{M_S^2} (M_2 + M_3) + \mu_0 \mathbf{H}_\mathrm{e} - \mu_0 \nabla U \tag{2.14}$$

M_2 and M_3 are the components of the magnetic moment in the *y* and *z* directions, respectively, and M_s is the saturation magnetization. The above equations are given at a temperature of 0 K and for uniaxial magnetocrystalline anisotropy. For temperatures above absolute zero, a term representing thermal fluctuations could be added on the right side of Equation (2.14). This would account for thermal fluctuations in the direction of magnetic moments to the effective magnetic field. We assume here that the temperature is well below the Curie temperature such that the thermal energy does not significantly contribute to the orientation of magnetic moments.

2.3 Micromagnetism of magnetic shape memory alloys

Magnetic shape memory alloys present a unique situation for the applications of micromagnetics due to a combination of their magnetic properties. MSMAs such as Ni-

Mn-Ga are magnetically soft with low coercivity (~5 mT) and large uniaxial magnetocrystalline anisotropy ($K > 10^5$ J/m^3) [43]. MSMAs contain twin boundaries across which the AEM changes direction by approximately 90°. Thus, twin boundaries define 90° domain walls, which move when the material strains.

Magnetic properties of MSMAs have been studied thoroughly. For Ni-Mn-Ga alloys, reported values for the magnetocrystalline anisotropy energy range from 0.9 x 10^5 to 2.45 x 10^5 J/m^3 at room temperature [57]. Heczko *et al.* reported the temperature dependence of the magnetic anisotropy of 10M Ni-Mn-Ga ranging from 1.5 x 10^5 J/m^3 to 2.65 x 10^5 J/ m^3 for temperatures from 317 K to 130 K [58]. The authors found the anisotropy energy decreased steeply as the temperature approached the Austenite transformation temperature. The anisotropy energy increased as the temperature decreased; and additional inter-martensitic transformation occurred at 95 K. The value for the exchange energy has been theoretically studied [59]. Ghosh *et al.* showed the effect of Mn-Mn separation on the exchange constant. The magnetic moments switch between ferromagnetic and anti-ferromagnetic coupling over a small change in Mn-Mn distance. In fact, when excess Mn atoms occupy Ni or Ga sites, the excess Mn atoms couple anti-ferromagnetically [60].

The exchange energy has also been investigated experimentally. Runov *et al.* found the exchange energy from neutron diffraction experiments [41]. The authors measured the distribution of magnons measured with neutron diffraction, from which they calculated the spin wave stiffness to be 100 meV·Å^2. Lazpita *et al.* measured the magnetic ordering in off-stoichiometric Ni_2MnGa [60]. They found that when increasing the Mn content, Mn atoms substituted on Ga or Ni sites and vacancies did not form. This

results in Mn atoms coupling anti-ferromagnetically which decreases the overall magnetization. The authors found the magnetization per formula unit for stoichiometric Ni_2MnGa was 4.17 Bohr magnetons (μ_B), which decreased for off-stoichiometric composition due to anti-ferromagnetic coupling between Mn atoms. The exchange energy calculated from Equation (2.3), $C_{ex} = \frac{WSN}{2V}$, where W is the exchange stiffness constant, S is the magnitude of the magnetic moment in Bohr magnetons, N is the number of Mn atoms per unit cell, and V is the volume of the unit cell, we find an exchange constant of C_{ex} = 6 x 10^{-12} J/m [61]. Using the experimental values above, the width and energy of a 90° domain wall at a twin boundary have been calculated to be 12 nm and 0.26 mJ/m^2, respectively [36]. The large anisotropy energy and small exchange energy result in narrow domain walls.

2.3.1 Analytical studies

The first analytical studies in MSMAs investigated the magneto-mechanics in terms of classic magnetostriction [62]. Tickle *et al.* incorporated the Zeeman, anisotropy, stray field, and mechanical strain energy to predict the magnetostrain and domain structure under an external magnetic field and uniaxial compressive stress [31]. In fact, the ordinary magnetostriction in Ni-Mn-Ga is relatively small, approximately 5 x 10^{-5} [63].

O'Handley analyzed a two-variant system where the discontinuous Zeeman and magnetocrystalline anisotropy energies across a twin boundary was the driving force for twin boundary motion and magnetostrain [29]. The model included an external stress term, and suggested that the field-induced strain increased linearly with external field in the absence of an external mechanical stress. In fact, MFIS occurs when a stress

generated by an external field overcomes a critical stress required for twin boundary motion. Müllner *et al.* compared the energy discontinuity with the work required to move a twinning dislocation in order to establish a value for the maximum possible stress (*i.e.* the magnetostress) from an external magnetic field [4]. The approaches of O'Handley [28] and Müllner *et al.* [4] yielded the same relation between external magnetic field and magnetostress.

Chernenko *et al.* [64] developed a phenomenological model based on the model of L'vov [65] which included Zeeman, anisotropy, and magnetoelastic energies. The model analyzes the critical stress required to move a twin boundary as a statistical distribution of stress values. The results of the model and corresponding experiments showed the stress generated by an external magnetic field depends on the square of the magnetization component perpendicular to the axis of easy magnetization.

Likhachev and Ullakko developed a model based on continuum thermodynamics, relating the stress with the change in magnetic energy with strain [66-68]. The authors compared their model results with experimental results for magnetization and magnetic field induced strain and found good agreement. Continuum thermodynamic models have been used to describe the magneto-mechanical response [29] in actuators and energy harvesters [39,69-72].

Paul *et al.* account for the exchange energy [36]. Paul *et al.* analyzed a single twin boundary in order to investigate the interaction of a Gaussian stress distribution at a twin boundary with the 90° domain wall [36,37]. The study showed that the magnetic domain wall motion precedes twin boundary motion.

The stray field energy was largely ignored in analytical models. If included, the magnetization was often considered to be homogeneous [23,34,35] . As experiments show, the stray field energy plays a large role in the magneto-mechanics of MSMAs. Heczko *et al.* showed that the external field required to move a twin boundary changes with the size of twin domains [23]. Heczko *et al.* went further in their analysis, considering the magnetization of neighboring twin domains as separate and dependent. Previous analysis by Heczko, which disregarded shape and size of twin domains, predicted the critical field for Type I twin boundaries, but not Type II twin boundaries, which require much lower fields to propagate. Instead of calculating the internal field energy based on the net magnetization of the entire sample, Heczko *et al.* found the internal field energy for each twin domain separately. Additionally, the authors calculated the effect of the stray field from each twin domain on the magnetization of neighboring twin domains. Heczko *et al.* predicted the increase in critical field required to move Type II twin boundaries as the size of the unfavorable twin domain decreased.

2.3.2 Experimental studies

Optical microscopy

Optical techniques utilizing Nomarski contrast or the Kerr effect with magneto-optical foil have been used to study in-situ twin domain formation and evolution. Sullivan *et al.* created contrast between magnetic domains using a Nomarski interferometer and magnetic colloids to study the in-situ domain evolution in a magnetic field [73]. Sullivan *et al*. used the same contrast method to visually verify the magnetic field induced martensite transformation [73]. The magnetic domain walls formed before the structural transition completed. The twin boundaries defined the magnetic structures; domain walls

zig-zagged through twin domains, following the axis of easy magnetization. The coercivity of the material was attributed to domain walls pinned at twin boundaries.

Magneto optical foil (MOIF) has been used to study the domain structure and evolution under mechanical stress [40] and an external magnetic field [74]. Lai *et al.* showed that, while the twin domain with AEM parallel to an external field saturates, *i.e.* only one magnetic domain exists, the other twin domain still contains multiple magnetic domains and 180° domain walls (Figure 2.4). The lack of continuity of magnetic domain walls across the twin boundary causes magnetic moments aligning "head-to-head" or "tail-to-tail", which results in a divergence of magnetization, which are associated with a large internal field energy due to a divergence of magnetization.

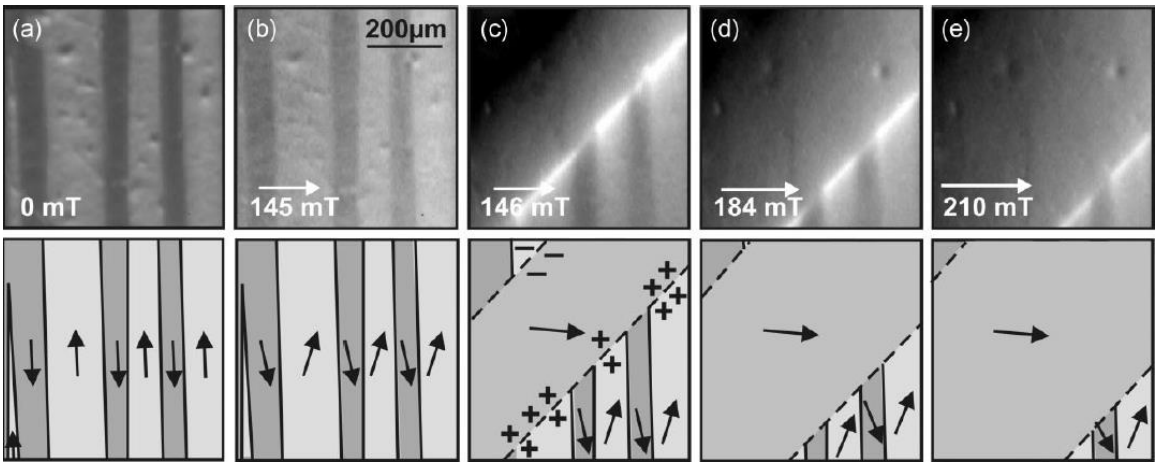

Figure 2.4 Domain walls move in twin variants with AEM parallel to the magnetic field. Domain walls do not move in the variant with the AEM perpendicular to the magnetic field. The continuity of domain walls across the twin boundary is broken, which results in large stray field and internal field energy (volume magnetic charges due to magnetization divergence in the bulk) [74]

An analogous study was done with MOIF and a mechanical stress [40]. Magnetic domain walls maintained continuity across a twin boundary. As the twin boundary moved under mechanical stress, the magnetic domain walls curved to maintain continuity across

the twin boundary (Figure 2.5). The curved domain wall resulted in a large stray field; the domains split into smaller domains to decrease the stray field energy.

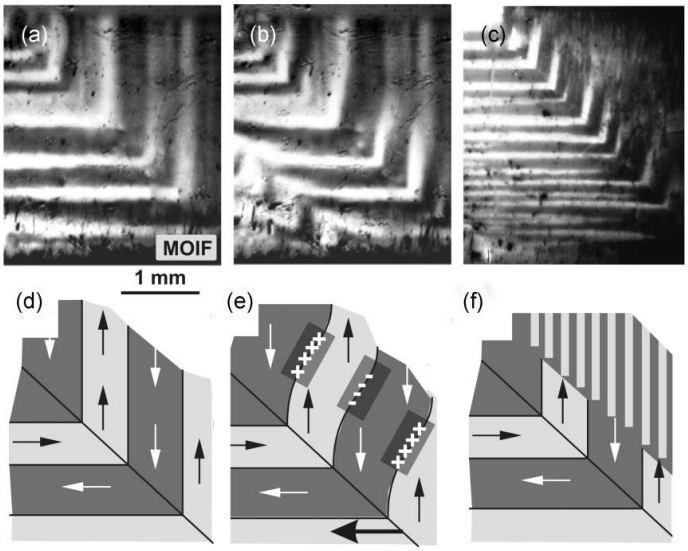

Figure 2.5 MOIF shows contrast between magnetic domains before mechanically-induced twin boundary motion (a,d) and after. Magnetic domain walls bend (b, e) to preserve continuity across the twin boundary when the twin boundary moves under mechanical stress. This also leads to magnetization divergence and a large stray field. To minimize the internal field energy, magnetic domains split into finer domains (c, f) [40,75]

Magnetic force microscopy

Magnetic force microscopy (MFM) is a scanning probe microscopy technique in which a magnetic tip moves at a constant height above the sample surface and reacts to the magnetic stray field of the sample. The technique is especially useful for characterizing thin films [61,76,77], but has also been used to characterize bulk micromagnetism [78,79].

Diestel *et al.* examined the twin and magnetic domain structure of a Ni-Mn-Ga thin film grown on an MgO substrate using MFM [61]. The authors applied micromagnetic analysis to derive the energy density of the film. They predicted the equilibrium spacing of magnetic domain walls to be proportional to the square root of the

film thickness, which correlated well with experimental findings (Figure 2.6). The equilibrium magnetic structure, with AEM both normal to and in the plane of the film, differed from a film grown on a Si substrate [77]. Golub *et al.* found a (220) texture and AEM at a 45° angle to film normal. The axis of easy magnetization found in a film grown on a Mo substrate [76] also occurred normal to and in the plane of the film.

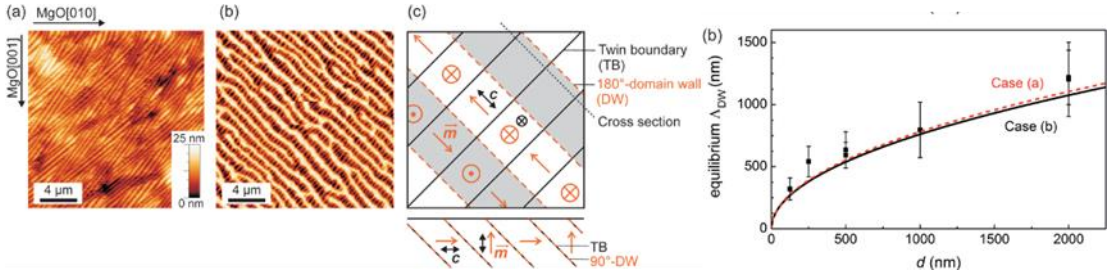

Figure 2.6 (a) Topography of the thin film from AFM and (b) magnetic domains from MFM are shown along with the proposed structure of twin and magnetic domains (c). The authors calculated for the equilibrium magnetic domain width as a function of film thickness; the results agreed with experimental data (d) [61].

Jakob *et al.* investigated the change in micromagnetic structure across the martensite transformation and Curie temperature in a thin film grown on an MgO substrate [78]. The authors noticed an abrupt decrease in the magnetic domain thickness when heating into the austenite phase. Within the austenite phase, further heating resulted in straightening of domain walls before reaching the Curie temperature. There was a hysteresis between the heating and cooling cycles in the temperature at which these transitions in domain patterns occurred.

MFM has also been used to perform in-situ experiments in bulk samples. Pan and James investigated the magnetic domain structure as the specimen was cooled across the phase transition under an applied field[79]. Under no field, the specimen formed a fine twin structure with little surface relief when cooled into the martensite phase. In an external field greater than 2kOe, a completely different twin structure formed when

cooling, which did have surface relief and a “fir” type domain structure at twin boundary interfaces.

Transmission electron microscopy

Transmission electron microscopy has been used to study magnetic domains in Ni-Mn-Ga [80] including domains pinned at an anti-phase boundary in an external magnetic field [81] and through the martensite phase transformation [82]. Budruk *et al.* examine the structure of domains looking edge-on to the AEM [81]. The domains formed a maze-like structure without an external magnetic field. Under an external field, the domain walls lined up parallel to the field (Figure 7). Domain walls aligning parallel to the field decreased the Zeeman energy since the moments in the domain wall had a component parallel to the field.

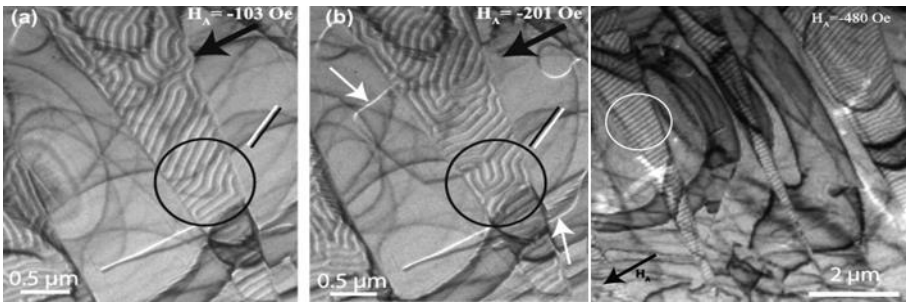

Figure 2.7 Transmission electron microscopy images of 180° domain walls viewed parallel to the AEM under external magnetic fields of -103 Oe (a), -201 Oe (b), and -480 Oe (c) [81]

Budruk *et al.* also investigated domain wall pinning at twin boundaries and an anti-phase boundary (APB). At an external field of 300 Oe, 90° domain walls remained pinned at twin boundaries; above this field the domain wall started to disappear. This correlates with the findings of Paul *et al.*, who predicted the domain wall motion would precede twin boundary motion. Budruk *et al.* showed a domain wall pinned at an APB was somewhat mobile at a field of 250 Oe.

2.3.3 Numerical Modeling

Numerical micromagnetic modeling in Ni-Mn-Ga can, in general, be broken down into two groups: finite element modeling and phase-field modeling, which uses a finite-difference method for calculations. The finite element method solves for boundary conditions of magnetism laid out by Maxwell's equations, and then solves for the continuum equations over a matrix of points, which are meshed together. Phase field modeling substitutes a boundary condition at an interface with a partial differential equation, creating a smooth change between discrete property values in each neighboring phase. The result is a phase field equation, which is used as an order parameter.

Typically, numerical simulations were run over a sample size much smaller than those used in experiments in order to keep simulation time of dynamic changes to a reasonable duration. The difficulty of accurately describing experimental results with such a small simulated area has been noted [83], as well as the difficulty in coupling the dynamic changes of magnetic and mechanical microstructure [84]. Nevertheless, numerical simulations calculated energies using robust mathematical descriptions of magnetic energies, which are too complex for analytical methods. Numerical simulations provide insight into magnetic structure and resulting energies, which determine magneto-mechanical properties.

Numerical methods have been applied to investigate the coupling of magnetic and structural transition across the Austenite-martensite phase transition as well as the magnetic transition across the Curie temperature [85]. Jakob *et al.* simulated the changes in magnetic domain structure across the phase transition, which exhibited a sharp decrease in magnetic domain width in the austenite phase. Conti *et al.* simulated shape-

memory polymer composites to investigate the influence of particle orientation and mechanical properties of the polymer on composite behavior [86]. The authors assumed the particles contained a single twin domain, and included the external field, internal field, anisotropy, and exchange energies. This is in stark contrast with numerical methods, none of which accounted for all four of these energy terms in calculations. Conti *et al.* concluded the particle shape and orientation, along with elasticity of the polymer play the most important roles in bulk properties. Conti *et al.* further developed the model to include inhomogeneous particles, *i.e.* polycrystals [87].

Although numerical methods greatly improved the ability to account for different energies, Conti *et al.* and Daniel *et al.* [85] simplified the model by assuming a homogeneous magnetization inside a twin domain, *i.e.* they disregarded 180° magnetic domains. A difficult task is incorporating the inhomogeneity of magnetization in a twin domain and across twin boundaries. Landis *et al.* showed that, if a model rigidly couples martensite strain to the magnetization, unrealistically small and high energy domain walls formed [88]. Luskin *et al.* created a model with finite-element methods which applied a strain gradient model to the material as well as a piecewise function to the discontinuity at the twin boundary [89]. It has been shown that, for certain limiting conditions, the free strain is effectively described using a strain gradient model [88]. Luskin *et al.* found that, for the approach including the discontinuity at the twin boundary, the error in energy minimization decreased as the mesh size decreased. Smaller mesh size means longer computation time.

Phase field simulations use equations to solve for order parameters which describe a property in each phase. Continuous equations smooth transition in the values

of order parameters between phases (in this case, martensite variants). Phase field models for magnetic shape memory alloys use two order parameters to describe the magnetization, those being the two angles necessary to describe the orientation of the magnetic vector in polar coordinates. Order parameters are also defined to describe the strain and twin domain evolution. Jin has used phase field simulations which include the exchange, anisotropy, internal field, external field, chemical, gradient, internal elastic and external elastic energies [90-93]. Jin changed model parameters in order to investigate the influence of twin boundary mobility [91] elastic interactions [93] and magnetostatic interactions [92] on the evolution of magnetic and twin domains structure. When the magnitude of the external field increased, the energetically unfavorable twin domain became more heterogeneously magnetized, resulting in larger internal fields. The twin boundary mobility influenced the evolution of magnetic domains in twin domains [92]. At high mobility, magnetic domain walls receded from the twin boundary as the energetically favored magnetic domain grew. Simulations took less time and strain increased, as well [91]. Small elastic strain energy at the twin boundary resulted in twin boundaries in the model bending away from {101) planes of martensite, which is not seen in experiments [93]. Zhang *et al.* applied phase field methods to investigate the stability of martensite and magnetic domain structure of a sample in an external field and under mechanical stress [94]. The model accounted for multiple twin domains and magnetic domains within twin boundaries. The energy minimization done by Zhang *et al.* resulted in uniformly magnetized twin domains with a fine twin structure.

Khan *et al.* created a model which contained regions of material with different magnetic properties in order to model the change in axis of easy magnetization across a

twin boundary [95]. The authors applied the boundary condition from Poisson's and Maxwell's equations in a finite element scheme in order to show the effect of twin boundaries on the flux density through the material. Magnetic flux decreased as it passed through twin boundaries, which was due to the internal field created at the twin boundary interface.

The results of Khan *et al.* depicted the influence of the twin domains on the internal field, much like the experimental results of Lai *et al.* [40] and Heczko *et al.* [75]. Heczko *et al.* [23] specifically showed the influence of the internal field on the critical field for twin boundary motion. As the strain decreased, the geometry of the twin domains changed such that the demagnetizing factor increased. The demagnetization factor increased the internal magnetic field, which increased the critical external magnetic field required to move the twin boundary by approximately 50% [23]. Haldar *et al.* iteratively calculated magnetization to correct for demagnetization [96]. The authors showed critical field increases due to demagnetization effects, and the critical magnetic field increased as the sample dimension parallel to the external field decreased. The authors also investigated the Maxwell stress in the specimen. The internal field resulted in varying magnetization across the sample, which gave rise to inhomogeneous Maxwell stress. Peng showed a similar effect with phase-field simulations [97]. As the width of a specimen decreased by two orders of magnitude the critical field increased by a factor of two and the field required to saturate the material increased by a factor of four[98].

2.4 Heusler alloys

In 1903, Friedrich Heusler discovered ferromagnetism in Cu_2MnAl, despite none of the constituent elements are themselves ferromagnetic. Today, Heusler alloys are

defined as ferromagnetic materials which exhibit the $L2_1$-ordered face centered cubic phase. The $L2_1$ structure (space group $Fm\bar{3}m$) has a composition X_2YZ where X and Y are typically transition metals. The *Y* component may be a rare-earth metal and the *Z* component is generally a non-metal or non-magnetic.

In the Austenite phase below the Curie temperature, the ferromagnetic shape memory alloy with stoichiometric composition Ni_2MnGa exhibits ferromagnetic behavior in the $L2_1$ structure. Although Ni is ferromagnetic, Mn contributes the strongest magnetic moment to Ni_2MnGa [60]. The atomic positions of Ni, Mn, and Ga are given in Table 2.1. Figure 2.8 shows the crystal structure for the Heusler phase of Ni_2MnGa.

Table 2.1 Crystallographic positions for Ni, Mn and Ga elements in the austenitic Heusler structure shown in Figure 8.

Ni	Mn	Ga
[¼ ¼ ¼]	[½ 0 0]	[0 0 0]
[¾ ¼ ¼]	[0 ½ 0]	[½ ½ 0]
[¼ ¾ ¼]	[0 0 ½]	[½ 0 ½]
[¼ ¼ ¾]	[½ ½ ½]	[0 ½ ½]
[¾ ¾ ¼]		
[¾ ¼ ¾]		
[¼ ¾ ¾]		
[¾ ¾ ¾]		

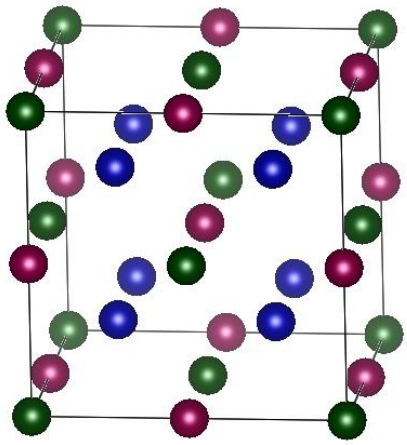

Figure 2.8 Heusler phase of Ni-Mn-Ga. Ga atoms occupy corner and face centers (green), Mn atoms occupy edge sites (red), and Ni atoms (blue occupy each quadrant of the unit cell.

2.4.1 Martensitic Structure

The Martensitic transformation temperatures of Ni-Mn-Ga depend strongly on the composition of the alloy. Changing the atomic compositions of the elements by 5%, the austenite/martensite equilibrium temperature varies from 154 to 458 K [99]. Often, a composition is expressed in terms of the ratio of valence electrons per atom (*e*/*a*). For Ni_2MnGa, a unit cell contains 8 Ni atoms with 10 valence electrons each, 4 Mn atoms with 7 valence electrons each, and 4 Ga atoms with 3 valence electrons each. Thus, for stoichiometric Ni_2MnGa, the *e*/*a* ratio is 7.5. The ratio increases with increasing Ni content, or by substituting Mn for Ga. The martensite transformation and Curie temperatures are given as a function of *e*/*a* ratio in Figure 2.9 [100].

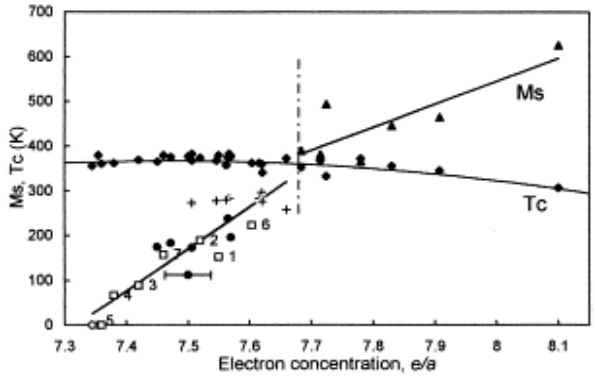

Figure 2.9 Martensitic transformation temperature (Ms) and Curie temperature (TC) for the different Ni-Mn-Ga alloys as a function of electron concentration (*e/a*). Diamonds represent the Curie temperatures of all alloys. Circles refer to alloys with 25 atomic % Mn, triangles to alloys with 21 atomic % Ga, and pluses to alloys with 50 atomic % Ni. Uncertainty for each symbol is shown by horizontal limiting bar. [100]

The most commonly reported martensite structures are the seven-layered monoclinic structure (14M), the five-layered monoclinic structure (10M) and the non-modulated tetragonal structure (NM). The specimen used in all experiments had the 10M structure. Figure 2.10 shows room-temperature phases for alloys with different compositions taken from Jin *et al.* [101], along with solid lines indicating isotherms for the martensite start temperature, M_s [102].

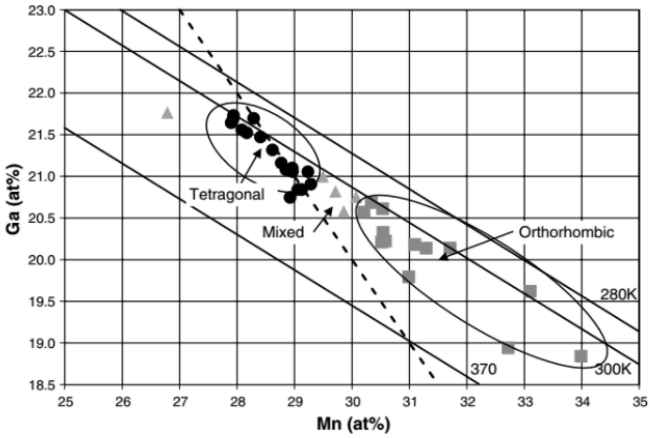

Figure 2.10 Martensite structure shown as a function of composition. Circles have 10M strucutre, triangles are mixed 10M/14M, and squares are 14M. Solid lines indicate martensite transformation temperatures and the dashed line indicates compositions with 50 atomic % Ni. Compositions were taken from Jin et al. [101]

Ni-Mn-Ga magnetic shape memory alloys transform from cubic Austenite to martensite, at a temperature which is tuneable with composition [99]. The transformation may occur directly from austenite to NM martensite, from Austenite to 10M martensite, or sequentially from Austenite to 10M to 14M to NM [103]. The transformation also occurs when applying an external mechanical stress. Similar transformation sequences occur for the stress-induced phase transformation [104].

The monoclinic 10M crystal structure has a monoclinic angle of between 90.2 and 90.5° and the lattice parameters *a* and *b* are almost equal. Because of the small deviation of the monoclinic angle from 90° and because of the small difference between *a* and *b*, the 10M crystal structure often is approximated as face-centered tetragonal; however, the actual crystal structure as defined by the International Union of Crystallography is monoclinic with space group I2/m. The monoclinicity as a function of martensite transformation temperature is given in Figure 2.11 [105].

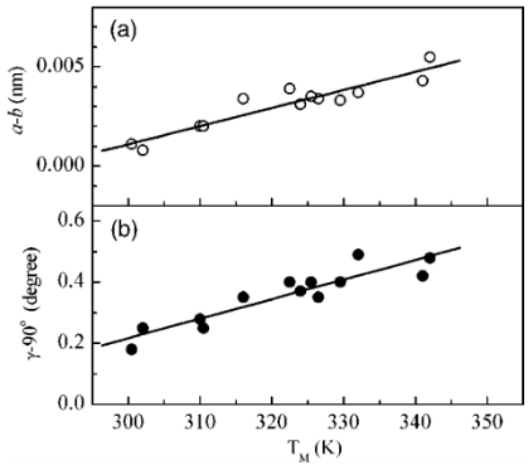

Figure 2.11 Monoclinic distortion for alloys with 10M phase at 298 K as a function of martensitic transformation temperature. (a) Difference of parameters *a* and *b* and (b) deviation of the angle *γ* from 90° [105].

2.4.2 Twinning and Deformation

The transformation from the higher symmetry austenite phase to the lower symmetry martensite phase is a diffusionless transformation that occurs by shear distortion of the lattice [106]. The phenomenological theory of martensite transformations [107,108] describes a total shape change which is imposed on a volume element of austenite as an invariant plane strain $\mathbf{P_1}$:

$$\mathbf{P_1 = RP_2B}$$

where the Bain distortion **B** is a homogeneous distortion which transforms the austenite lattice to the martensite lattice. Generally, **B** does not have an invariant plane. $\mathbf{P_2}$, a lattice invariant shear, plastically deforms the lattice such that $\mathbf{P_2B}$ produces an undistorted plane from the parent austenite. This undistorted plane must be rotated by **R** to become completely invariant after the total transformation $\mathbf{RP_2B}$.

The lattice invariant shear, $\mathbf{P_2}$, may occur via slip or twinning [28]. Twinning is the operative mechanism in shape memory alloys. The martensite transformation results in a twinned microstructure. Twinning is described by elements K_1, K_2, η_1, and η_2, which are shown in Figure 11. K_1 is the invariant plane, called the twinning plane. The shear direction or twinning direction is η_1. The conjugate twinning plane K_2 intersects K_1 on a line perpendicular to the shear direction. K_2 is also undistorted and makes an equal angle with K_1 before and after the shear. The shear plane s contains η_1 and the normal direction to K_1. The direction η_2 is the conjugate twinning direction and is defined by the intersection of K_2 and *s* [109,110].

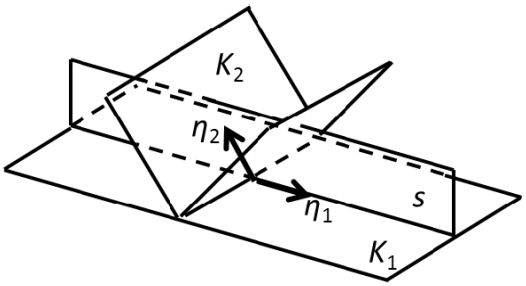

Figure 2.12 Twinning elements: K_1 is the invariant twinning plane with η_1 the twinning direction parallel to K_1., K_2 is the conjugate twinning plane with η_2 the conjugate twinning direction parallel to K_2. The shear plane *s* contains the twinning directions and intersects the twinning planes. [110]

The crystal lattice is not changed by the shear, giving the condition that either K_1 or η_2 both have rational, small indices (Type I twin) or K_2 and η_1 both have rational, small indices (Type II twin) [110]. If all four elements are rational, the twin is compound. Type I twins are related by mirror symmetry with respect to K_1. Type II twins are related by a rotation of π about η_1.

In the magnetic shape-memory alloy Ni-Mn-Ga, the NM phase has a tetragonal unit cell. All twinning elements are rational, and the NM phase has compound twins. The 10M phase has a monoclinic lattice, which results in several different twinning systems whereof two operate to produce MFIS [111]. The twinning elements for compound twins in the tetragonal lattice and for the Type I and II twins in the monoclinic lattice are given in Table 2.2 [111].

Table 2.2 Twinning elements for compound twins in the tetragonal lattice and Type II twins in the monoclinic lattice of 10M Ni-Mn-Ga. For Type I twins, K_2 and η_1 are irrational, while for Type II twins, K_1 and η_2 are irrational [111]

Twinning element	Tetragonal	Monoclinic Type I	Monoclinic Type II
K_1	$(01\bar{1})$	$(01\bar{1})$	$(\overline{0.1058}\ 1\ \bar{1})$
η_1	$[011]$	Irrational	$[011]$
K_2	(011)	Irrational	(011)
η_2	$[01\bar{1}]$	$[01\bar{1}]$	$[0.0924\ 1\ \bar{1}]$
s	(100)	(100)	$(\bar{1}\ \overline{0.0462}\ \overline{0.0462})$

Straka *et al.* reported an order of magnitude difference of twinning stress in a specimen with different twin boundary density [22]. The authors attributed the difference in twinning stress to the twin boundary structure. Kellis *et al.* measured the switching field (which is related to the twinning stress [64]) in single crystals polished along (100) faces, and showed two discrete ranges for the twinning stress [112]. The twin boundaries with lower twinning stress occurred at an 82-84° angle with the edge of the crystal, while the twin boundaries with larger stress occurred at nearly 90° angle with the edge. Sozinov *et al.* described the Type I and Type II twinning systems in a monoclinic lattice structure, and determined the twinning planes for Type I and Type II twin boundaries in the 10M phase of Ni-Mn-Ga [111]. The authors calculated the angle between the twin boundary and surface normal to be 4.12°. The twin boundary trace across a (100) surface of a specimen is 90°±4.12°. Straka *et al.* went further to describe the orientation of the Type II twin boundary across (100) type compound twins, and showed the angle of the twin boundary with the surface changes by approximately 12° across (100) twin boundaries

[113]. This results in the Type II twin boundaries zig-zagging across the surface of the sample.

Type I twin boundaries, in general, require a larger critical stress to propagate than Type II twins [8,9,111-116]. Straka *et al.* measured the twinning stress for Type I and Type II twins in 10M Ni-Mn-Ga as a function of temperature [114]. The authors showed that, near the martnesite transformation temperature, Type I and Type II twin boundaries required the same stress to move, which was about 0.1 MPa. As the temperature decreased, the twinning stress for Type I twin boundaries increased linearly by approximately 0.04 MPa per degree K, while the twinning stress of Type II twin boundaries remained constant. This effect was seen in many different crystal compositions. Heczko *et al.* measured a constant twinning stress of Type II twin boundaries down to 1.7 K [116].

Type II twin boundaries also have higher mobility. Faran and Shilo optically measured the velocity of twin boundaries in response to different magnetic field magnitudes [8,9]. The authors found that, above the critical field required to move the twin boundary, the Type II twin boundary velocity increased more quickly with increasing driving force (magnetic field magnitude) compared with the Type I twin boundary.

CHAPTER THREE: SENSING STRAIN WITH NI-MN-GA

This chapter is published in modified form by Elsevier in *Sensors and Actuators A: Physical* and should be referenced appropriately.

Reference:

A. Hobza, C. Patrick, K. Ullakko, N. Rafla, P. Lindquist, P. Müllner. Strain Sensing with Ni-Mn-Ga, Sensors and Actuators A: Physical (2018) 269:137-144. DOI: 10.1016/j.sna.2017.11.002

STRAIN SENSING WITH NI-MN-GA

Anthony Hobza[1]

Link Patrick[2,*]

Kari Ullakko[3]

Nader Rafla[2]

Paul Lindquist[1]

Peter Müllner[1]

Published in:

Sensors and Actuators A: Physical

January 2018

[1]Materials Science and Engineering, Boise State University, Boise, ID, USA

[2]Electrical and Computer Engineering, Boise State University, Boise, ID, USA

[3]School of Engineering Science, Lappeenranta University of Technology, Savonlinna, Finland

*Now at Electrical Engineering, Princeton University, Princeton, NJ, USA

3.1 Abstract

Deformation changes extensive magnetic properties in magnetic shape memory alloys, such as a resistive or piezoelectric strain gauge, without the constraint of operating the elastic region. This study investigates a strain measurement technique with potential to expand to strain measurement in three dimensions with one piece of material. A Ni-Mn-Ga single crystal placed inside a doubly wound coil with a primary and a secondary winding was used as a strain sensor. An AC voltage excited the primary coil and the secondary voltage varied as the sample was strained from 0 to 5.2%. This method varies from other methods that utilize complex magnetic circuits, require high magnetic fields, or other sensing methods such as Hall probes. When the sensor element was tested statically by compressing the element manually against a bias magnetic field perpendicular to the load axis, the voltage output varied from 129.7 mV to 164.2 mV. The dynamic performance of the sensor was tested by cycling the element between 25 and 100 Hz in compression against a bias magnetic field in a displacement controlled magneto-mechanical test system. The bias magnetic field was varied from 0.2 to 0.8 T (0.16 to 0.64 MA/m) while the cyclic displacement was varied from 0.5 to 4.5% strain. The voltage amplitude of the signal in the secondary coil increased with decreasing tensile strain. The full scale RMS voltage at a 200 μm stroke increased from 53.0 mV to 78.4 mV as the bias magnetic field decreased from 0.8T to 0.2 T. As the element was compressed, there was no difference in the voltage output of the sensor between the static

and dynamic tests. When the element expanded during unloading, the voltage output of the sensor from the static test matched the voltage output during compression. For the dynamic testing, the voltage output of the sensor exhibited a hysteresis from the loading voltage output, the hysteresis increased when the strain rate increased.

3.2 Introduction

The magnetization of magnetic shape-memory (MSM) alloy Ni-Mn-Ga changes linearly with strain which is useful for a strain sensor [1]. Current resistance and piezo-electric strain gauges are limited to operating in the elastic strain range of the element – which is small – and the straining specimen works against the elastic modulus of the gauge. Inductive strain gauges such as linear variable differential transformers are bulky. MSM alloys reversibly deform under a very low stress [2], which provides opportunities for sensor applications [3]. Developments in MSM crystal growth using high purity elements produce oriented single crystals with high chemical homogeneity and twinning stress as low as 0.05 MPa [2,4], with reversible strains up to 7% [5] for 10M structure and 11% [6,7] for 14M structure.

When cooled from high temperature, MSM alloys transform from cubic austenite to martensite. Ni-Mn-Ga martensite with 10M monoclinic structure is often approximated as tetragonal, with $c < a$. The martensitic transformation results in three martensite variants with different orientations of the crystallographic *c* direction, which is the direction of easy magnetization. Heczko recently reviewed the magneto-mechanics of MSM alloys of Ni-Mn-Ga [8]. In brief, under a mechanical stress or magnetic field, the variant with *c* most closely parallel to a compressive stress component or to the magnetic field direction grows at the expense of other variants. Variant growth or shrinkage

proceeds through the motion of twin boundaries. Twin boundary movement reorients the short crystallographic *c* direction of unfavorably oriented variants such that it aligns to the applied compressive stress or magnetic field. Twin boundaries move if the stress exceeds the twinning stress or the magnetic field exceeds the switching field. Low twinning stress and magneto crystalline coupling make Ni-Mn-Ga useful for actuating, sensing, and energy harvesting.

When the direction of easy magnetization reorients there is an electromagnetic response. In energy harvesting or strain sensing the electromagnetic response is used when the crystal strains [1,9-14]. Müllner *et al.* measured the flux density parallel to an applied magnetic field and perpendicular to the direction of mechanical compressive strain with a Hall probe. They found a nearly linear relationship between the strain and flux density due to the change in magnetization of Ni-Mn-Ga. The authors proposed the use of the reverse magneto-plasticity effect for sensing applications [1].

Suorsa *et al*. found that the flux density as measured with a coil around the element has a linear relationship to strain at high applied fields (>40 kA/m), while at low fields (<40 kA/m) the relationship was non-linear [12]. The authors concluded that in low-field applications, such as sensing, a linear relationship is not valid. Sarawate *et al*. showed the magnitude of variation in flux density with strain changes with the magnitude of the external field [11]. Sarawate measured flux density changes due to dynamic strain up to 160 Hz at a bias field of 368 kA/m [13]; the flux density-strain relationship showed large hysteresis, which increased as the frequency increased. The authors attributed the hysteresis to a loss from the rotation of the magnetic moment.

The flux density and the magnetic permeability through the material change with the sample strain [15,16]. Suorsa *et al.* placed an MSM element between an iron yoke wrapped with two coils. The authors measured changes in inductance by applying a 180 Hz AC voltage to the coils without a bias magnetic field. The test setup mechanically strained the element in the direction perpendicular to the axis of the coils and measured the change in mutual inductance of the coils. Tensile strain induced motion of twin boundaries and reoriented the *c* axes of unfavorably oriented variants parallel with the coils. A larger fraction of the element with easy magnetization parallel to the axis of the coils increased the inductance of the system. The measured inductance was larger than the calculated linear relationship but less than the calculated non-linear relationship.

In our study, the sensor consisted of an MSM single crystal and two coils that were wound simultaneously. One coil was excited with an AC voltage, and the induced voltage in the second coil was measured. We compare the magnitude of the induced voltage to the strain of the sample for static tests and at a range of dynamic frequencies and motor strokes. The secondary coil output voltage decreases with increasing tensile strain of the MSM core over a range of cyclic loading frequencies and amplitudes.

3.3 Experimental Setup

A single crystal with a nominal composition of $Ni_{51}Mn_{27}Ga_{22}$ (numbers indicate atomic percent) was grown with the Bridgman-Stockbarger technique using the crystal growth system developed by Kellis *et al.* [4]. After crystal growth, the composition along the crystal growth direction was measured every 2 mm by electron dispersive spectroscopy (EDS) using a Hitachi 3400S scanning electron microscope and an Oxford Instruments Energy^{+} EDS detector at a working distance of 10 mm and a 20 kV

accelerating voltage. The crystal structure and lattice constants were determined by X-ray diffraction using a Bruker D8 Discover X-ray diffractometer with a copper target operated at 40 kV and 40 mA. The X-ray beam was filtered to remove Cu K_β wavelengths, collimated and passed through a circular aperture 1 mm in diameter. The intensity of the diffracted X-ray beam was measured with a HI-STAR area detector. A portion of the crystal with a 10M martensite structure and a composition of $Ni_{51.1}Mn_{25.6}Ga_{23.4}$ was aligned and cut with a Princeton Scientific WS22 wire saw such that sample faces were parallel to {100}. These faces were then polished with 2000 grit SiC, followed by a sequence of diamond pastes to 1 μm, and finally 0.03 μm alumina slurry yielding a crystal of size 2.14 x 3.35 x 7.53 mm^3 (elongated, *c* parallel to the 3.35mm edge). Prior to testing, the twinning stress was measured at 0.72 MPa (in compression) on a Zwick screw-driven test bench type 1445 and the magnetic switching field was measured at 0.3 T (0.24 MA/m) using a MicroSense Model 10 vibrating sample magnetometer.

The dynamic performance of the sensor system (Ni-Mn-Ga crystal + doubly wound drive/pick-up coil) was measured by cycling the crystal in compression against a bias magnetic field perpendicular to the load axis. An instrumented Magneto-Mechanical Test Apparatus (MMTA), pictured in Figure 3.1, measured force and elongation of the Ni-Mn-Ga single crystal while it was cyclically deformed in a magnetic field. This system was described in detail by Lindquist and Müllner [17]. Its main components are: (a) A variable-field electromagnet with maximum field strength of 1.2 T (0.96 MA/m); (b) A voice coil motor with maximum actuation frequency of 800 Hz; (c) A linear-variable differential transformer (LVDT) displacement transducer; (d) A sample

compression micrometer; (e) A 44 N piezoelectric dynamic load cell; (f) springs to tune the resonant frequency of the voice coil motor; (g) The Ni-Mn-Ga single crystal test sample. Analog signals for force and displacement were connected as inputs to a multiplexed four-channel 16 bit analog to digital converter (ADC). The current to the electromagnet was controlled with analog output from a 16 bit digital to analog converter (DAC) that was connected to the power supply remote control. The ADC inputs and DAC outputs were controlled by a dSpace Model ACE 1104 Power PC embedded controller that was plugged into a personal computer. The embedded controller was programmed from scripts written in MatLab along with a symbolic model for the ADC and DAC converters written in Simulink, an accessory software package from MathWorks. The dSpace system was designed to work with MatLab, which had a cross-compiler/linker that downloaded the program to the dSpace controller card. The program controlled the test frequency and displacement. The test frequency and magnetic field was set by a MatLab script and the displacement amplitude was changed in dSpace while the voice coil motor ran.

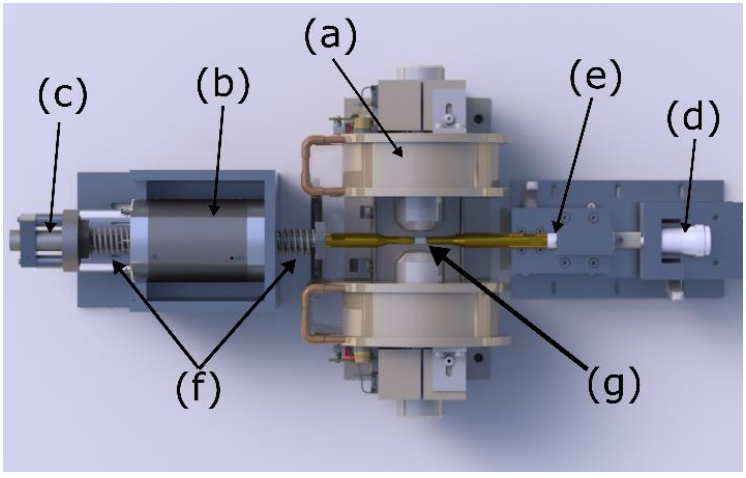

Figure 3.1 Magneto-Mechanical Test Apparatus (MMTA) with a variable-field electromagnet (a), voice coil motor (b), linear-variable differential transformer (c),

micrometer (d), piezoelectric force transducer (e), springs to tune the resonant frequency of the motor (f), and Ni-Mn-Ga specimen (g).

A double coil of 1000 turns per coil was wound with two 43 AWG magnet wires. The double coil measured approximately 5 mm in inner diameter and 6 mm in length. Each coil had a resistance of approximately 180 Ω. One coil served as drive coil, the other as pick-up coil. A Hewlett-Packard 33120A waveform generator powered the drive coil with a sine wave at 4 kHz and 800 mV peak-to-peak amplitude. The amplitude was chosen such that the maximum electrical current would not melt the insulation on the wire. The coils were placed around the sample such that the axis of the coil was parallel to the direction of loading by the motor and perpendicular to the bias magnetic field (Figure 3.1).

The pickup coil voltage was amplified by a factor of 5 with a tunable band-pass amplifier made by Alligator Technologies so that it matched the input range (+/- 1.25 V) of the analog to digital converter. The amplified pick-up coil voltage was connected to one channel of a 4-input analog to digital converter (Agilent U2542A) with 16 bit resolution. The other inputs of the U2542A measured the signals from the LVDT, the force transducer, and the drive coil voltage. The U2542A captures 4 channels simultaneously at 500 kilo-samples per second or one sample every 2 μs. This yielded 125 samples for each period of the 4 kHz sine wave.

Prior to testing, the sample was compressed to 0% strain. The sample was glued to the load platen opposite the motor with cyanoacrylate adhesive such that the 3.35 mm dimension of the sample was parallel to the magnetic field. The dual-coil was placed around the sample parallel to the load axis. The perpendicular magnetic field was turned on to 0.8 T (0.64 MA/m) to fully elongate the sample, and then changed to the desired

field for the test. With the magnetic field on, the sample was compressed against the springs manually with a micrometer screw (details are given in [17]) while monitoring the LVDT signal. The compression was determined by subtracting the LVDT displacement (amount springs have compressed) from the displacement of the micrometer.

Two types of tests were performed: static and cyclic. In static experiments, the sample was compressed manually in the axis of the coil with a micrometer and data was taken for every 30 μm of micrometer displacement at a 0.4 T bias magnetic field. In cyclic experiments, the sample was compressed manually by approximately 200 μm (to 3.33% tensile strain) before actuating the motor. Once compressed, the motor was powered on to cyclically load the sample at the test frequency and amplitude. The sample was compressed in the axis of the coil by the voice-coil motor during the load portion of the cycle and it expanded due to the bias magnetic field during the unload portion of the cycle. Compressive loading by the motor occurred against the perpendicular bias magnetic field; upon mechanical unloading, the magnetic field elongated the sample. Simulink controlled the voice coil motor frequency and it used the LVDT signal as feedback to maintain the test amplitude (sometimes called displacement-controlled testing).

The loading frequency of the voice-coil motor was set to 25, 50, 75, and 100 Hz against an perpendicular magnetic field was varied from 0.2 to 0.8 T (0.16 to 0.64 MA/m) and at peak-to-peak stroke varying from 50 μm (0.67 % strain) to 350 μm (4.67 % strain). The maximum strain was limited to 4.67% due to the clamping constraints exerted by the cyanoacrylate adhesive [18].

The experimental data was post-processed with a MatLab program that converted the raw data into stress, strain, and voltages from the double coil. The force measured by the force transducer was normalized by the cross sectional area of the sample to compute the stress. The strain was calculated from the LVDT data, initial sample compression, and sample length. The strain and voltage data were post-processed further using software filters.

In the program the LVDT data was first passed through a software filter: a 7^{th}-order low-pass Butterworth filter with a cutoff frequency of 12 kHz to suppress noise from the LVDT excitation frequency. The MatLab script applied a 3^{rd}-order Butterworth band-pass filter with a bandwidth of 1 kHz centered at 4 kHz to the drive and pickup voltage signals. This filter extracted only the modulation of the 4 kHz carrier frequency by suppressing all other signal components in the voltage from the system. The running root-mean-square (RMS) amplitude was computed for the input and output voltage waveforms by finding the RMS for each period of the 4 kHz voltage. This yielded a voltage corresponding to the amplitude modulation of the excitation voltage with 4000 points per second.

The ratio of the output voltage to the input voltage was calculated in order to find the change in output RMS amplitude independent of changes in the input RMS amplitude. The script also computed the hysteresis in this relationship to quantify the relationship between the voltage and strain.

The change in pickup voltage amplitude across the secondary coil was characterized as a function of input voltage frequency at a magnetic field of 0.8 T (Figure 3.2). The output of the secondary coil was recorded for the fully compressed and fully

elongated sample for each voltage frequency. The elongated RMS voltage was subtracted from the compressed RMS voltage to find the voltage change for full strain of the sample. The pick-up voltage difference had a maximum at 4 kHz which was then used as drive frequency for all experiments. The pick-up coil voltage was also characterized as a function of the perpendicular applied magnetic field in order to select an optimal field of 0.4 T for further testing. With these parameters, the sample was tested both statically over the full strain range of the mounted sample as well as dynamically at set values of frequency and strain. The results from these tests are presented in Section 3.3 and discussed in Section 3.4.

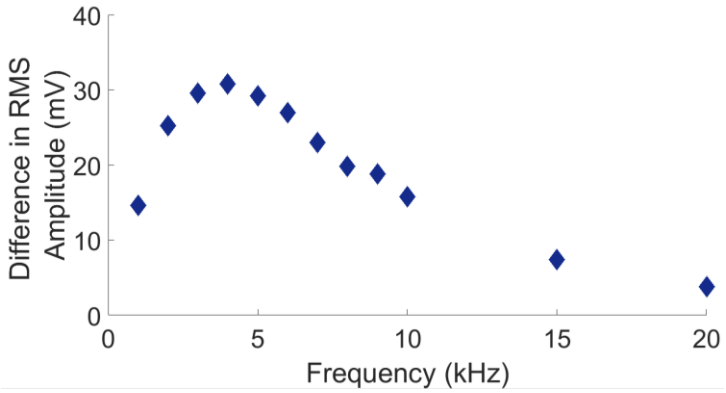

Figure 3.2 Difference in RMS output voltage as a function of drive frequency for a fully compressed and fully elongated sample in an external field of 0.4 T. The RMS output voltage has a maximum at 4 kHz, which was chosen as drive frequency for all experiments.

3.4 Results

The sample was loaded mechanically with a compressive stress from the linear motor. It compressed due to the motor and expanded due to the bias magnetic field upon mechanical unloading. A running RMS was taken for each period of the 4 kHz excitation voltage, resulting in an RMS voltage signal with 4 kilo-samples per second. Figure 3.3 contains 0.1 seconds of collected data, which corresponds to four hundred cycles of the 4

kHz excitation voltage. Figure 3.3a shows the RMS amplitude of raw output voltage data from the pickup coil collected using the U2542A before applying filters. The amplitude modulation is the response of the system (sample and noise) to the actuation of the sample. To extract the amplitude modulation from the coils and exclude any noise components, a time-averaging 3rd-order Butterworth band-pass filter with a bandwidth of 1 kHz centered at 4 kHz was applied in software to the drive and pickup voltage signals. The RMS amplitude of the filtered voltage signal only contains frequency harmonics of the primary actuation frequency (Figure 3.3b).

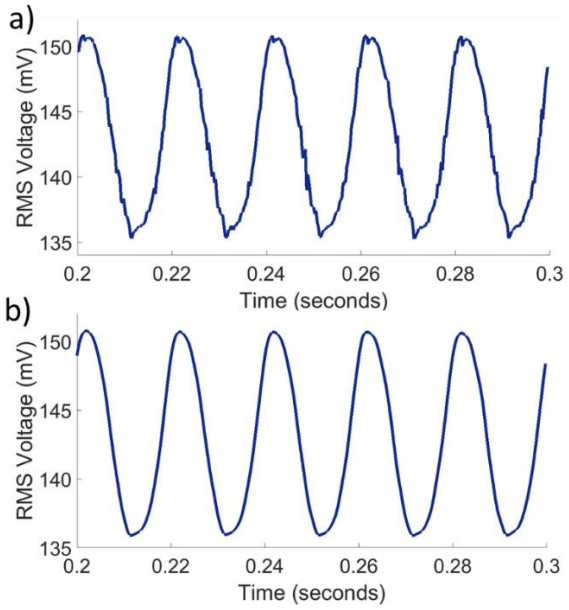

Figure 3.3 The root-mean-square of the raw voltage data from the pickup coil is shown (a) at a frequency of 50 Hz and stroke of 150 µm with an applied field of 0.4T. Time is calculated by applying a sampling rate factor to the sample number. A band-pass filter was applied to let through only the 4 kHz excitation voltage and suppress all noise components. The resulting voltage waveform shows an amplitude modulation with only the harmonics present in the sample strain (b).

The amount of strain on the sample modulated the amplitude of the 4 kHz sine wave in the pickup coil as well as in the drive coil (Figure 3.4a). The excitation voltage across the drive coil provided a changing flux within the pickup coil, which resulted in an

induced voltage across the pickup coil at the same frequency. The changing magnetization of the sample due to the reorienting of the easy axes of magnetization also resulted in a changing flux in the coil. This changing flux also modulated the input voltage independent of the modulation from the mutual inductance.

The amplitude of the pickup coil was a function of the drive coil amplitude. Figure 4b shows the ratio of the pickup coil amplitude to the drive coil amplitude. The strain on the sample (Figure 3.4c) was calculated from the LVDT, initial compression, and sample length. The modulation of the amplitude (RMS ratio, Figure 3.4b) was in phase with the strain of the sample; the sample strain caused the changing output voltage relative to the input voltage (Figure 3.4d).

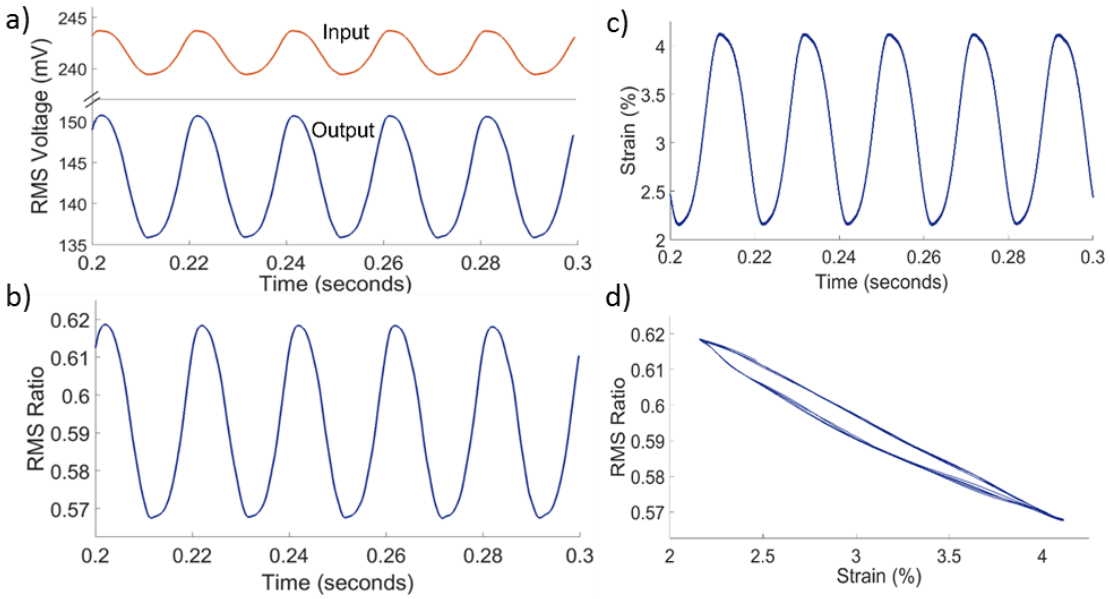

Figure 3.4 The MatLab script applied a band-pass filter to both the input and output voltage data, and then calculated a running RMS for each voltage waveform (a). A ratio of the output RMS to input RMS is taken to account for the modulation of the input voltage waveform (b). The motor displacement was measured using the LVDT and the MatLab program applied a low-pass filter with a 12 kHz cutoff frequency to suppress noise from the excitation voltage of the LVDT. Strain was calculated using the filtered LVDT signal, initial position of the LVDT and initial strain of the sample (c). The RMS Ratio was plotted against the strain to analyze the voltage-strain relationship of the measurement coils (d).

Figure 3.5 shows the stress *vs*. strain curves at 50 Hz while varying the stroke of the motor at 0.4 T external magnetic field. The initial compressive displacement on the sample before turning the motor on was approximately 200 µm (3.33% tensile strain). The center point of oscillation stayed consistent while the magnetic field was held constant.

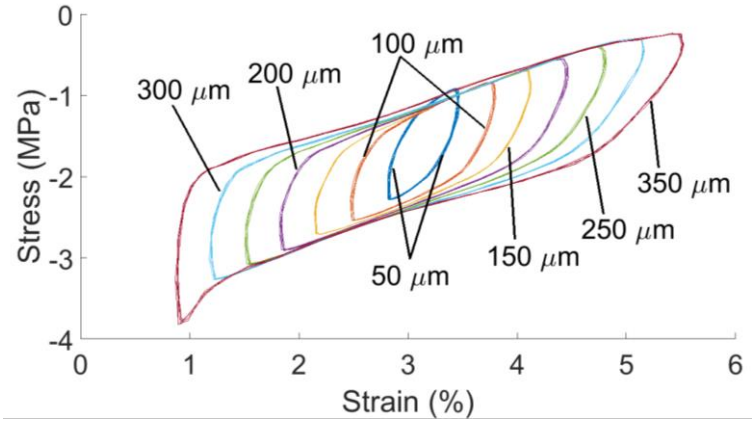

Figure 3.5 Stress vs. Strain curves recorded at 50 Hz, with 0.4 T applied field and stroke varying from 50 to 350 µm. Each loop contains data of ten full loading cycles. The piezoelectric force transducer measures relative stress, not absolute stress. The relative stress from the transducer was shifted to the appropriate compressive stress by performing a manual test using the compression from the LVDT and spring constant of springs in Figure 1.

The stress was calculated based on data from a piezoelectric force transducer. This device measures the relative force, not the absolute force. A stress strain curve was taken manually with an external field of 0.4 T; we determined the stress from the LVDT displacement and spring constant of springs on each side of the motor, and strain from the difference of the micrometer displacement and LVDT displacement. The stress data from the force transducer was shifted such that the data point at the maximum stress coincided with the stress at that strain value from the manual test.

3.5 Analysis of Results

The ratio of the output to input amplitude varied with the strain on the sample (Figure 3.4d). The magnitude of this ratio with time (Figure 3.4b) was in phase with the strain of the sample (Figure 3.4c). With less strain, the volume fraction of twin variant with high magnetic susceptibility parallel to loading and the axis of the coil increased. Larger susceptibility and permeability of the sample in the axis of the coil resulted in greater mutual inductance between the drive and pickup coils and larger voltage amplitude on the pick-up coil at the same input voltage amplitude. There was a consistent dependence of the RMS voltage ratio on the strain of the sample (Figure 3.4d); the ratio at discrete strain values was consistent during many loading-unloading cycles of the sample.

The magnetic field was varied from 0.8 T (0.64 MA/m) down to 0.2 T (0.16 MA/m) in 0.1 T (0.08 MA/m) increments at 50 Hz and 150 μm amplitude (Figure 3.6a). Though 0.2 T was below the initially measured switching field, the sample fully recovered the mechanical stroke. Thus, repeated cycling trained the sample, which reduced the twinning stress and lowered the switching field below 0.2 T. The range of RMS ratio was greater for lower applied magnetic fields (Figure 3.6b). The perpendicular magnetic field applied to elongate the sample worked to demagnetize the sample perpendicular to the axis of the coil, which resulted in a lower net change in magnetization between variants [1]. A larger net change in magnetization yields the largest difference in voltage amplitude and better resolution of the sample strain.

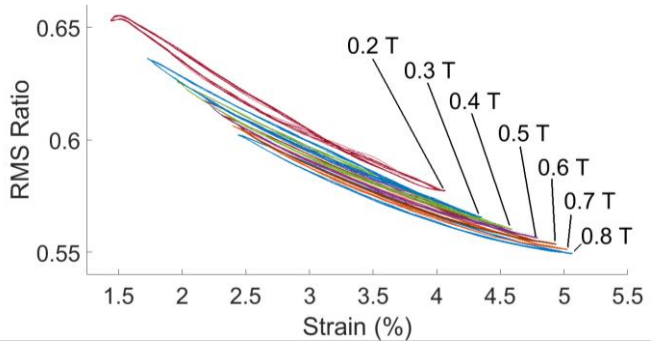

Figure 3.6 RMS ratio vs. Strain was taken for magnetic fields from a maximum of 0.8 T down to 0.2 T. The inset shows the ratio range (maximum – minimum). The full scale of the ratio decreases with increasing perpendicular field.

A larger RMS ratio range gave a higher strain-sensing resolution, meaning that a small perpendicular field would be optimal because a lower field has larger change in the RMS voltage ratio. In order to keep a constant field throughout the remaining tests, we chose a perpendicular field of 0.4 T to stay well above the switching field. The magnetic field elongated the sample below the initial measured switching field because actuating the sample leads to magneto-mechanical training, effectively decreasing the twinning stress [18].

While varying the motor frequency at a constant applied magnetic field and cyclic stroke, the loading portion of the RMS voltage-strain relationship deviated from the unloading portion (Figure 3.7a). The integrated area of the curve, or hysteresis, increased as the frequency increased (Figure 3.7b). The hysteresis increased nearly linearly with increasing frequency; the hysteresis at 25 Hz slightly deviated from this relationship. The resonant frequency of the motor was close to 75 Hz; as the frequency deviated from resonance, the strain became less sinusoidal and multiple harmonics of the frequency were included. The higher harmonics increased the strain rate, resulting in larger hysteresis than would be expected for a sinusoid with only the fundamental harmonic. Using the data points from 50, 75, and 100 Hz, a linear fit extrapolated to zero hysteresis

occurs at -2 Hz. This verifies that close to static deformation, little or no hysteresis occurs in the loading and unloading curves as shown in the static test.

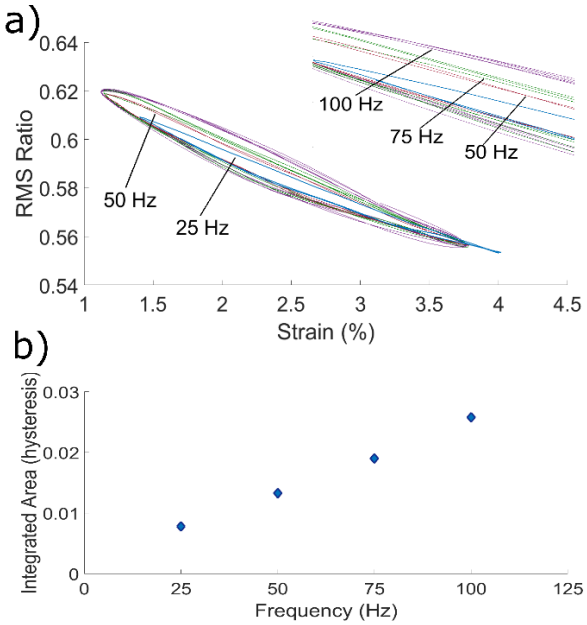

Figure 3.7 As the frequency increases, the slope of the linear fit increases by 15% while the voltage intercept decreases by less than 2%. The dependence of the slope on the magnetic field is consistent across all frequencies tested, with slope increasing with magnetic field. The slop of the fit for 100 Hz at 0.3 T decreases because the magnetic field does not accelerate the strain of the sample as quickly as the motor unloads the sample.

The hysteresis also increased with increasing stroke. The static test is depicted by the dashed black line in Figure 3.8. The unloading curve for each stroke matches the static test relationship, but the loading curve deviates from the static test due to hysteresis. The hysteresis increased non-linearly with increasing stroke. The hysteresis at 4.00% strain, or 300 μm, deviated from the otherwise systematic trend of the hysteresis. In this test, the sample reached the compressive limit of twinning strain, resulting in the deviation in the voltage-strain relationship at small strain values. This was seen in the stress-strain curves measured by the MMTA; a large increase in stress indicated that portion of the strain was due to compression of the springs and not the sample.

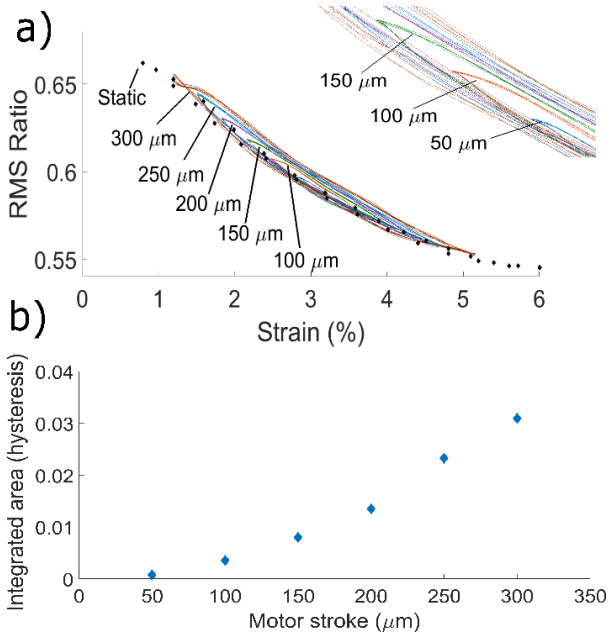

Figure 3.8 At a constant actuation frequency of 50 Hz and applied magnetic field of 0.4 T, the hysteresis in the RMS-strain relationship increases quadratically with increasing strain.

Using Matlab, we fit a linear function to the logarithm of the integrated area *vs.* the logarithm of the stroke. The slope of the linear fit was 2.05, meaning the dependence of the hysteresis on stroke was quadratic.

3.6 Discussion

The results show a non-linear dependence of the voltage on the strain, with hysteresis between the loading and unloading curves. This is in contrast to Müllner *et al.* 2003, where the static dependence of the flux density on the strain was linear and without hysteresis.

Müllner *et al*. used an orthogonal magnetic field of 0.7 T, near the saturation field. The domains with axis of easy magnetization parallel to the field were saturated and those with axis of hard magnetization parallel to the magnetic field were nearly saturated. In this experiment, the alternating current carried by the drive coil resulted in a varying flux density, which reached a maximum of approximately 15 mT. Also, Müllner *et al.*

measured the flux density of two twin domains oriented in parallel. The flux density in the present experiment passed through domains oriented in series. Due to the continuity of flux density at domain boundaries, domains oriented in parallel have a different flux density response than those oriented in series [15,19].

The demagnetizing (internal) field may cause the non-linearity seen in the experiment. Consider an element with one twin boundary and two domains (Figure 3.9). The black line denotes the direction of the axis of easy magnetization in each domain. The axis of the coils lies in the *x* direction and the external magnetic field in the *y* direction. The external field magnetizes the A domain at an angle α from the *x* direction, reducing the magnetization in the *x* direction. The magnitude of the RMS voltage of the pickup coil depends on the magnitude of magnetization in the *x* direction. At large strains, the A domain is small. The demagnetizing factor in the A domain is small, resulting in large α and smaller magnetization in *x*. At small strains, the A domain is large (wide). The demagnetizing factor in the A domain is large, resulting in small α and larger magnetization in *x*. Instead of a linear dependence of RMS amplitude on strain, the amplitude in domain A is larger at small strain and smaller at large strain due to changes in domain geometry and internal field magnitude.

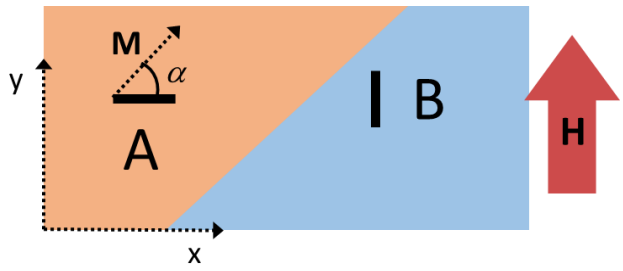

Figure 3.9 A sample is depicted containing one twin boundary and two twin domains, A and B, with axis of easy magnetization in the *x* and *y* direction, respectively. The external magnetic field is parallel to the *y* direction, and the axis of the coils is parallel to the *x* direction. The external magnetic field causes the magnetic moments in domain A to rotate at an angle *α* away from the axis of easy magnetization.

The loading portion of the dynamic tests matched that of the static test. The unloading portion, where the external field drove twin boundary motion, contained hysteresis. The hysteresis increased linearly with increasing frequency and quadratically with increasing stroke. The magnitude of the hysteresis was not only due to the velocity of twin boundary motion; the twin boundary velocity increases linearly with both frequency and stroke. The hysteresis depended on the distance through the material the twin boundary moved.

Assuming exactly one twin boundary existed in the material, at the maximum stroke of 300 μm, the twin boundary moved approximately 5 mm. A frequency of 100 Hz and stroke of 300 μm resulted in a maximum twin boundary velocity of 1.6 m/s, assuming sinusoidal actuation. Most likely, multiple twin boundaries existed, which implies a smaller velocity. Reported values of twin boundary velocity vary from ~1 m/s [20,21] to 82.5 m/s [22]. If there was only one twin boundary and the twin boundary velocity in our experiment more closely matched those measured by Faran *et al.*, the magnetic field-induced twin boundary motion may have been slower than the motor, resulting in inaccurate strain measurement. This was possible since the sample glued only

on one side and free on the other side such that upon mechanical unloading, the sample may have detached from the sample holder. If the twin boundary velocity closely matched that measured by Smith *et al*., the rate of twin boundary motion strained the material fast enough to match the motor actuation. If a large number of twin boundaries were present such as in densely twinned crystals, twin boundary velocities measured by Faran *et al.* and Smith *et al.* suffice to deform the sample at the speed of actuation.

The strain-voltage hysteresis increases with increasing frequency and tends to zero as the frequency approaches zero. This means no hysteresis exists in a static application of the sensor, which agrees with the static test. The hysteresis occurs in the elongation/tensile portion of the stress-strain curve, which is the portion of the curve when the sample is being actuated magnetically. If the sample is glued or otherwise affixed to the deforming medium and no external field is needed, the hysteresis would possibly vanish. Thus, the hysteresis may indicate that the twin boundary velocity was not sufficient to deform the sample at the rate of mechanical unloading.

This sensing method does not require a large external magnetic field to measure the magnetic properties as in other sensing methods of magnetic shape memory alloys. The measurement could be made in a small, low power configuration. Since a large net magnetic field is not required to measure the strain, strain sensing with this method can be done in all three dimensions at once. Twin domains with easy axis parallel to any orthogonal direction in Cartesian coordinates can exist. The magnetic properties of the sample will change in three dimensions depending on the three dimensional strain state. Using a dual coil setup around each principal axis of a parallelipedal sample, the same measurement can be done in three dimensions. Currently, it is not possible to measure

strain in three dimensions with one device. This material and configuration make this possible.

The change in RMS voltage across the full strain range was approximately 10% of the largest voltage, and the configuration has not been fully optimized. The resistance of a traditional strain gauge is only a fraction of a percent. The drawback of this method is that the contribution of the internal field varies, and the configuration may need more calibration than other methods.

3.7 Summary and Conclusion

The amplitude of the voltage across the pickup coil decreased by 17.7% as the tensile strain increased by 5.2% during manual unloading. The hysteresis in the voltage-strain relationship between the loading and unloading curves was minimal when the strain was varied manually. When the sample was actuated with the motor, the loading (compression) portion of the voltage-strain relationship matched closely the relationship of the static manual test. The unloading portion deviated from this relationship resulting in hysteresis. The hysteresis increased with increasing strain rate, either by increasing the frequency or stroke at which the motor operated.

The strain sensing resolution is defined by the change in RMS ratio to the strain of the sample. The best resolution occurs when the change in voltage is the greatest. The excitation voltage frequency was optimized to maximize the voltage change. Tests showed that in order to fully maximize the voltage change, the smallest orthogonal magnetic field should be used.

The strain sensing system (MSM element and dual-coil) did not require the use of a large permanent magnetic field, and instead utilized a varying AC voltage with 400 mV

amplitude. The proposed sensing system works best in an environment when the strain does not change rapidly, such as to decrease the hysteresis between loading and unloading curves. Also, the system would be optimized if the sample is physically adhered to the deforming substrate in question, thus not requiring an external magnetic field.

The magnetic susceptibility varies in all three dimensions as a function of the three dimensional strain state. This strain measurement configuration could be expanded with a dual-coil in each dimension to measure strain in all three dimensions with one piece of material.

3.8 Acknowledgements

We thankfully acknowledge funding through the Idaho State Board of Education, Higher Education Research Council project IF-15-003.

3.9 References

[1] P. Müllner, V. Chernenko, G. Kostorz, Stress-induced twin rearrangement resulting in change of magnetization in a Ni-Mn-Ga ferromagnetic martensite, Scr. Mater. 49(2) (2003) 129-133.

[2] A. Sozinov, N. Lanska, A. Soroka, L. Straka, Highly mobile type II twin boundary in Ni-Mn-Ga five-layered martensite, Appl. Phys. Lett. 99(12) (2011).

[3] L. Straka, N. Lanska, K. Ullakko, A. Sozinov, Twin microstructure dependent mechanical response in Ni-Mn-Ga single crystals, Appl. Phys. Lett. 96(13) (2010).

[4] D. Kellis, A. Smith, K. Ullakko, P. Müllner, Oriented single crystals of Ni-Mn-Ga with very low switching field, J. Cryst. Growth 359 (2012) 64-68.

[5] E. Pagounis, R. Chulist, M.J. Szczerba, M. Laufenberg, Over 7% magnetic field-induced strain in a Ni-Mn-Ga five-layered martensite, Appl. Phys. Lett. 105(5) (2014).

[6] A. Sozinov, A. Likhachev, N. Lanska, K. Ullakko, V. Lindroos, 10% magnetic-field-induced strain in Ni-Mn-Ga seven-layered martensite, J. Phys. IV 112 (2003) 955-958.

[7] P. Müllner, V. Chernenko, G. Kostorz, Large cyclic magnetic-field-induced deformation in orthorhombic (14M) Ni-Mn-Ga martensite, J. of Appl. Phys. 95(3) (2004) 1531-1536.

[8] O. Heczko, Magnetic shape memory effect and highly mobile twin boundaries, Mat. Sci. Tech. Ser. 30(13A) (2014) 1559-1578.

[9] I. Suorsa, J. Tellinen, K. Ullakko, E. Pagounis, Voltage generation induced by mechanical straining in magnetic shape memory materials, J. Appl. Phys. 95(12) (2004) 8054-8058.

[10] I. Karaman, B. Basaran, H. Karaca, A. Karsilayan, Y. Chumlyakov, Energy harvesting using martensite variant reorientation mechanism in a NiMnGa magnetic shape memory alloy, Appl. Phys. Lett. 90(17) (2007).

[11] N. Sarawate, M. Dapino, Experimental characterization of the sensor effect in ferromagnetic shape memory Ni-Mn-Ga, Appl. Phys. Lett. 88(12) (2006).

[12] I. Suorsa, E. Pagounis, K. Ullakko, Magnetization dependence on strain in the Ni-Mn-Ga magnetic shape memory material, Appl. Phys. Lett. 84(23) (2004) 4658-4660.

[13] N. Sarawate, M. Dapino, Dynamic sensing behavior of ferromagnetic shape memory Ni-Mn-Ga, Smart Mater. Struct. 18(10) (2009).

[14] J. Stephan, E. Pagounis, M. Laufenberg, O. Paul, P. Ruther, A Novel Concept for Strain Sensing Based on the Ferromagnetic Shape Memory Alloy NiMnGa, IEEE Sens. J. 11(11) (2011) 2683-2689.

[15] I. Suorsa, E. Pagounis, K. Ullakko, Position dependent inductance based on magnetic shape memory materials, Sensors Actuat. A-Phys. 121(1) (2005) 136-141.

[16] A. Saren, D. Musiienko, A.R. Smith, J. Tellinen, K. Ullakko, Modeling and design of a vibration energy harvester using the magnetic shape memory effect, Smart Mater. Struct. 24(9) (2015).

[17] P. Lindquist, P. Müllner, Working Ni-Mn-Ga Single Crystals in a Magnetic Field Against a Spring Load, Shap. Mem. Superelast. (2015).

[18] M. Chmielus, I. Glavatskyy, J.-U. Hoffmann, V.A. Chernenko, R. Schneider, P. Müllner, Influence of constraints and twinning stress on magnetic field-induced strain of magnetic shape-memory alloys, Scr. Mater. 64(9) (2011) 888-891.

[19] N. Gabdullin, S.H. Khan, Study of Non-Homogeneity of Magnetic Field Distribution in Single-Crystal Ni-Mn-Ga Magnetic Shape Memory Element in Actuators Due to Its Anisotropic Twinned Microstructure, IEEE T. Magn. 53 (3) (2017).

[20] E. Faran, D. Shilo, The kinetic relation for twin wall motion in NiMnGa, J. Mech. Phys. Solids 59(5) (2011) 975-987.

[21] E. Faran, D. Shilo, The kinetic relation for twin wall motion in NiMnGa-part 2, J. Mech. Phys. Solids 61(3) (2013) 726-741.

[22] A.R. Smith, J. Tellinen, K. Ullakko, Rapid actuation and response of Ni-Mn-Ga to magnetic-field-induced stress, Acta Mater. 80 (2014) 373-379.

CHAPTER FOUR: MAGNETIC TORQUE IN SINGLE CRYSTAL NI-MN-GA

This chapter is published by Springer in *Shape Memory and Superelasticity* and should be referenced appropriately.

Reference:

A. Hobza and P. Müllner, Magnetic torque in single crystal Ni-Mn-Ga, Shape Memory and Superelasticity (2017) 3:139-148. DOI: 10.1007/s40830-017-0106-3

Anthony Hobza [1]

Peter Müllner [1]

Published in:

Shape Memory and Superelasticity

May 2017

[1] Micron School of Materials Science and Engineering, Boise State University, Boise, ID 83725, USA

4.1 Abstract

Magnetic shape memory alloys deform in an external magnetic field in two distinct ways, namely axial straining – known as magnetic-field-induced strain – and bending. Here, we examine the magnetic torque that a magnetic field exerts on a long Ni-Mn-Ga rod. A single crystal specimen of Ni-Mn-Ga was constrained with respect to bending and subjected to an external field. The torque required to rotate the specimen in the field was measured as a function of the orientation of the sample with the external field, strain, and the magnitude of the external field. The torque was analyzed based on the change in the free energy with the angle between the field and sample. The contributions of magnetocrystalline anisotropy and shape anisotropy to the Zeeman energy determine the net torque. The torque is large when magneotcrystalline and shape anisotropies act synergistically and small when these anisotropies act antagonistically.

4.2 Introduction

Magnetic shape memory alloys (MSMAs) change shape when exposed to a mechanical stress or a magnetic field [1]. The shape change results from a re-orientation of the unit cell via motion of twin boundaries. The most widely studied magnetic shape memory alloy, monocrystalline Ni-Mn-Ga, has a monoclinic martensite structure with 10M lattice modulation. The lattice is often approximated as tetragonal with $c < a$. The maximum strain is 1-c/a, which is approximately 6%. At 0% strain the materials is a single domain with c parallel to the strain direction, and at 6% strain the materials is a single domain with c perpendicular to the strain direction.

Martensitic Ni-Mn-Ga has uniaxial magnetic anisotropy with the axis of easy magnetization parallel to c, the short axis of the unit cell. The easy axis of magnetization

changes across a twin boundary. If an external magnetic field is not parallel to the easy axis of a domain, the magnetic field imposes a magnetostress in that domain [2]. If the magnetostress is larger than the twinning stress, the twin boundary will move. The twin domain with axis of easy magnetization most parallel to the external field grows.

The magnetic-field-induced shape change of a MSM element enables contact-free actuation without moving parts. Since the sample length determines stroke, a long element maximizes the stroke and work output of the material. Long samples tend to bend when a uniform magnetic field is applied perpendicular to the long dimension [3-5]. When bent, MSM elements may contact guide walls which results in friction and a reduction of axial strain [3]. Though bending is a natural deformation mode of a long MSM element in a magnetic field, studies on the magneto-mechanical properties of magnetic shape memory alloys focus on magnetic-field-induced strain (MFIS) and often neglect magnetic-torque-induced bending (MTIB).

MTIB was reported in a non-uniform magnetic field [6]. The authors noted that, even in a uniform field, the magnetic and shape anisotropies would lead to a torque on the sample. MTIB was reported in a uniform field for wires with sub-millimeter diameter by Zheng et al. [4] who attributed it to the difference in Zeeman energy depending on the orientation of the sample. Kucza et al. studied bending in single crystal beams with 1 mm2 cross sectional area and various lengths, and found that the amount of bending depended on the beam's aspect ratio, while the axial strain did not depend on the sample length [5]. The authors attributed the bending strain to torque introduced by the Zeeman, shape anisotropy, and magnetocrystalline anisotropy energies [4,5].

In both studies, sample bending was attributed to differences in the magnetic energy depending on the orientation of the sample in the external magnetic field. The relative contributions of the energies to torque was qualitatively discussed [5] based on the sample behavior in different magnetic field strengths. MSM alloys may be used in various shapes, sizes, and magnetic field strengths. A quantitative understanding of the contributors to this torque is necessary to understand the response of actuating elements to a variable magnetic field.

Several studies applied free energy functions to describe the driving force behind twin boundary motion [7-9] as well as the dependence of the critical field on the geometry of domains due to demagnetization [10]. The energy functions contain the contributions described above as well as external stress and magnetoelasticity. The studies quantitatively describe or analytically calculate the contribution of each energy term to the equilibrium of the twin domains, but do not consider the torque imposed on a sample by these energies.

O'Handley et al. [11] calculated the torque on an unfavorably oriented domain in an external magnetic field in order to describe the driving force for twin boundary motion. The contributions of the external field and magnetocrystalline anisotropy to the torque on the unfavorable twin domain were related to the shear stress at the twin boundary. In their theoretical approach, these authors considered torque as it relates to twin boundary motion in a specimen which is constrained on its ends such that it can deform only by straining. They did not discuss the total torque on a specimen without these constraints, such as in the experiments in Refs. 4 and 5. Additionally, only one

orientation of the applied field with the specimen was considered in contrast with the rotating field in Refs. 4 and 5.

This study examines experimentally the torque of a Ni-Mn-Ga specimen constrained with respect to bending strain in a magnetic field and explores the causes for this torque. The torque as a function of angle with the magnetic field was measured and compared to the same test using a soft magnetic material and a permanent magnet as references. We discuss the contributions of the torque in terms of the external field energy, magnetocrystalline anisotropy energy, and internal field energy.

4.3 Experimental Procedure

Single crystal specimen of Ni-Mn-Ga were grown with a modified Bridgeman-Stockbarger technique [12]. Specimen were grown with a nominal composition of Ni50.5Mn27.75Ga21.75 (atomic percent); however, due to chemical segregation during growth there was a composition gradient across the crystal resulting in sections with different martensite structures at room temperature. Crystals were characterized in a Hitachi S3400 scanning electron microscope with energy dispersive x-ray spectroscopy (EDS, Oxford Instruments Energy+ detector) and a Bruker D8 X-ray diffractometer with a Cu K_α source. Samples were cut with a Princeton Scientific WS-22 wire saw with a 50 μm diameter tungsten wire and polished using successively smaller grit SiC paper and then diamond slurries down to 1 μm diameter diamonds. The Ni-Mn-Ga sample tested had 10M structure with composition Ni51.1Mn25.7Ga23.2 (atomic percent, as determined with EDS with accuracy atomic percent) and measured 20.02 x 5.02 x 3.62 mm3 fully extended in the longest dimension and compressed in the intermediate dimension. The sample was subjected to constant magnetic fields between 25 and 150

milli-Tesla (mT) in a Varian Associates V3603 electromagnet. Once the samples had reached an equilibrium angle with the external magnetic field, a torque was applied as described below and the angular deflection was measured.

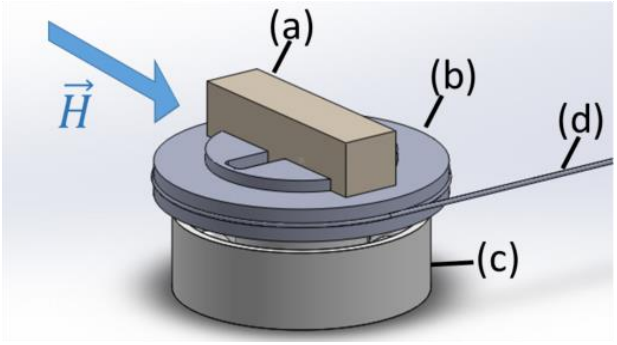

Figure 4.1 The magnetic samples (a) were placed in a round Teflon sample holder (b). The sample holder had a shoulder machined to press-fit into the inner bore of a non-magnetic ZrO2 ceramic bearing (c). A groove was machined at the circumference and a string (d) was wrapped around the sample holder in this groove. The string was connected to a spring force gauge (not shown) to apply a tangential force (torque) to the sample holder and sample.

A sample holder made from Teflon contained a groove to accommodate the sample (Figure 4.1). The sample holder had a diameter of 25.4 mm on which the sample was laid and a shoulder with a smaller diameter of 9.53 mm which was press-fit into the inner bore of a ZrO_2 non-magnetic bearing (Figure 4.2a). The bearing was placed in Styrofoam between the pole pieces of an electromagnet (Varian Associates V3603). The angle of the sample with the magnetic field γ was measured by taking pictures using a Canon PowerShot A3000 digital camera and comparing the edge of the sample to a compass aligned in the field (Figure 4.2a) using the angle tool in ImageJ. We define Cartesian coordinates such that the *x* direction coincides with the long edge of the sample and the rotation axis constitutes the *z* direction. The angle γ describes the deviation of the magnetic field direction from the x direction. When the magnetic field was parallel to the *x* direction $\gamma = 0°$. The angular error was less than 0.5°. The sample holder had a groove

cut around the circumference where a string was wrapped around and extended to a spring force gauge (PCE Instruments) and pulley. The string transferred a displacement of the pulley to apply a tangential force to the sample holder and, thus, a torque to the sample.

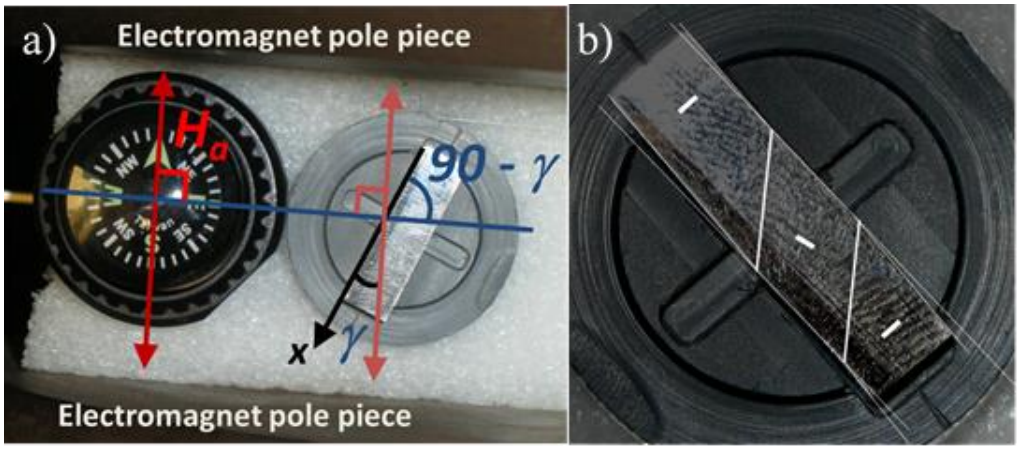

Figure 4.2 (a) A digital image was captured using a Canon PowerShot A3000 digital camera. A compass was placed in between the poles of the electromagnet. The North-South pole aligned parallel to the magnetic field, and the East-West pole was perpendicular to the magnetic field. Using the angle tool in ImageJ, the angle γ between the poles of the compass and the x axis of the sample was measured. The magnetic field direction is the reference direction and γ increases clock wise. (b) White lines highlight the kink between adjacent domains. Lines across the sample connect the kinks on the surfaces and indicate the location of twin boundaries. Thick white lines in each domain denote the direction of the easy axis of magnetization.

Two spring force gauges from PCE Instruments were used alternatively, with maximum forces of 10 g (0.098 N) and 1 N and resolution of 0.001N and 0.01 N respectively. For experiments with a magnetic field of 25 mT and for tests with a magnetic field of 50 mT and strain equal to or larger than 5%, the maximum force to fully rotate the sample was less than 0.098 N. For these experiments, we measured the torque with the 10 g force gauge. For all other experiments, we applied the 1 N force gauge.

The sample was tested with a constant twin structure throughout each experiment. The sample contained three twin domains with two twin boundaries, such that the center domain had the easy axis in the x direction. Figure 4.2b outlines the edges of the sample with light-colored lines, showing the kink between the domains. The approximate locations of the two twin boundaries between the domains are given by the lines running at a 45 degree angle to the sample edges. Twin boundaries intersect the location of the kinks on either side of the sample. The thick white lines in the domains give the directions of the c axis in each domain. The image in Figure 4.2b depicts a sample at 4% strain, which would correspond to the domain with c parallel to x making up one third of the sample. This is visually verified in Figure 4.2b. The resolution of the angle measurement in ImageJ was approximated by measuring the angle between the edges of the two domains, and comparing compared to the expected angle from lattice parameters.

We set the strain on the sample and then placed it into the sample holder with the magnetic field turned off. Then we increased the field to the set point of interest. Once at the field set point, we measured the equilibrium angle of the sample with the magnetic field direction without applying a force to the string. Then, with the sample in a constant magnetic field, we increased the force on the spring gauge manually to apply torque to the sample holder. We took pictures to measure the resulting angle between the sample and the field at discrete force values. Upon exceeding the position of maximum torque, the mechanical loading system became unstable and the sample holder spun uncontrolled. Thus, no data was collected at angles greater than the angle of maximum torque.

We performed experiments first with the fully extended sample (*i.e.* at 6% strain) at magnetic fields of 25, 50, 75, 100, 125, and 150 mT. Between the experiments at

different fields, we turned the field to zero, checked the sample strain and re-wound the string around the sample holder. We then compressed the sample to 5% strain and conducted experiments at multiple magnetic fields. This process was repeated for multiple fields at integer values of strain (0-6%). At 100 mT, twin boundaries moved for strains lower than 3%, which changed the strain. Therefore, data below 3% strain at 100 mT and fields higher than 100 mT was not measured. We assume that the repeated straining of the sample required to properly establish each strain state caused a softening of the material which resulted in reducing the switching field [13] to below 100 mT. This is known as training and often applied intentionally to reduce the twinning stress [14]. Additionally, the equilibrium angle as a function of strain at 50 mT external magnetic field was found in strain increments of 0.5%.

4.4 Results

The equilibrium angle γ_{eq} (*i.e.* at zero torque) was measured as a function of strain at different magnetic fields (Figure 4.3). The amount of strain changed the equilibrium angle. At 0% strain (*i.e.* when the easy direction of magnetization was parallel to the longest axis of the sample), the equilibrium angle was 0°. With increasing strain, the equilibrium angle increased non-linearly and reached 90° when the sample was fully extended (*i.e.* at 6% strain). The equilibrium angle did not depend on the field strength except at 3% strain where the value for 100 mT deviated from those at 50 and 75 mT.

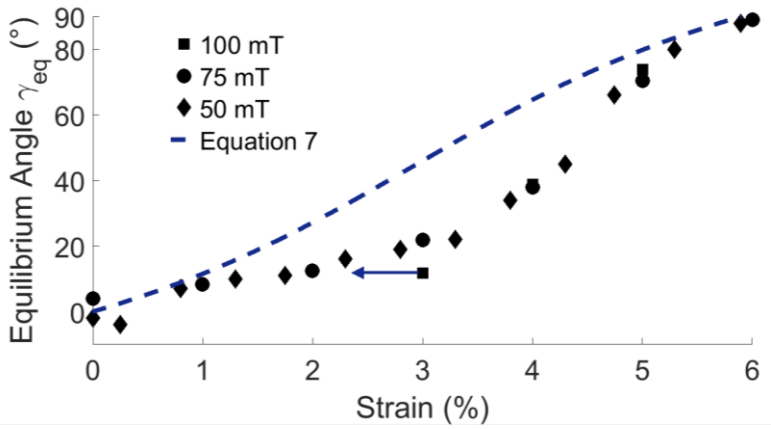

Figure 4.3 Equilibrium angle γ_{eq} between the sample's long axis and magnetic field as a function of strain at different magnetic fields. At 100 mT, twin boundaries moved for strains higher than 3% and so data past 3% was not obtained. The arrow shows the strain for the data point at 3% strain and 100 mT may have decreased, changing the equilibrium angle. Equation 7 is plotted as a dashed line.

We derived the torque from the force measurements by multiplying them by the radius of the sample holder (Figure 4.1). Figure 4a shows the torque at 6% strain as a function of γ and different magnetic fields (Figure 4.4a). The tests started at or near -90 degrees as this was the equilibrium angle for 6% strain independent of external field (Figure 4.3). The torque increased until the sample spun in the magnetic field to another equilibrium angle 180 degrees from the initial starting point. At low magnetic field (particularly at 25 mT) friction impeded the smooth motion of the sample holder and caused large jumps in angle. The torque required to rotate the sample increased with increasing magnetic field such that friction was negligible at fields of 50 mT and above. For example, the maximum torque measured at 25 mT was 0.19 mNm while the maximum torque at 150 mT was 5.9 mNm, an increase by a factor of 31. The torque as a function of external field at -75°, -60°, and -45° is given in Figure 4.4b. The method used to interpolate torque values at these discrete angles is given in Section 4.4. The torque needed to rotate the sample increases non-linearly with external field for each angle.

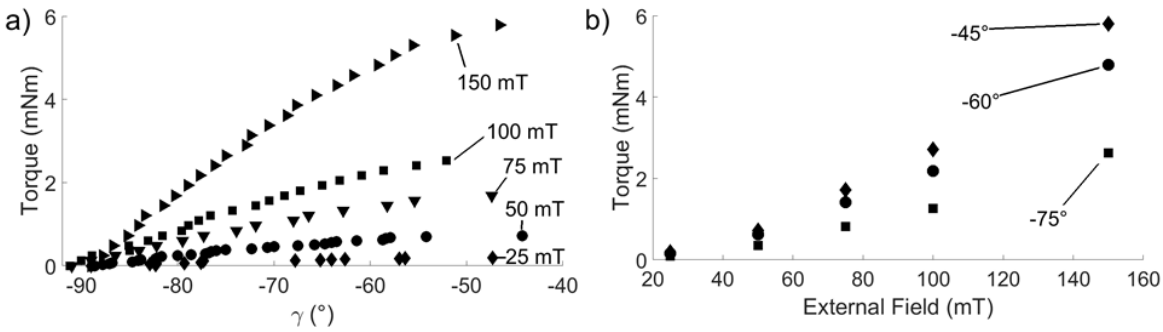

Figure 4.4 (a) Torque as a function of angle γ between the sample's long axis and magnetic field at 6% strain for different applied magnetic fields. (b) Interpolated torque values from empirically fit equations as a function of external field at -75°, -60°, and -45°.

Figure 4.5 shows the torque as a function of γ at a magnetic field of 75 mT and different strains. The equilibrium angle shifted to larger values with increasing strain according to the results shown in Fig. 4.3. For each strain, the torque increased with increasing angle though with regressing slope. The slope of the torque vs. angle curves decreased with increasing strain such that the maximum torque at 0% strain was 10.1 mNm and decreased to 1.72 mNm at 6% strain, a decrease by a factor of 5.87.

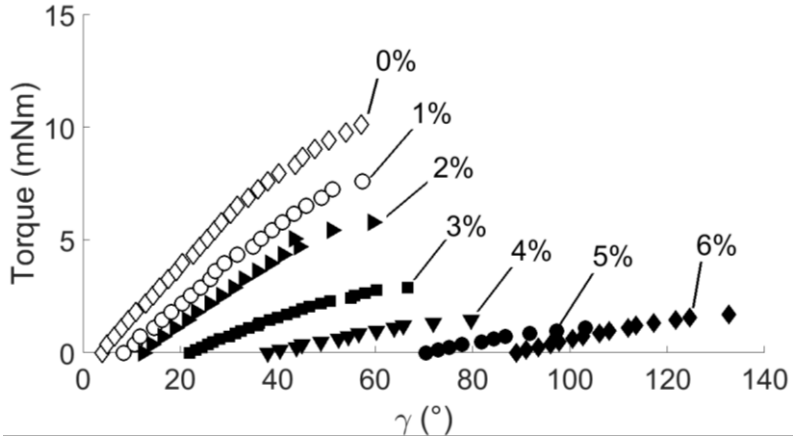

Figure 4.5 Torque as a function of angle γ between the sample's long axis and magnetic field at 75 mT applied field for different values of strain. The maximum measured torque decreased by a factor of 6 from 0% to 6% strain.

4.5 Discussion

The total magnetic energy of a specimen is the sum of the exchange energy (E_{ex}), the magnetocrystalline anisotropy energy (E_{anis}), the energy of the magnetized sample in an external field, also known as the Zeeman energy (E_Z), and the energy of the magnetized sample in its own internal field created by the net magnetization, often referred to as the shape anisotropy energy (E_{int}). The exchange energy causes the magnetic moments to align parallel (*i.e.* ferromagnetically). The magnetocrystalline anisotropy energy results from the symmetry of the crystal lattice and effectively keeps the magnetization vector parallel to the easy axis of magnetization. Ni-Mn-Ga with 10M martensite is uniaxially anisotropic and the crystallographic c direction is the direction of easy magnetization. The magnetocrystalline anisotropy energy depends on the angle between the magnetization vector and the c direction. The Zeeman energy is the dot product of the magnetization vector and external magnetic field vector. The magnetic poles of a magnetized specimen create an internal magnetic field, which opposes the external field and is a function of sample geometry. The total energy is given by

$$E_{\text{total}} = E_{\text{ex}} + E_{\text{anis}} + E_{\text{Z}} + E_{\text{int}} \tag{4.1}$$

All energy terms are given as energy densities referring to the sample volume. The magnetic moments orient such as to minimize E_{total}. The total magnetic energy is a function of the angle of the external magnetic field with the sample. The negative first derivative of the total magnetic energy with respect to the angle γ between the field and sample (Figure 4.2a) gives the torque on the sample due to the magnetic energy:

$$\theta = -dE_{\text{total}}/d\gamma \tag{4.2}$$

The equilibrium angle of the specimen in the external magnetic field is the angle at which the torque on the specimen is zero; it is the angle at which the magnetic energy is minimal.

As stated by Liang et al [6] and Kucza et al. [5], the torque on a specimen is governed by the Zeeman, magnetocrystalline and shape anisotropy energies. The specimen had three domains and two twin boundaries. The axis of easy magnetization changed across each twin boundary, and each domain had a different shape anisotropy energy. As the strain of the sample changed so did the relative sizes of each domain. The shape anisotropy for each domain was different at each strain value resulting in the variation of the equilibrium angle in Figure 4.3. The equilibrium angle did not depend on the field strength except at 3% strain where the value for 100 mT deviated from those at 50 and 75 mT. We assume that this deviation resulted from the small movements of twin boundaries (as described in the experimental section). Thus, the actual strain value of that sample was less (as indicated by the arrow in Figure 4.3).

The torque as a function of angle for external fields ranging from 25 mT to 150 mT is plotted in Figure 4.4a. A sine function for each external field was empirically fit to the torque values. The values of torque for -75°, -60°, and -45° at each external field were interpolated from the fitting functions. These torque values are plotted in Figure 4.4b as a function of the magnetic field. The torque magnitude has a non-linear dependence on the external field magnitude. In order to find this dependence, a linear equation was fit to the logarithm of torque as a function of the logarithm of external field. The slope of the relationship for each angle was 1.88 ± 0.02. The power dependence of the torque on magnetic field is slightly less than quadratic.

The maximum torque measured on the sample changed by a factor of 5.87 between single variant states. The major difference in these two cases is the shape anisotropy of the domain and resulting internal field. We can define the internal field with a demagnetization factor (Section 4.4.3). The larger the demagnetization factor, the larger the internal field. At 0% strain, the single domain has easy axis of magnetization parallel to the long dimension, which has a small demagnetization factor of about 0.093 [15]. At 6% the easy axis is parallel to the sample dimension with a larger demagnetization factor of about 0.386 [15]. The ratio of large demagnetization to small demagnetization is 4.15.

4.5.1 Zeeman Energy

A magnetic material in an external magnetic field (Figure 4.6) has a net magnetization, **M** with magnitude *M*. The angle γ is the angle between the longest axis of the sample (which is also the *x* direction) and the magnetic field, and α is the angle between the magnetization vector and the sample's longest axis.

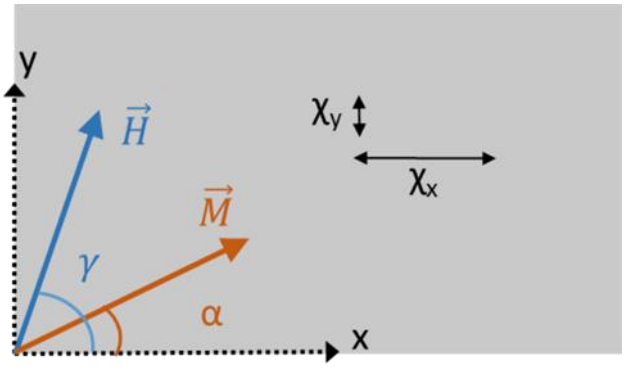

Figure 4.6 A magnetic material subjected to an external magnetic field at an angle γ to the sample edge experiences a magnetization M at an angle α to the sample edge.

In a soft, magnetically anisotropic material, such as Ni-Mn-Ga, at low magnetic field the magnetic anisotropy energy holds the direction of magnetization nearly parallel

to the easy axis of magnetization. (Ni-Mn-Ga saturates at fields well below the external fields used in the experiment.) When saturated in the easy axis the Zeeman energy is

$$E_Z = -\mu_0 M_s H|\cos(\gamma - \alpha)| \tag{4.4}$$

A soft magnet will magnetize in both directions in the easy axis. This means the Zeeman energy is always negative, hence the absolute value of the cosine function. Equation 4.4 has 2 energy minima at $\gamma = 0°$ and 180°.

Figure 4.7 Specimen containing two domains, A and B, with easy axis of magnetization parallel to the *x* and *y* directions, respectively. As the strain is increased, the fraction of domain B increases and domain A shrinks.

Consider a Ni-Mn-Ga sample with 2 domains, A and B, where the easy axis of magnetization of domains A and B are parallel to the *x* and *y* directions (Figure 4.7). The fraction of each domain, f_A and f_B, depends on the overall strain of the sample. Zero strain corresponds to only domain A, or $f_A = 1$ and $f_B = 1 - f_A = 0$. Full strain (6% for 10M) corresponds to $f_B = 1$ and $f_A = 0$. For simplicity, we refer here to normalized strain $\epsilon = \varepsilon/\varepsilon_{max}$, such that $\epsilon = f_B$. Since the orientation of the easy axis of magnetization is different in each domain, the energy must be calculated for each domain individually. The total Zeeman energy for a specimen is:

$$E_Z = -\mu_0 M_s H[f_B|\sin(\gamma - \alpha)| + f_A|\cos(\gamma - \alpha)|] \tag{4.5}$$

Assuming α is small, the torque due to Zeeman energy (for brevity *Zeeman torque*, θ_Z)

$$\theta_Z = -\frac{dE_Z}{d\gamma} = \mu_0 M_s H[\epsilon(\sin\gamma + \cos\gamma) - \sin\gamma] \quad (4.6)$$

For the equilibrium angle, Equation 4.6 yields by setting $\theta_Z = 0$:

$$\gamma = \arctan(\epsilon/(1-\epsilon)) \quad (4.7)$$

Equation 4.7 is plotted in Figure 4.3. It accounts well for the equilibrium angle at small *(i.e.* compressed sample) and large (*i.e.* extended sample) strain but overestimates the equilibrium angle at intermediate strains.

The magnitude of the Zeeman torque depends on the amount of strain on the sample. The zero of the torque (equilibrium angle) in Equation 4.7 also depends on strain. The Zeeman torque has a maximum of $\mu_0 M_s H$ when $\epsilon = 0$ or 1. For an external field of 75 mT, the maximum torque density is 36 kNm/m^3.

4.5.2 Magnetocrystalline Anisotropy

Consider a material with uniaxial magnetic anisotropy, *i.e.* it has an easy axis of magnetization. Magnetizing the sample in a direction not parallel to the easy axis is unfavorable and has a positive energy. The energy density is represented by the product of the anisotropy energy constant K_U with the square of the sine of the angle α between the easy axis of magnetization and the direction of net magnetization (Figure 4.6):

$$E_{\text{anis}} = K_u \sin^2\alpha \quad (4.8)$$

For martensitic Ni-Mn-Ga with 10M structure the anisotropy energy constant K_u is 2.45x10^5 J/m^3 [16].

When a component of the magnetic field is perpendicular to the easy axis of magnetization, the magnetic moments rotate to reduce the angle to the magnetic field direction (Figure 4.6). The angle α varies with the magnitude and direction of the external magnetic field.

The magnetocrystalline anisotropy keeps the magnetic moment parallel to the easy axis. In an external field, the magnetization vector has an equilibrium position which is the angle α at which the total magnetic energy is minimal. The total magnetic energy is

$$E_{\text{total}} = -\mu_0 M_s H \cos(\gamma - \alpha) + K_u \sin^2\alpha \tag{4.9}$$

In order to find the equilibrium angle of the magnetization with the *x* axis α, we set the first derivative of Equation 4.9 with respect to α equal to zero and solve for α. With this angle we find the total magnetic energy density as a function of γ for domains A (c // x) and B (c // y) [17]:

$$E_{\text{MA}} = -\mu_0 M_s H \cos\gamma + \frac{1}{4K_u}(\mu_0 M_s H_a)^2 \sin^2\gamma \tag{4.10A}$$

$$E_{\text{MB}} = -\mu_0 M_s H \sin\gamma + \frac{1}{4K_u}(\mu_0 M_s H)^2 \cos^2\gamma \tag{4.10B}$$

We find the torque density due for each domain A and B with Eqs. 4.2 and 4.10:

$$\theta_{\text{MA}} = -\mu_0 M_s H \sin\gamma - \frac{1}{4K_u}(\mu_0 M_s H)^2 \sin 2\gamma \tag{4.11A}$$

$$\theta_{\text{MB}} = \mu_0 M_s H \cos\gamma + \frac{1}{4K_u}(\mu_0 M_s H)^2 \sin 2\gamma \tag{4.11B}$$

Equation 4.11 gives the torque density normalized by the sample volume for each domain. The relative size of each domain changes as the strain changes. In order to find the total torque density as a function of strain, the torque density in domain A is multiplied by the relative strain 1-ϵ = f_A and the torque density in domain B is multiplied by ϵ = f_B. The sum of the two torque densities results in the total torque due to the Zeeman and magnetocrystalline anisotropy energies as a function of the relative strain and γ:

$$\theta_{\text{MT}} = (\mu_0 M_s H)[\epsilon(\sin\gamma + \cos\gamma) - \sin\gamma] + \frac{1}{4K_u}(\mu_0 M_s H)^2 \sin 2\gamma\,(2\epsilon - 1) \tag{4.12}$$

The first term in Equation 4.12 is equivalent to the right side of Equation 4.6. The second term is the torque density due to magnetocrystalline anisotropy energy. The terms both contain a constant multiplied by a function of γ and ϵ. For an external field of 75 mT and saturation magnetization 0.6 T, the constant in the Zeeman term has a value of 36 kNm/m^3 and the magnetocrystalline term has a value of 1.3 kNm/m^3. The Zeeman term is more than an order of magnitude larger than the contribution of the magnetocrystalline anisotropy energy.

The functions of strain and angle in each term have different characteristics. The angle γ at which the Zeeman torque is zero and the energy is minimized changes continuously as the strain changes, going from 0° to 90° as the normalized strain goes from 0 to 1. The zero of the magnetocrystalline torque corresponding to the energy minimum is only either 0° or 90°. If $\epsilon < 0.5$ the equilibrium angle is 0° and if $\epsilon > 0.5$ the equilibrium angle is 0°. If the strain $\epsilon = 0.5$ the magnetocrystalline torque is zero for all angles of γ. The torque contribution of the magnetocrystalline anisotropy energy does not have the same symmetry as the Zeeman energy, but is small and does not significantly contribute to the torque at the low fields in the experiments. The equilibrium angle is almost identical to Equation 4.7 and cannot be distinguished in Figure 3 from the solution which neglects the magnetocrystalline anisotropy energy (*i.e.* Equation 4.7). These two energies do not predict accurately the equilibrium angle for intermediate strain values.

4.5.3 Internal Field

The equations in Section 4.4.1 for the Zeeman energy assume that the magnetic field inside the material is the same as the external magnetic field. In fact, a magnetized body creates its own demagnetizing internal magnetic field in addition to the external

field. The demagnetizing field (internal field) is a function of the specimen geometry and the orientation in the external field.

The effective magnetic field in the body is

$$H_{\text{eff}} = H - N_d M \tag{13}$$

where N_d is the geometric demagnetization factor and M the average magnetization of the sample. The sum of the Zeeman and internal field energies is

$$E_{\text{net}} = -\mu_0 \left(H - \frac{1}{2} N_d M\right) \cdot M \tag{4.14}$$

The summation of the interaction between magnetic moments counts each interaction twice; thus, a factor of ½ is included in the internal field energy term. The energy E_{net} refers to the total magnetic field energy. In a non-spherical sample such as a bar, N_d is different for each direction.

The shape anisotropy and internal field significantly affect the torque in the Ni-Mn-Ga specimen. Figure 4.5 shows that the torque required to rotate the specimen decreases with increasing strain. As the strain increases, the domain with easy axis of magnetization parallel to the short dimension of the sample increases. The geometry of the domain with easy axis parallel to the long dimension changes such that the demagnetization factor in the easy axis increases as well. At 6% strain, the internal field is large due to large demagnetization factor, while at 0% strain the demagnetization factor and internal field are small. The maximum torque decreased by a factor of 5.87 between 0% and 6% strain, while the relative demagnetization factor decreased by a factor of 4.15 [15].

Ni-Mn-Ga has uniaxial anisotropy along the crystallographic *c* direction, which causes the magnetization vectors to align in that direction. We know the direction of

magnetization, however, for a twinned specimen (Figure 4.7) the *c* direction varies throughout the sample and the domain pattern changes with varying strain. The geometry of each domain changes with strain. The demagnetizing field is a function of the magnetization as well as the demagnetization factor; this means that N_d must be calculated for each twin domain at each strain value. Additionally, the susceptibility along the easy axis is very high and the magnetization saturates at a low field (~15 mT).

Let us assume a single domain with easy axis of magnetization parallel to *x* (Figure 4.6) that saturates at an effective field of 15 mT. We represent the average magnetization as a function of the effective field with a piecewise function (Equation 4.15) instead of a linear one.

$$M_{av} = \begin{cases} \chi H_{\text{eff}} & 0 \le H_{\text{eff}} < 15\ mT \\ M_{\text{s}} & H_{\text{eff}} \ge 15\ mT \end{cases} \tag{4.15}$$

The internal field energy does not significantly contribute to α at low external fields. We analyze the external and internal field energies separately. The energies in Equations 4.10 can be combined with the internal energy calculated from Equations 4.14 and 4.15 to find the total energies of domains A and B:

$$E_{\text{TA}} = -\mu_0 M_{\text{s}} H \cos\gamma + \frac{1}{4K_u}(\mu_0 M_{\text{s}} H)^2 \sin^2\gamma + \frac{1}{2} H_d^x M_{\text{av}} \tag{4.16A}$$

$$E_{\text{TB}} = -\mu_0 M_{\text{s}} H \sin\gamma + \frac{1}{4K_u}(\mu_0 M_{\text{s}} H)^2 \cos^2\gamma + \frac{1}{2} H_d^y M_{\text{av}} \tag{4.16B}$$

where H_{d}^{x} and H_{d}^{y} are the demagnetizing fields for the A domain in the *x* direction and the B domain in the *y* direction, respectively. The internal field energy in Equation 4.16 is not a continuous function of γ if the magnetization saturates. The torque due to the internal field must be calculated for specific values of strain, γ, and *H*. Some values for the magnetotorque are given in Table 4.1 and discussed in Section 4.4.4.

Table 4.1 Torque contributions from the Zeeman energy, magnetocrystalline anisotropy energy, and shape anisotropy energy, as well as the measured torque. For relative strains of $\epsilon = 0$, 0.5 and 1 the symbolic equation for each contribution is given along with the calculated maximum value, angle of maximum torque, and angle for which the torque vanishes. The angle refers to γ, which is the angle between the long axis of the sample and the magnetic field. The calculated values are given for an external field H_a = 75 mT, saturation magnetization M_s = 0.6 T, and magnetocrystalline anisotropy energy of K_u = 2.45 x 10^5 J/m^3. The torque values given are normalized by the volume, and have the units kNm/m^3 = kPa.

ϵ	Zeeman energy (kNm/m^3)			Magnetocrystalline anisotropy energy (kNm/m^3)			Shape anisotropy energy (kNm/m^3)			Experimental (kNm/m^3)		
0	$-\mu_0 M_s H_a \sin\gamma$			$\frac{-1}{4K_u}(\mu_0 M_s H_a)^2 \sin 2\gamma$			$\frac{1}{2} H_d^x M_s$			-80	57°	4°
	-36	90°	0°	-1.3	45°	0°	11	90°	0°			
0.5	$\frac{1}{2}\mu_0 M_s H_a(\cos\gamma - \sin\gamma)$			0			$\frac{1}{4} M_s(H_d^x + H_d^y)$			-23	67°	22°
	±18	0°, 90°	45°	0	none	All angles	±8	90°, 0°	45°			
1	$\mu_0 M_s H_a \cos\gamma$			$\frac{1}{4K_u}(\mu_0 M_s H_a)^2 \sin 2\gamma$			$\frac{1}{2} H_d^y M_s$			-13	133°	89°
	36	0°	90°	1.3	45°	90°	-17	0°	90°			

4.5.4 Comparison of different energy contributions to magnetic torque

Table 4.1 contains the torque contributions from the Zeeman energy, magnetocrystalline anisotropy energy, and shape anisotropy energy, as well as the measured torque in a Ni-Mn-Ga specimen. For relative strains of $\epsilon = 0$, 0.5 and 1 the symbolic equation for each contribution is given along with the calculated maximum

value, angle of maximum torque, and angle for which the torque vanishes. The angle refers to γ, which is the angle between the long axis of the sample and the magnetic field. The calculated values are given for an external field H = 75 mT, saturation magnetization M_s = 0.6 T, and magnetocrystalline anisotropy energy of K_u = 2.45 x 10^5 J/m^3. The torque values given are normalized by the volume, and have the units kNm/m^3 = kPa.

The Zeeman energy from the external field contributes the most to the torque. At low fields such as the ones used in this experiment, the magnetocrystalline anisotropy energy is negligible. The magnitude of the shape anisotropy energy is much greater in the case for ε = 1 because domain A has its easy axis parallel to the direction with the largest demagnetization factor. Figure 5 shows that with increasing fraction of domain B, the torque required to rotate the specimen decreases. This is due to the larger demagnetizing field in the direction of easy magnetization in domain B.

The sum of the magnitudes of the calculated torques does not match the measured torque. The case for ε = 0 has a measured torque larger than the combined magnitudes of the torque calculated. The sum of the calculated torques in the case where ε = 1 results in a torque of the opposite sign of the measured torque.

The analysis used to calculate torque internal field energy is insufficient to use for a twinned sample of Ni-Mn-Ga because (i) Equation 4.14 assumes a homogeneous magnetization and (ii) the domains are not rectangular. Twin domains magnetize differently due to the difference in easy axis of magnetization. Additionally, material interfaces including twin boundaries, affect the magnetization. Also, no published values of demagnetization factor for the shape of the domains exist. We can apply demagnetization factors to single-domain states, at 0% and 6% strain, but not at

intermediate strains. Finally, we cannot assume that neighboring domains do not influence each other [10]. Thus, a quantitative analysis of the torque of twinned specimen requires numerical, micromagnetic calculations which are beyond the scope of this study.

The sample had two twin boundaries and three domains (Figure 4.2b). The twin structure in the sample was B-A-B (using the domain nomenclature in Figure 4.6). The center domain (domain A) has c // x while the two outside domains have c // y. We also tested the sample with an opposite twin structure, A-B-A. At an equal magnetic field of 75 mT and equal strain value of 2%, the B-A-B structure required 1.7 times more torque to rotate than the A-B-A structure. The only difference was the geometry of each domain, which resulted in different internal field magnitudes in the domains.

The demagnetization factor does not provide sufficient information to describe the internal field in the sample. The above analysis assumes saturation of the magnetization and independent stray fields in each domain. Also, a sample with the same number of domains and overall strain can experience very different torques, even with relatively simple domain structures containing only two twin boundaries. We cannot account for the internal field with an experimentally derived parameter using these values. The evaluation of the internal field requires a micromagnetic analysis of specific twin microstructures which is beyond the scope of this study.

4.6 Conclusion

The magnetocrystalline anisotropy energy caused the magnetic moments to remain parallel to the axis of easy magnetization; the direction of magnetic moments was invariant. The Zeeman energy was a function of the angle between the sample and field, resulting in torque on the sample. While the change in Zeeman energy contributed the

most to the torque, the internal field energy drastically reduced the torque at large strain values. The change in maximum torque in Figure 4.5 as well as the deviation of equilibrium angle from that calculated in Equation 4.7 are due to the difference in internal field energy due to shape anisotropy.

As the strain in the sample increased, the geometries of each domain changed such that the demagnetization factor in the direction of the easy axis increased. The increase in internal field effectively decreased the magnitude of the external field, which resulted in smaller total energy and less torque. When the magnetocrystalline and shape anisotropies worked synergistically (the easy axis was parallel to the long domain dimension) the sample experienced a large torque. When the magnetocrystalline and shape anisotropies worked antagonistically (the easy axis was parallel to the short sample dimension) the sample experienced smaller torque.

Not only the sample geometry but the twin domain microstructure changes the contribution of the internal field to the magnetization and energetics of the sample. This in turn affects the magneto-mechanical properties. Sample geometry and twin domain structure can be manipulated in order to optimize the desired response of an MSMA sample.

4.7 Acknowledgements

The authors thank Justina Freilich, Tammy Jackson, Kevin Finn, Andrew Armstrong, Eric Frank, Laurel Johnston, Carl Rustad, and Paul Lindquist for assistance with experimental setup, data collection and data analysis. We thank NanoSteel for donation of equipment and the Micron School of Materials Science and Engineering for financial support.

4.8 References

1. Heczko, O.: Magnetic shape memory effect and highly mobile twin boundaries. Mater. Sci. Tech. Ser. 30(13A), 1559-1578 (2014)
2. Chernenko, V.A., L'Vov, V.A., Müllner, P., Kostorz, G., Takagi, T.: Magnetic-field-induced superelasticity of ferromagnetic thermoelastic martensites: Experiment and modeling. Phys. Rev. B. 69(13), 134410, (2004)
3. Schiepp, T. Detkov, V., Maier, M., Pagounis, E., Laufenberg, M.: Failure mechanisms and high-cycle fatigue of MSM actuators. ICFSMA, P. Müllner, W.B. Knowlton Eds., 48-49 (2013)
4. Zheng, P., Kucza, N.J., Patrick, C.L., Müllner, P., Dunand, D.C.: Mechanical and magnetic behavior of oligocrystalline Ni-Mn-Ga microwires. J. Alloy. Compd. 624, 226-233 (2015)
5. Kucza, N.J., Patrick, C.L., Dunand, D.C., Müllner, P.: Magnetic-field-induced bending and straining of Ni-Mn-Ga single crystal beams with high aspect ratios. Acta Mater. 95, 284-290 (2015)
6. Liang, Y.C., Kato, H., Taya, M., Mori, T.: Straining of NiMnGa by stress and magnetic fields, Scr. Mater. 45(5), 569-574 (2001)
7. O'Handley, R.C.: Model for strain and magnetization in magnetic shape-memory alloys. J. Appl. Phys. 83(6), 3263-3270 (1998)
8. L'Vov, V.A., Gomonaj, E.V., Chernenko, V.A.: A phenomenological model of ferromagnetic martensite. J. Phys.-Condens. Mat. 10(21), 4587-4596 (1998)
9. James, R.D., Wuttig, M.: Magnetostriction of martensite. Philos. Mag. A. 77(5), 1273-1299 (1998)
10. Heczko, O., Vokoun, D., Kopecky, V., Beleggia, M.: Effect of Magnetostatic Interactions on Twin Boundary Motion in Ni-Mn-Ga Magnetic Shape Memory Alloy. IEEE Magn. Lett. 6, 1000204, (2015)
11. O'Handley, R.C., Paul, D.I., Allen, S.M., Richard, M., Feuchtwanger, J., Peterson, B., Techapiesancharoenkij, R., Barandiaran, M., Lazpita, P.: Model for

temperature dependence of field-induced strain in ferromagnetic shape memory alloys. Mat. Sci. Eng. A-Struct. 438, 445-449 (2006)

12. Kellis, D., Smith, A., Ullakko, K., Müllner, P.: Oriented single crystals of Ni-Mn-Ga with very low switching field. J. Cryst. Growth. 359, 64-68 (2012)

13. Chmielus, M., Rolfs, K., Wimpory, R., Reimers, W., Müllner, P., Schneider, R.: Effects of surface roughness and training on the twinning stress of Ni-Mn-Ga single crystals. Acta Mater. 58(11), 3952-3962 (2010)

14. Straka, L., Heczko, O., Hanninen, H.: Activation of magnetic shape memory effect in Ni-Mn-Ga alloys by mechanical and magnetic treatment. Acta Mater. 56(19), 5492-5499 (2008)

15. Aharoni, A.: Demagnetizing factors for rectangular ferromagnetic prisms. J. Appl. Phys. 83(6), 3432-3434 (1998)

16. Tickle, R., James, R.D.: Magnetic and magnetomechanical properties of Ni2MnGa. J. Magn. Magn. Mater. 195(3), 627-638 (1999)

17. Müllner, P., Chernenko, V., Wollgarten, M., Kostorz, G.: Large cyclic deformation of a Ni-Mn-Ga shape memory alloy induced by magnetic fields. J. Appl. Phys. 92(11), 6708-6713 (2002)

4.9 Supplemental Materials

A soft magnetic iron (VWR Scientific, composition Fe-98.8±0.1%, Mn-0.7±0.1% and Si-0.3±0.1% as measured with EDS) was machined into a bar with dimensions 19.98 x 3.50 x 1.79 mm^3. The soft magnetic iron had a magnetic susceptibility of 15 as measured with a vibrating sample magnetometer (VSM, DMS Model 10). An Alnico 8 permanent bar magnet (Grainger) was also subjected to torque measurements.

Figure S1 shows the torque as a function of the angle γ for the Alnico 8 permanent magnet (Figure 4.8a) and the soft magnetic iron (Figure 4.8b). The permanent

magnet came to an equilibrium angle (i.e. at zero torque) within a few degrees near 0°, i.e. when the longest dimension of the sample was parallel to the magnetic field. The permanent magnet rotated by 80° to 110° in γ before spinning to a new equilibrium angle. The magnitude of the maximum torque increased nearly linearly with the magnitude of the external field. The torque increased linearly with the angle until close to 70° before leveling off.

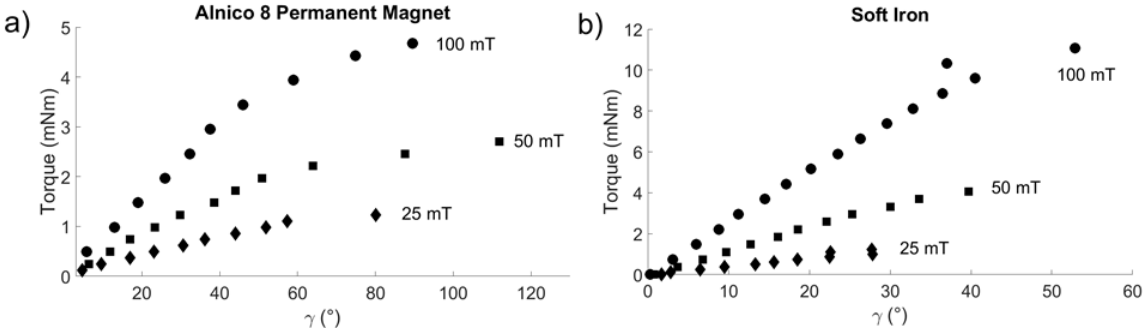

Figure 4.8 Torque in a field of 25, 50, and 100 mT as a function of angle γ between the magnetic field and the direction of the long axis of the sample for (a) the Alnico 8 permanent magnet and (b) the soft magnetic iron. The permanent magnet (a) rotated by much more than the soft iron (b) because the permanent magnet had only one equilibrium angle at γ = 0° while the soft iron had two equilibrium angles at γ = 0° and 180°. The main torque contributor in the permanent magnet is the Zeeman energy, while in the soft iron it is the shape anisotropy energy.

The soft iron came to an equilibrium angle within a few degrees of 0° as well. The torque increased nearly linearly to around 30° to 50°, without leveling off before spinning to a new equilibrium position. The magnitude of the torque increased with the external field with a power dependence between a linear and quadratic relation (Section 4.4.4).

In the case of the permanent magnet, the magnet aligned with the field so the moments were parallel to the field. At 180° to the equilibrium position, the moments were aligned anti-parallel to the field, which is the angle of maximum energy and an unstable equilibrium. The permanent magnet had only one stable equilibrium position

determined by the Zeeman energy, the energy of a magnetized body in an external field. The soft magnetic material aligned such that the demagnetizing (internal) field was minimized. The magnetic moments aligned parallel to the field at any orientation. The soft iron had two stable equilibrium angles separated by 180°, where the magnetic field was parallel to the direction of smallest demagnetization factor (Section 4.4.3).

The samples spun to the nearest equilibrium angle in the direction of the applied torque once the loading system became unstable. The equilibrium angles of the permanent magnet were separated by 360° as opposed to the soft iron which had equilibria separated by 180°. The permanent magnet rotated by approximately twice the angle γ before the loading system became unstable.

In the case of the Alnico 8 permanent magnet (Figure 4.8a) the magnetization direction is along the sample's long axis (parallel to *x*) and α = 0°. Equation 4.3 then reduces to

$$E_Z = -\mu_0 MH \cos\gamma \tag{4.17}$$

The negative cosine function contains one minimum at 0°, giving one equilibrium angle between the permanent magnet and the magnetic field. In this case, the torque increases proportional to sin γ and to the magnetic field as found experimentally (Fig. 4.8a).

In a soft, magnetically isotropic material, such as the soft iron bar, the magnetization changes direction depending on the magnetic field direction. The magnetic hysteresis of a soft magnetic material is very small and, thus, the magnetization direction is nearly parallel to the magnetic field. In this case $\gamma = \alpha$ and the Zeeman energy is

$$E_Z = -\mu_0 MH. \tag{4.18}$$

At low fields (i.e. substantially below the saturation field) and for soft magnetic materials, the magnetization is linearly proportional to the external magnetic field: $M = \chi H$ where χ is the magnetic susceptibility. For a soft, isotropic magnetic material χ does not depend on direction ($\chi_x = \chi_y$). Substituting the linear relationship between M and H in Equation 4.18 for the Zeeman energy gives

$$E_Z = -\mu_0 \chi H^2. \tag{4.19}$$

In the case for a soft isotropic material the Zeeman energy does not depend on orientation. Therefore, the Zeeman energy does not impose a torque. The torque measured for soft iron (Figure 4.8b) originates from the shape anisotropy (Section 4.4.3).

We decompose the components of the external field and magnetization into the x and y components. The components of the external field are

$$H_x = H \cos\gamma \tag{4.20A}$$

$$H_y = H \sin\gamma \tag{4.20B}$$

The magnetization M in Equation 4.18 is the effective magnetization; using $M = \chi H_{eff}$ (i.e. substantially below saturation), the effective magnetic field is:

$$H_{\text{eff}} = {H}/{(1 + N_d \chi)} \tag{4.21}$$

The x and y components of the magnetization are

$$M_x = {\chi H_x}/{1 + N_d^x \chi} \tag{4.22A}$$

$$M_y = {\chi H_y}/{1 + N_d^y \chi} \tag{4.22B}$$

N_d^x and N_d^y refer to the demagnetization factors in the x and y dimensions of the sample. The dot product in Equation 4.19 becomes

$$E_{\text{net}} = -\mu_0 \left[(H_x M_x + H_y M_y) - \frac{1}{2} \left(N_d^x M_x^2 + N_d^y M_y^2 \right) \right] \tag{4.23}$$

To find the total magnetic field energy for the soft iron bar, we combine Equations 4.20, 4.21, and 4.22; we obtain the net energy due to external and internal fields

$$E_{\text{net}} = -\mu_0 \left\{ \chi H^2 \left(\frac{\cos^2\gamma}{1+N_d^x\chi} + \frac{\sin^2\gamma}{1+N_d^y\chi} \right) - \frac{1}{2}\chi^2 H^2 \left[N_d^x \left(\frac{\cos\gamma}{1+N_d^x\chi} \right)^2 + N_d^y \left(\frac{\sin\gamma}{1+N_d^y\chi} \right)^2 \right] \right\} \quad (4.24)$$

Using Equation 4.2 to find the torque due to the magnetic field energy, we find

$$\theta_{\text{net}} = \mu_0 \chi H^2 \sin 2\gamma \left[\frac{1}{1+N_d^y\chi} - \frac{1}{1+N_d^x\chi} - \frac{\chi N_d^y}{2\left(1+N_d^y\chi\right)^2} + \frac{\chi N_d^x}{2\left(1+N_d^x\chi\right)^2} \right] \quad (4.25)$$

The torque due to net magnetic field energy has zeros at $\gamma = 0°$ and 90° and a maximum at $\gamma = 45°$. The torque zeros at $\gamma = 0°$ and 90° correspond to one energy maximum and one energy minimum. If $N_d^x < N_d^y$, $\gamma = 0°$ corresponds to an energy minimum and is the equilibrium angle. This is the case for the current specimen, the longer *x* dimension results in a smaller demagnetization factor and internal field with the field parallel to that direction. The difference in demagnetization factors (shape anisotropy) is the driving force of the torque in the soft magnetic iron (if the demagnetization factors are equal, Equation 4.25 is zero). If $N_d^x > N_d^y$, $\gamma = 90°$ corresponds to an energy minimum.

The symmetry (or period) of Equation 4.25 matches the symmetry of the measured torque. Equation 4.25 has a period half that of Equation 4.4, which describes the energy in the permanent magnet. The soft iron rotates by approximately half the angle of the permanent magnet in accordance with this analysis. The magnitude of the torque described by Equation 4.25 varies with the square of the external field *H*. In order to determine the relationship between torque and external field of the experimental data, we found the slope of the relationship of $\log\theta_{\text{net}}$ vs. log *H*. The slope for the experimental

data varied from 1.4 to 1.3 as γ varied from 0° to 45°, thus, the field dependence of the torque is less than quadratic. Equation 4.25 assumes a homogeneous magnetization and neglects effects of a magnetic domain structure.

The anisotropic shape of the sample causes a different internal field depending on the orientation of the sample in the magnetic field. Shape anisotropy results in a torque on the soft iron of the same order of magnitude as the torque measured in the other samples.

CHAPTER FIVE: TWIN ENHANCED MAGNETIC TORQUE

Anthony Hobza[1]

Carlos J. García-Cervera[2]

Peter Müllner[1]

[1]Micron School of Materials Science and Engineering, Boise State University, Boise, ID 83725

[2]Department of Mathematics, University of California, Santa Barbara, CA 93106

Under review for publication by Elsevier in *Journal of Magnetism and Magnetic Materials*

5.1 Abstract

Magnetic shape memory alloys experience magnetic-field-induced torque due to magnetocrystalline anisotropy and shape anisotropy. In a homogeneous magnetic field, torque results in bending of long samples. This study investigates the torque on a single crystal of Ni-Mn-Ga magnetic shape memory alloy constrained with respect to bending in an external magnetic field. The dependence of the torque on external magnetic field magnitude, strain, and twin boundary structure was studied experimentally and with computer simulations. With increasing magnetic field, the torque increased until it reached a maximum near 700 mT. Above 200 mT, the torque was not symmetric about the equilibrium orientation for a sample with one twin boundary. The torque on two specimen with equal strain but different twin boundary structures varied systematically with the spatial arrangement of crystallographic twins. Numerical simulations show that twin boundaries suppress the formation of 180° domains if the direction of easy magnetization between two twin boundaries is parallel to a free surface and the magnetic field is perpendicular to that surface. For a particular twin microstructure, the torque decreases with increasing strain by a factor of six due to the mutual compensation of magnetocrystalline and shape anisotropy. When free rotation is suppressed such as in transducers of magneto-mechanical actuators, magnetic-field-induced torque creates strong bending forces which may cause friction and failure under cyclic loading.

5.2 Introduction

As all magnets do, magnetic shape memory alloy (MSMA) samples experience a torque when exposed to a magnetic field that is not parallel to the magnetization of the sample. Although very basic, this torque has been neglected in almost the entire literature

on the magneto-mechanics of MSMAs as exemplified in a recent review [1]. Zheng *et al.* [2] demonstrated magnetic-torque-induced bending (MTIB) of MSMA wires and Kucza *et al.* [3] discovered a shape effect according to which long samples (*i.e.* samples with a large length-to-width aspect ratio) deform in a magnetic field mostly by bending (*i.e.* MTIB) while short samples (*i.e.* samples with a small aspect ratio) deform axially by magnetic-field-induced straining (MFIS).

MFIS proceeds by deformation twinning in the low temperature martensite phase. Twin boundaries move if the stress induced by an external magnetic field exceeds a critical stress referred to as the twinning stress. Twin boundary motion reorients the anisotropic unit cell. As the twin boundary moves through the material, one twin domain grows and the other shrinks, which results in a macroscopic shape change. The driving force for twin boundary motion in an external field has been analytically described as the change in magnetic energy over a finite distance the twin boundary moves [4-6]. The authors applied micromagnetic principles in their energy calculations. In analytical methods, many times only the external field and magnetocrystalline anisotropy energies are accounted for [5,7,8]. Typically, authors assume that a twin domain is homogeneously magnetized [5,9,10], which ignores the potential for 180° domain walls to form. Other models, which include 180° magnetic domains, fix domain fractions such that the 180° magnetic domain wall maintains continuity across the twin boundary [11,12].

These models differ from experimental findings of Lai *et al.* who described that 180° domains existed in the twin domain with axis of easy magnetization perpendicular to the external field [13]. The 180° domain walls did not maintain continuity at a twin

boundary. Analytical calculations were based on a physical model of the magnetic structure in the material. The assumptions taken to create the physical model restricted the energy landscape the model can access. The validity of the physical model was not re-assessed once the energy minimization was completed. The complexity of magnetic and mechanical microstructures made it nearly impossible to create a reasonable model to describe the material. In the case of a bending sample [2,3,14], the axis of easy magnetization is not simply parallel to or perpendicular to the magnetic field. Additionally, the twin structure changes depending on the amount of bending, and twin boundaries may not be parallel.

Magnetic field induced bending in magnetic shape memory alloys was reported on a thin film and attributed to a magnetic field gradient in an inhomogeneous field [14]. The authors noted that, even in a homogeneous field, the magnetocrystalline and shape anisotropy result in a torque on the specimen. Zheng *et al.* first reported on bending in a homogeneous magnetic field [2]. The authors rotated an oligocrystalline wire in a homogeneous field; the wire not only experienced axial strain but also magnetic-torque-induced bending. The driving force for bending was attributed to magnetic torque; twin boundary motion accommodated bending. Kucza *et al.* further studied MTIB in a homogeneous field by rotating single crystal specimen with varying aspect ratio in an external magnetic field [3]. The bending strain increased with increasing aspect ratio, while the axial strain stayed consistent. The authors qualitatively described the torque magnitude in terms of the Zeeman, magneto crystalline and shape anisotropy energies. The authors discussed the influence of magnetic energies on the dependence of bending on the external magnetic field and sample geometry [3]. However, a bending specimen

presents an exceptionally difficult system to analyze quantitatively. Many twin boundaries exist, and the angle of the magnetic field with respect to the axis of easy magnetization varies across the length of the specimen.

Characterization of torque gives the ability to directly probe the energetics of a sample in a magnetic field [15]. In a previous study we investigated the torque on a Ni-Mn-Ga single crystal specimen constrained with respect to bending in an external magnetic field. The torque magnitude varied by nearly a factor of 6 depending on the strain of the specimen, *i.e.* the twin domain fraction present in the specimen. We attempted to describe the torque with the change in magnetic energy as a function of the angle between the specimen and magnetic field. The magnetic energy was described assuming homogeneous magnetization in twin domains, but the torque could not be adequately described with the external field, demagnetizing field, and anisotropy energies but requires numerical, micromagnetic calculations, which is the objective of the present study.

5.3 Micromagnetism

Micromagnetism is the numerical study of the energy contributions to the equilibrium magnetic structure of a material on a mesoscopic length scale. In other words, we seek the distribution of magnetic moments that minimizes the total energy with a resolution in the range of nanometers to micrometers. We consider the following energies. (1) The exchange energy is the product of the exchange constant C_{ex}, with the square of the gradient of the magnetization, **M**, integrated over the sample volume (V):

$$E_{\text{ex}} = C_{ex} \int_V |\nabla \mathbf{M}|^2 \, dV \tag{5.1}$$

(2) The magnetocrystalline anisotropy energy: Ni-Mn-Ga is uniaxial anisotropic with the anisotropy energy constant K_u :

$$E_{\text{anis}} = \int_V K_u \sin^2\alpha \, dV \tag{5.2}$$

(3) The external field energy is the dot product of the external field vector **H** with the magnetization vector **M**. The external field energy is often referred to as the Zeeman energy:

$$E_{\text{Z}} = -\mu_0 \int_V \mathbf{M} \cdot \mathbf{H}_{\text{ext}} \, dV \tag{5.3}$$

The constant μ_0 is the magnetic permeability of free space.

(4) The internal field energy is the energy of the magnetic moments in the field created internally by the net magnetization in a magnetized specimen. The internal field is calculated using Poisson's equation, where the effective magnetic charge density ρ is found from the Laplacian of the magnetic potential U, expressed as $\Delta U = \rho$. The internal magnetic field, analogous to the electric field created by an electric potential, is given as $\mathbf{H}_{\text{int}} = \nabla U$. The internal field energy is

$$E_{\text{int}} = \frac{\mu_0}{2} \int_V |\nabla U|^2 \, dV \tag{5.4}$$

The effective magnetic field, **H**, at a point in a specimen is given as the first derivative of the energy with respect to magnetization:

$$\mathbf{H} = -\frac{\delta E}{\delta M} = \frac{2C_{ex}}{M_S^2}|\nabla \mathbf{M}|^2 - \frac{2K_u}{M_S^2}(M_2 + M_3) + \mu_0 \mathbf{H}_{\text{ext}} - \mu_0 \nabla U \tag{5.5}$$

The effective field is the driving force for a change in magnetization which results in lower energy. Equation (5.5) assumes uniaxial magnetocrystalline anisotropy, where M_2 and M_3 are the magnetization components in Cartesian coordinates orthogonal to the axis of easy magnetization. M_s is the saturation magnetization. The relaxation process of

the magnetization distribution in a ferromagnetic material is described by the Landau-Lifshitz equation [16]

$$\frac{d\mathbf{m}}{dt} = \gamma_0 \mathbf{m} \times \mathbf{H} - \frac{\alpha\gamma_0}{M_s} \mathbf{m} \times (\mathbf{m} \times \mathbf{H}) \tag{5.6}$$

The constants α and γ_0 are the damping and gyromagnetic terms, respectively.

5.4 Experimental Procedure

Single crystal specimen of Ni-Mn-Ga were grown with a modified Bridgeman-Stockbarger technique with an apparatus described in Ref. [17]. Specimen were grown with a nominal composition of $Ni_{50.5}Mn_{27.75}Ga_{21.75}$ (atomic percent); however, due to chemical segregation during growth there was a composition gradient across the crystal resulting in sections with different martensite structures at room temperature. Crystals were characterized in a Hitachi S3400 scanning electron microscope with energy dispersive x-ray spectroscopy (EDS, Oxford Instruments Energy$^+$ detector) and a Bruker D8 X-ray diffractometer with a Cu K_α source. Samples were cut with a Princeton Scientific WS-22 wire saw with a 50 μm diameter tungsten wire and polished using successively smaller grit SiC paper and then diamond slurries down to 1 μm diameter diamonds. The Ni-Mn-Ga sample tested had 10M structure with composition $Ni_{51.1}Mn_{25.7}Ga_{23.2}$ (atomic percent, as determined with EDS with accuracy atomic percent) and measured 16.46 x 5.02 x 3.62 mm^3 fully extended in the longest dimension and compressed in the intermediate dimension. The sample was subjected to constant magnetic fields $\mu_0 H$ from 50 to 1500 mT in a Varian Associates V3603 electromagnet. Once the samples had reached an equilibrium angle with the external magnetic field, a torque was applied as described below and the angular deflection was measured.

A cylindrical sample holder made from Teflon contained a groove to accommodate the sample (Figure 5.1). The sample holder had a diameter of 25.4 mm on which the sample was laid and a shaft with a smaller diameter of 9.53 mm which was press-fit into the inner bore of two ZrO_2 non-magnetic bearings and an E-5 optical encoder kit from US Digital with 5000 counts per revolution (Figure 5.1a). The ceramic bearings were placed in machined nylon between the pole pieces of an electromagnet (Varian Associates V3603). The optical encoder was fixed to the nylon with nylon screws.

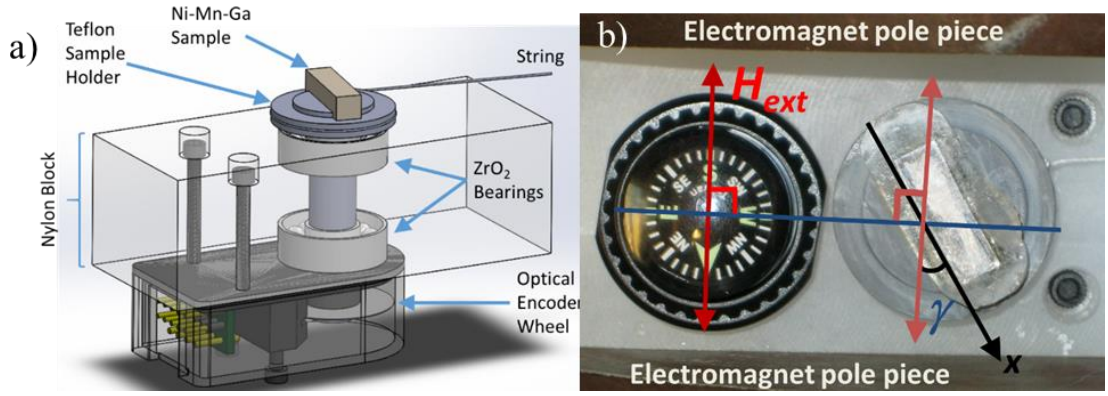

Figure 5.1 The platform of the experimental apparatus was made from a nylon block which was press fit in between the pole pieces of the electromagnet. (a) Two ceramic bearings were press fit into the nylon block. The inner diameters of the bearings guided the shaft of the Teflon sample holder into the optical encoder wheel, which was attached with a set screw. The Ni-Mn-Ga sample was laid in a groove on the sample holder. A groove was cut around the circumference of the sample holder, into which a string was tied and wrapped to apply the torque. (b) The initial angle, γ, of the sample to the external magnetic field was determined by comparing the edge of the sample to the angle of a compass deflected by the magnetic field.

The sample was placed in the sample holder and the magnetic field turned on to a set value. The sample turned to an equilibrium angle (γ_{eq}), this initial angle was measured by taking pictures using a Canon PowerShot A3000 digital camera and comparing the edge of the sample to a compass aligned in the field (Figure 5.1b) using the angle tool in

ImageJ. We defined Cartesian coordinates on the sample such that the *x* direction coincided with the long edge of the sample and the rotation axis constituted the *z* direction. The sign of the coordinates was chosen such that the trace of the twin boundary plane (when moved through the coordinate origin) bisected the first quadrant of the *x*-*y* plane (Figure 5.2). The angle γ described the deviation of the magnetic field direction from the *x* direction. When the magnetic field was parallel to the *x* direction $\gamma = 0°$. The angle γ was positive when the sample was rotated clockwise or conversely a positive γ refers to a counter clockwise rotation of the magnetic field with respect to the sample coordinate system. The angular error was less than 0.5°.

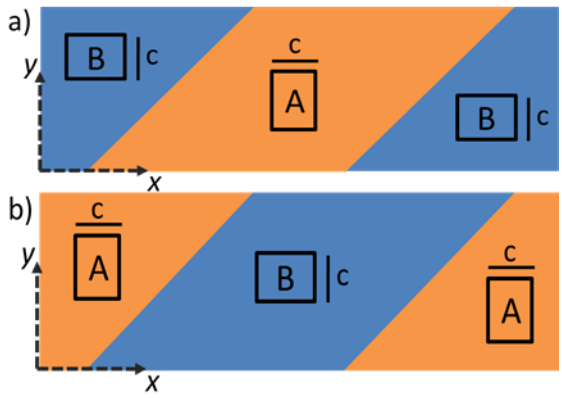

Figure 5.2 A sample containing two twin boundaries may have either microstructure, denoted by "ABA" (a) or "BAB" (b). The axis of easy magnetization is parallel and perpendicular to the lateral surface in twin domains A and B, respectively.

The sample holder had a groove cut around the circumference where a string was wrapped around and extended to a spring force gauge (PCE Instruments) and pulley. The string transferred a displacement of the pulley to apply a tangential force to the sample holder and, thus, a torque to the sample. We manually recorded angle measurements with the optical encoder at regular intervals of applied torque. The optical encoder counts were compared to the measurement at γ_{eq} to calculate the total angle.

The sample was tested with microstructures containing different numbers of twin boundaries. The sample was manipulated manually to create the twin domain structure, which was characterized with optical images. We define the fully compressed state, *i.e.* when the crystallographic *c* direction is parallel to *x* in the entire sample, as the reference state with zero strain. When fully extended, *i.e.* when the crystallographic *c* direction is parallel to *y* in the entire sample, the sample had a strain of 6%. Since the sample edge kinks by approximately 3.5° across the twin boundary, the strain could not be measured with a micrometer. The strain was found by determining the relative position of the twin boundary in the sample from a high resolution optical image in ImageJ. In the cases where the sample contained one twin boundary, the sample was placed on a glass slide and cast in a two-part polyamine epoxy. This constrained the sample, which froze twin boundaries, making it possible to test the sample at external magnetic fields greater than the switching field. Samples with two twin boundaries were tested without polyamine epoxy.

The sample was tested with one twin boundary at strains of 2.27%, 3%, and 3.92%. In the case where the sample contained two twin boundaries, two twin microstructures were tested, shown in Figure 2. One twin microstructure (Figure 5.2a) referred to as ABA had three twin domains where the central twin domain had *c* parallel to *y* and the other two domains had *c* parallel to *x*. The second microstructure, BAB, had the twin domain pattern reversed (Figure 5.2b). For this case, the sample was tested at a field of 75 mT at strain values of 2%, 3%, and 4%. Samples containing two twin boundaries had parallel faces on the ends, allowing strain measurement with a micrometer screw.

Experimental results are reported in terms of specific torque (Nm/m^3). We directly compare experimental and numerical results where the sample sizes vary.

5.5 Micromagnetic Simulation

We simulated the magnetization of the sample in the external magnetic field with code, which applies micromagnetic principles to find the equilibrium magnetic microstructure. The code solves the Landau-Lifshitz equation with the Gauss-Seidel projection method [18,19]. Detailed descriptions of the code may be found in Refs 18 and 19.

In the simulations, the spatial density of magnetic moments needed to be high enough in order to effectively capture the rotation of magnetic moments across Bloch walls between 180° magnetic domains, which are tens of nanometers wide in Ni-Mn-Ga [20]. Computation time increased significantly with increased number of magnetic moments, prohibiting the simulation of a sample with the same spatial dimensions (mm^2) as the sample used in the experiment. The parameters used in the micromagnetic simulation were as follows:

The real space dimensions of the simulated sample were 4 orders of magnitude smaller than the sample used in experiments. At 3% strain, the experimental specimen had dimensions 16.00 x 5.20 x 3.60 mm^3, and for simulations at 3% strain the specimen had dimensions 1.6 x 0.52 x 0.36 μm^3. The simulation contained 384 magnetization vectors in the *x* dimension and 192 moments in the *y* dimension, resulting in magnetic moments spaced every 4.17 nm in the *x* dimension and every 2.83 nm in the *y* dimension.

The magnetic energy constants (magnetocrystalline anisotropy energy, exchange interaction energy, and saturation magnetization) are listed in Table 5.1.

Table 5.1 Numeric values of magnetic energy constants for 10M Ni-Mn-Ga for micromagnetic simulations

Energy Term	Value	Reference
Saturation magnetization (M_s)	0.61 Tesla	[31]
Exchange interaction energy (C_{ex})	6×10^{-12} J/m	[32]
Magnetocrystalline anisotropy energy (K_u)	2.45×10^5 J/m^3	[33]

Twin boundaries were defined such that the angle of the twin boundary crossed the sample at 45° in real space, consistent with the {101) type major twin boundaries seen in 10M Ni-Mn-Ga. The magnetocrystalline anisotropy energy and effective field due to the magnetocrystalline anisotropy energy were defined according to an axis of easy magnetization in different directions for neighboring twin domains. The A domain had the axis of easy magnetization in the *x* direction, while the B domain had the axis of easy magnetization in the *y* direction. The twin boundary constituted an abrupt change in the axis of easy magnetization.

Micromagnetic simulations were conducted at a constant external magnetic field and variable angle, γ, with respect to the sample. The discrete angles at which the code ran was changed depending on the twin domain structure in order to allow the code to find the same energy minima across multiple angle sweeps. An external magnetic field of 75 mT was applied to specimen with one, two, and 5 twin boundaries. The simulations ran for a fixed real time interval of 0.2 ns, during which 20,000 iterations of the minimization scheme ran. The equilibrium microstructure of magnetic moments was

recorded along with the energy components described in Section 5.2. This allowed us to view not only how each energy component changed as a function of angle, but also how the magnetic domain structure evolved.

The initial magnetic state of the sample was defined such that the component of the magnetic vector in each spatial dimension was equal. The normalized *x*, *y*, and *z* components of the magnetic vector each had an initial magnitude of $1/\sqrt{3}$, giving a total normalized magnetic vector magnitude of 1.

The two twin microstructures (Figure 5.2) which were experimentally tested with results were tested in the numerical simulations. All simulations, with one or two twin boundaries, had the twin boundaries oriented as in Figure 5.2. Coordinates and sense of rotation were as given in Section 5.3 (Figure 5.2). For the ABA twin domain structure, the angle was swept in a loop from -γ = 0° to 80° and back to 0°. This sweep was considered one loop. When then back sweep did not show the same results as the forward sweep, a second loop was run with a narrower angle range around the angle for which the energy showed a minimum. This procedure was repeated until the back sweep coincided with the forward sweep.

5.6 Experimental Results

The torque as a function of γ was tested for two different twin microstructures when the sample contained two twin boundaries. The equilibrium angle γ_{eq} depended equally on strain for the two twin microstructures (Figure 5.3a) while the maximum torque as a function of strain varied significantly (Figure 5.3b). At 2% strain and 50 mT, the BAB microstructure required 70% greater torque to rotate the sample than the ABA microstructure. This was the strain at which the greatest difference in torque occurred

between the two microstructures. Away from 2%, the torque of the BAB and ABA microstructures were closer in magnitude. When the sample contained a single twin boundary, the equilibrium angle followed the same trend as the sample with two twin boundaries. The torque at 2% strain was larger than for the two twin boundary conditions. At larger strain, the single twin boundary condition resulted in smaller torque, close to that of the ABA microstructure.

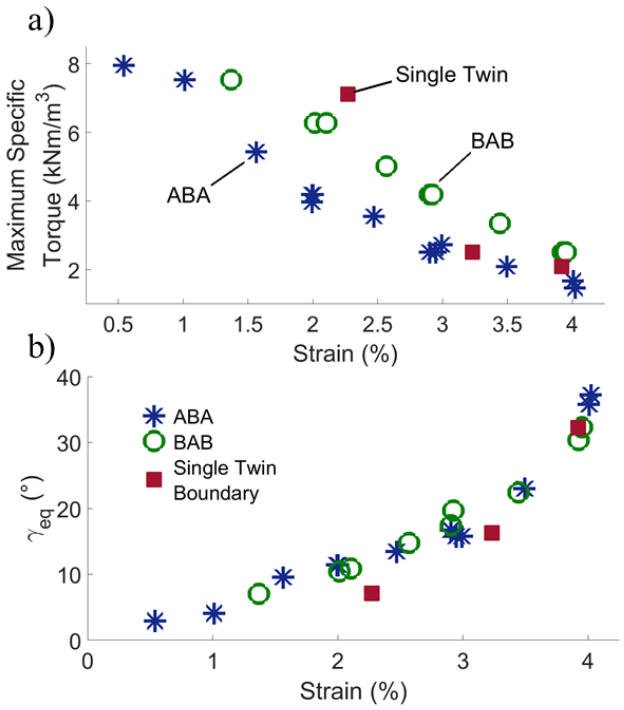

Figure 5.3 Experimental results for the maximum specific torque as a function of strain for a single twin as well as ABA and BAB twin microstructures at an external field of 50 mT (a). The equilibrium angle is shown as a function of sample strain (b). Results for the ABA and BAB microstructures are denoted with blue stars and open green circles, respectively. Results for samples with a single twin boundary are shown in solid maroon squares.

At low fields (*i.e.* <100 mT), the torque required to rotate the sample away from the equilibrium angle was symmetric about the equilibrium angle (Figure 5.4a). At larger fields, the torque required to rotate the sample in the clockwise direction did not follow a monotonic relationship. At fields larger than 250 mT, the torque first increased, reached a

local maximum, and then decreased above approximately 15° away from γ_{eq}. When the torque passed the local maximum, the sample spun to a new location further from γ_{eq} with a similar torque value. At larger angle, the torque increased progressively. Upon decreasing the torque, the angle decreased until the torque reached a local minimum value. Upon further reduction of the angle, the sample spun back closer to γ_{eq} at a similar torque value (Figure 5.4b). The hysteresis shown in Figure 4b results from the experiment being torque-controlled. The torque-angle dependence between the two experimentally accessible branches is schematically indicated with the dotted black line. Thus, the angle exhibits a bifurcation. The angle is given in terms of $\Delta\gamma$, to plot the curves for different magnetic fields into one graph. This was not possible for plotting γ because the equilibrium angle changed as a function of external magnetic field (Figure 5.5a). The dashed lines in Figure 5.5a indicate the fields for which data was plotted in Figure 5.4a.

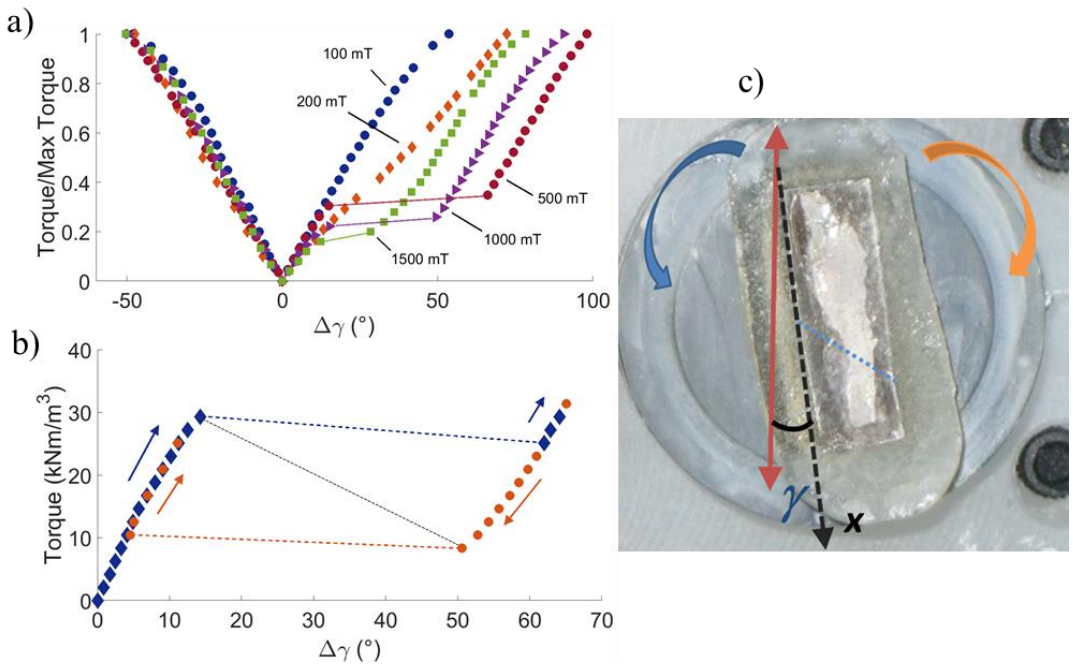

Figure 5.4 Experimental data for the normalized torque as a function of the change in γ from the equilibrium angle for a sample with one twin boundary at 2% strain (a). Data is given for 100 mT, 200 mT, 500 mT, 1000 mT, and 1500 mT in both the positive and negative g directions. Positive γ is in the clockwise direction, and negative γ is the counterclockwise direction. For magnetic fields above 200 mT, the torque decreased after ~15° rotation in the clockwise direction. The sample holder spun to a new angle, hence the abrupt jump in angle. The decrease in torque is shown in (b) for 500 mT. The jumps in angle represent show the bifurcation, since the stimulus to the sample was torque and there are multiple possible angles at the same torque. The dotted black line approximates the torque in the intermediate angle range. The sample for 2% strain is shown, containing the location of the twin boundary (dashed blue line) at the equilibrium angle at a magnetic field of 50 mT(c).

At 2% strain and magnetic fields larger than 250 mT the torque decreased with increasing magnetic field. The slope of the energy as a function of γ decreased, but never reached zero. There was no additional equilibrium angle. At 4% strain and fields greater than or equal to 250 mT, the sample experienced four equilibrium angles instead of two (which were 180 ° apart). The first equilibrium angle γ_{eq1} occurred in the same direction (negative γ) as the equilibrium angle at 2% and 3% strain. The other equilibrium angle γ_{eq2} occurred in the opposite direction (positive γ). The two unique equilibrium angles as

a function of external magnetic field are given in Figure 5.5a. Each equilibrium angle had a similar dependence on the external magnetic field; they increased sharply up to 300-400 mT where the magnitude of the equilibrium angle reached a maximum at -55 ° (γ_{eq1}) and +55 ° (γ_{eq2}). Above 55 mT, the equilibrium angles were nearly constant up to 1500 mT. Each equilibrium angle had two-fold rotation symmetry about the sample rotation axis, but the equilibrium angles did not exhibit four-fold rotational symmetry.

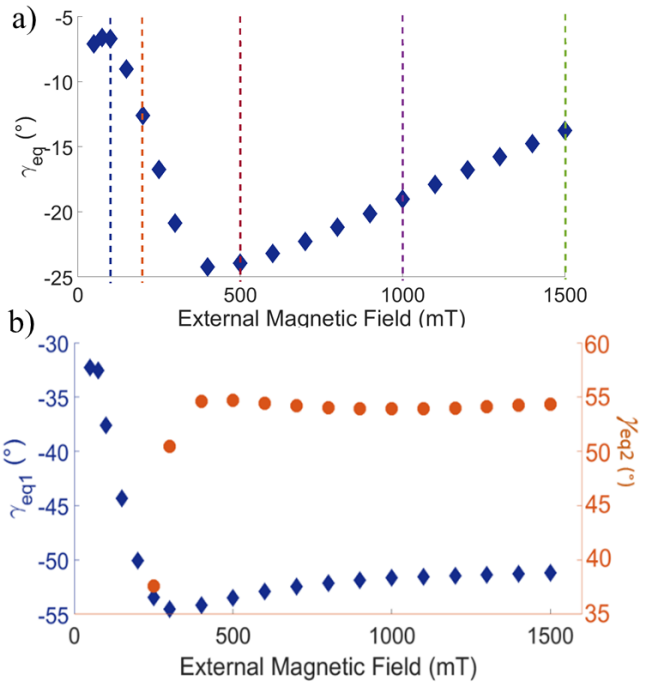

Figure 5.5 Experimental results for the equilibrium angle as a function of external magnetic field for a sample with one twin boundary at 2% strain (a) and 4% strain (b). Dashed lines indicate the equilibrium angles for the fields plotted in Figure 5.4a. At fields 250 mT and larger, two unique equilibrium angles existed for the sample at 4% strain.

5.7 Simulation Results

5.7.1 Two Twin Boundaries

Figure 5.6 shows the numerical results for the ABA twin domain structure with 3% strain. The energy as a function of γ for the converging third loop is shown in Figure

5.6a. The micromagnetic code calculated the exchange energy, magnetocrystalline anisotropy energy, stray field energy, and Zeeman energy. The variation in these individual energies (referred to their respective minimum values) are given as a function of γ in Figure 5.6b. The change in energy was plotted in order to view each energy on the same scale. The sum of anisotropy energy, exchange energy, and stray field energy is almost constant. The largest change in energy contribution came from the Zeeman energy. The change in Zeeman energy (blue solid circles in Figure 5.6b) very closely matched the total energy variation (Figure 5.6a).

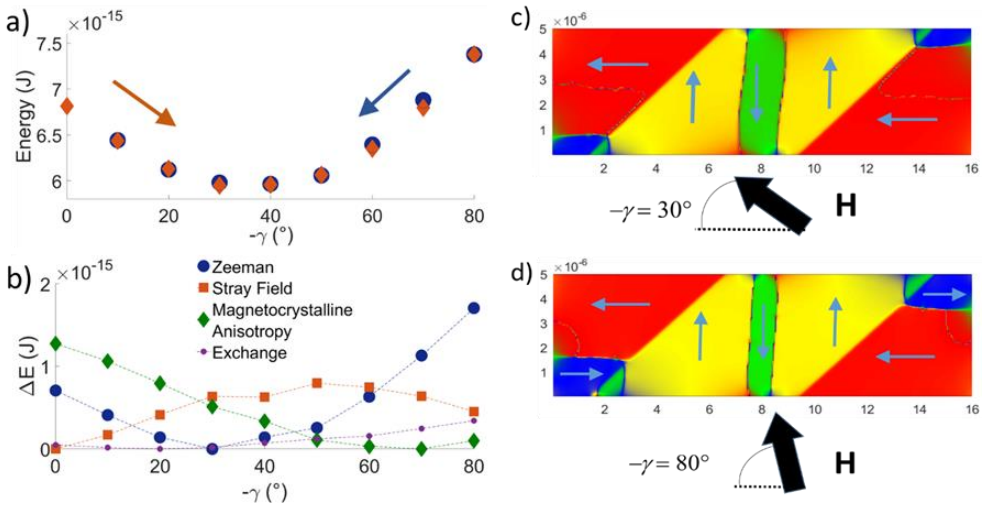

Figure 5.6 Simulation results for the magnetic energy as a function of angle is given for the ABA twin structure at a strain of 3%. The total energy is given as a function of -γ (a) and separated in its contributions in (b) as a difference to its respective minimum value. The equilibrium magnetic domain structure is shown for -γ = 30 ° (c) and -γ = 80 ° (d).

The smallest and largest total energy occurred at γ = -30° and γ = -80°. The magnetic domain structure for these two field directions are shown in Figures 5.6c and 5.6d. The gray arrows indicate the average direction of magnetic moments in each domain. As -γ increased, the blue magnetic domains grew domains grew to decrease the stray field energy in the A twin domains. As the blue domains grew, so did the green

domain adjacent to it in the *B* twin domain, which increased the Zeeman energy. The central green domain shrank as γ approached 90°.

The total area of the blue and green domains as a function of γ is given in Figure 5.7a. As the area of the domains decreased, the stray field energy increased (Figure 5.6b). The stray field energy and area of demagnetizing magnetic domains were directly related. The magnitude of the net magnetization is given in Figure 5.7b. The net magnetization was correlated inversely to the Zeeman energy in Figure 5.6b. As the net magnetization increased, the Zeeman energy decreased.

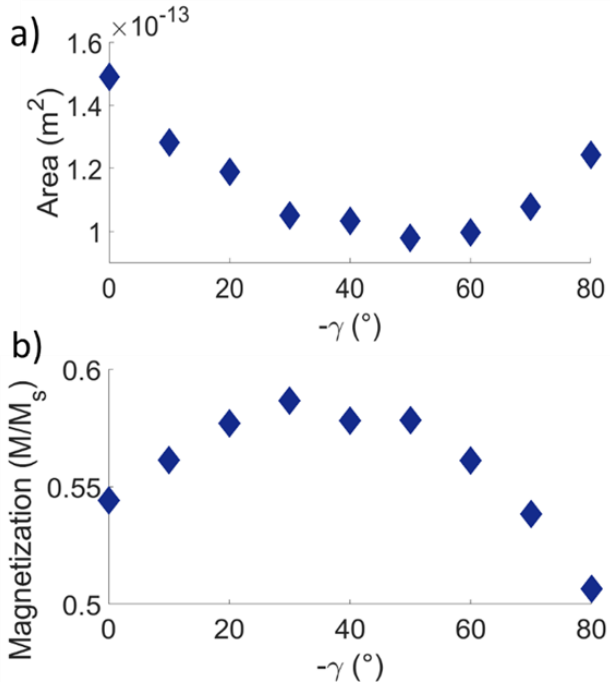

Figure 5.7 Simulation results for the ABA twin microstructure giving the total area of the blue and green magnetic domains (a) and the net magnetization (b) plotted against -γ.

Figure 5.8a gives the change in energy as a function of γ for the ABA and BAB microstructures. Again, the energies are plotted as differences to their respected minima to more easily compare the different energy contributions. The BAB microstructure

resulted in a smaller total energy. The energy increased more quickly away from the minimum energy for the BAB microstructure. The simulation shows a larger torque for the BAB microstructure than for the ABA microstructure, as seen also in experiments. A quadratic function was fit to the energy values as a function of γ. The second derivative gives the slope of the torque as a function of γ, and is constant. This is similar to experimental data, which shows a constant slope of the torque near the equilibrium angle (Figure 5.4a). Experimental and simulation results for the slope of the torque for ABA, BAB and single twin microstructures are given in Table 5.2 for 75 mT and 3% strain. While the values are about a factor of 50 different between the experimental and simulated results, both show the same dependence of the torque on the twin microstructure. The difference in absolute values stems from the much smaller volume covered with the simulation.

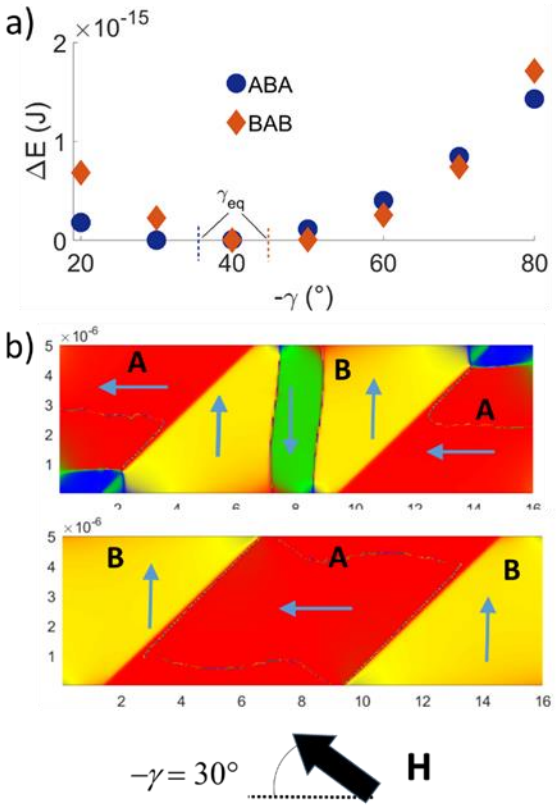

Figure 5.8 Simulated results for the change in total energy with respect to the minimum energy is given as a function of -γ for the ABA and BAB microstructures (a) along with the equilibrium magnetic domain structure at an angle of $-\gamma$ = 30° (b). The ABA microstructure (top) has 180° magnetic domains in both twin domains, while the BAB microstructure (bottom) has fully saturated domains. The simulated samples are both at 3% strain with an external magnetic field of 75 mT.

The equilibrium magnetic structures for the ABA and BAB twin microstructures at 75 mT and γ = -30° are given in Figures 5.6c and 5.8b. The ABA microstructures contained 180° magnetic domain walls in both A and B twin domains, while the twin domains in the BAB microstructure were fully saturated. The BAB microstructure had a smaller total energy (5 kJ/m^3 compared to 20 kJ/m^3 for ABA), and the energy increased more quickly with changes in γ. Thus, the BAB microstructure required a larger torque to rotate.

Table 5.2 Derivative of the specific torque as a function of γ near the equilibrium angle. The experimental results showed nearly linear (constant slope) increase in torque close to the equilibrium angle. A quadratic function was fit to the simulated energy. The second derivative of the quadratic function is a constant which gives the rate of change of the torque with increasing γ.

Twin boundary structure (3% strain, 75 mT)	Derivative of specific torque: Simulation ($Nm/m^3/°$)	Derivative of specific torque: Experimental Results ($Nm/m^3/°$)
One twin boundary	4.00	218
Two twin boundaries – ABA	4.86	235
Two twin boundaries – BAB	8.79	300

5.7.2 Single Twin Boundary

The magnitude of the total energy (Figure 5.9a) and calculated torque were both close to and less than the energy and torque of the ABA microstructure at 3% strain and 75 mT external field. The magnetization of domain A, with axis of easy magnetization parallel to the long dimension of the sample, was normal to a small surface area. The magnetization in this domain created a small stray field and saturated at low fields (Figure 5.9b). The magnetization of the B domain was normal to a larger surface area. This domain did not saturate due to the larger stray field. Magnetic domains were present in domain B. The B domain magnetized such that there was no magnetization divergence at the twin boundary; no magnetic domains intersected the twin boundary since domain A was saturated.

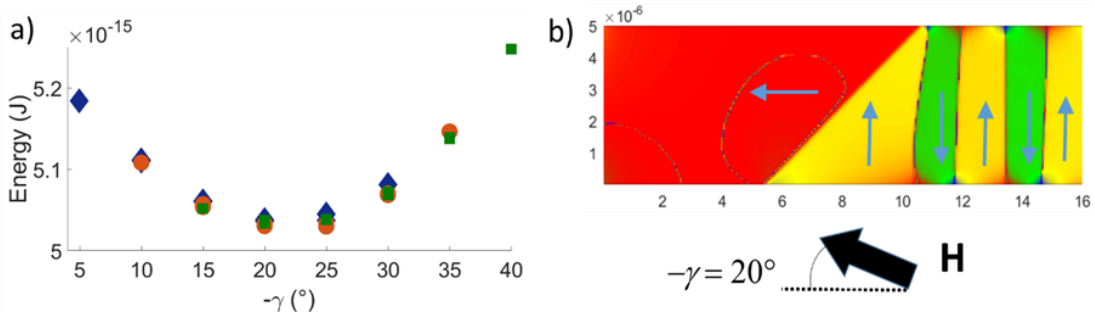

Figure 5.9 The total energy is given as a function of -γ (a) along with the equilibrium magnetic structure at the lowest energy for a sample at 3% strain and 75 mT with one twin boundary (a). The magnetic domain structure at -γ = 20° (b) shows a fully saturated A twin domain while the B twin domain has two demagnetizing 180° magnetic domains which extend from lateral surface to lateral surface without intersecting the twin boundary. To avoid intersecting the twin boundary, the outermost left 180° magnetic domain curves to the right.

At large fields, the torque was asymmetric about the equilibrium angle (Figure 5.4a). We calculated the energy for γ ranging from -90° to +90° (Figure 5.10a) for a sample at 2% strain with one twin boundary in an external magnetic field of 500 mT. The results of the simulation showed a decrease in the torque in the positive γ direction, as seen also in the experiment. The simulated data showed another energy minimum, which was not seen in experiments at 2% strain. The simulated results overestimate the decrease in energy in the positive γ direction.

The change in magnetization perpendicular to the twin boundary was nearly symmetric about γ = 0° (Figure 5.10b). The magnitude of the change in each direction was similar, but larger when the external magnetic field was perpendicular to the twin boundary (γ = -45°) than parallel to the twin boundary (γ = +45°). In contrast, the divergence of the magnetization was not symmetric about γ = 0°. The divergence, which causes the stray field, was maximum when the field was parallel to the twin boundary, and had a local minimum when nearly perpendicular to the twin boundary.

The change in each energy term as a function of γ is given in Figure 5.10d. The total stray field energy was comparable in both directions, though slightly larger in the positive γ direction. The Zeeman energy was comparable, though slightly less in the positive γ direction. The magnetocrystalline anisotropy energy has two parabolas, with the parabola in the positive γ direction having a higher minimum energy. The minimum magnetocrystalline anisotropy energy occurs near the simulated equilibrium angle.

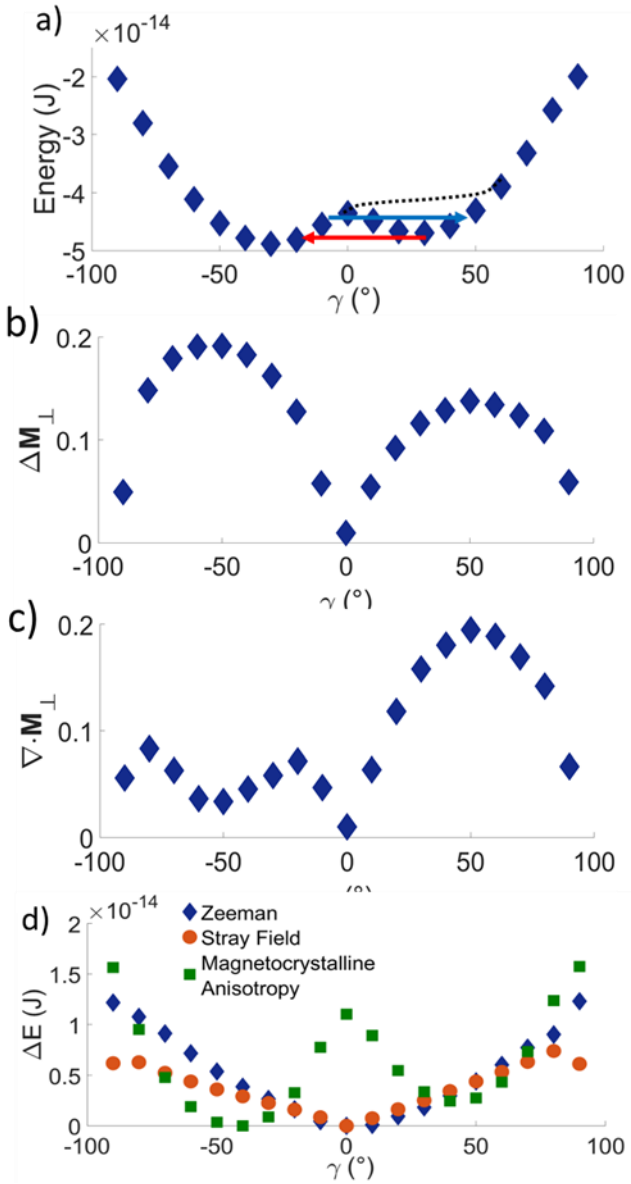

Figure 5.10 Simulated results for the energy as a function of γ at 2% strain and 500 mT for a sample with one twin boundary (a). The arrows mark the bifurcation of the stable position under torque as displayed in Figrue 4b. The change in magnetization normal to the twin boundary (b) and the divergence of the magnetization normal to the twin boundary (c) are given as a function of γ. The change in energy from the minimum for each individual energy component is given as a function of γ (d).

5.8 Discussion

The main experimental and numerical results are: (1) The magnetic torque on a Ni-Mn-Ga single crystal with equal fractions of A and B twin domains varies strongly

with the twin microstructure; for example, a single crystal with a BAB microstructure experiences a much higher torque compared to a single crystal with an ABA microstructure. (2) The magnetic torque is asymmetric with respect to the direction of rotation; for example, a crystal with a single twin boundary experiences a monotonically increasing torque when turned in one direction and a bifurcated torque when turned in the other direction. We argue here that both effects have the same origin, namely the emergence of finite divergence of the magnetization at twin boundaries.

The three dimensional, macroscopic sample measured 16.46 x 5.02 x 3.62 mm^3. The simulated specimen measured 1.6 x 0.52 x 0.36 μm^3. The simulated magnetization was found over a two dimensional matrix of magnetization vectors. The difference in sample size and dimensionality of the simulation resulted in a calculated torque, which was a factor of 50 less than the experimentally measured torque. Nevertheless, as discussed below, we believe the simulation gives valuable qualitative insight into the magnetization of the three dimensional sample used in experiments.

While the matrix of magnetization vectors was two dimensional, the magnetization vectors were free to rotate in all three dimensions. They had *x, y* and *z* components, *i.e.* the magnetization vectors were unconstrained from rotating perpendicular to the plane of the simulated specimen if a driving force existed. The external magnetic field only occurred in the *x-y* plane, which also contained the direction of easy magnetization. The driving force due to the Zeeman and magnetocrystalline anisotropy energies would cause the specimen to magnetize only in the *x-y* plane. The integral to compute the stray field energy is carried out in all three spatial dimensions. The stray field could, potentially, provide a driving force for magnetization perpendicular

to the plane. With only one vector in the *z* dimension, the exchange energy is not calculated based on any nearest neighbor in the *z* direction. The simulation assumes the exchange energy is minimized in the *z* direction. Further, the initial orientation of the magnetization vector prior to the first iteration step was [111], i.e. it had a finite *z* component. In the equilibrium magnetic structure, the *z* component had disappeared. Thus, the magnetocrystalline anisotropy suffices to force the magnetization vectors parallel to the *x*-*y* plane.

The difference between the simulation and experiment derive from the scale of sample and the assumption that the magnetization vector is invariant in the *z* sample dimension. The assumption of the simulation with only one magnetization vector in the *z* direction is that vector represents the magnetization throughout the thickness in *z*. Saturation of the A twin domains indicate that the assumption that the magnetization is homogeneous in *z* is valid for these twin domains. For B twin domains with 180° magnetic domains, the simulation assumes that magnetic domain walls extend straight through the sample. In fact, experiments show that magnetic domains form a maze-like structure when viewed parallel to the direction of easy magnetization [21-25]. Confining the magnetic domain walls in the *z* sample dimension inhibits the relaxation of stray field energy minimization through the formation of 180° magnetic domains perpendicular to the *z* axis.

The simulation did find equilibrium magnetic domain sizes comparable to reported values. The magnetic domain size depends on the sample dimensions [16]. The magnetic domains in the simulation were on the order of 100 nm in width. This is much smaller than in bulk samples, with magnetic domain width typically on the order of 100

μm [21,22,25]. In smaller specimen, such as those used for investigation in transmission electron microscopes, the magnetic domain widths are closer to 100 nm seen in the simulation [24]. For thin films, Chernenko *et al.* [26] found that the domain size is proportional to the film thickness. Thus, the domain size of this study is reasonable compared with results reported in the literature. Also, the 180° magnetic domain walls of this study are approximately four magnetic vectors wide in the *x* direction, corresponding to a width of 16.6 nm. This compares well to the analytical value of 15.5 nm calculated from Ref. [16]. The simulation finds sizes of magnetic domains and magnetic domain wall width which correspond well with experiments and the analytical solution, respectively.

The small simulated sample dimensions cause discrepancy between simulated and experimental torque. Small closure domains form at the intersection of magnetic domain walls and the crystal surface (Figure 5.6cd, 5.9b). In a small sample, these closure domains represent a much larger fraction of the sample volume than in the larger experimental sample. Also, the sample in experiments would have tens or hundreds of magnetic domain walls, while only a few existed in the simulation. This means that, if one magnetic domain wall bends near the twin boundary, as seen in Figures 5.8b and 5.9b, this contributes a much larger increase in total domain wall energy than in a sample with many magnetic domain walls.

In the simulation, the small specimen size and assumption that magnetization is invariant through the *z* dimension of the sample results in a system which is more confined in terms of the magnetic structures which can form. However, the assumption that magnetization is homogeneous through the *z* dimension of the sample is valid for a

homogeneously magnetized twin domain, and only plays a role when twin domains contain 180° magnetic domains. The suppression of 180° magnetic domains perpendicular to the *z* direction leads to quantitative deviations; the qualitative conclusions are sound.

The derivative of the torque found from numerical simulations is approximately a factor of 50 less than the torque measured on a bulk single crystal specimen. We attribute this discrepancy to the difference in sample size, where the simulated sample is 4 orders of magnitude smaller in each dimension. The simulated results do show the same trend in maximum torque seen in experiments. At 3% strain, the BAB microstructure required the largest torque to rotate, the sample with a single twin boundary required the least, and the ABA microstructure required slightly more than the single twin and substantially less than the BAB microstructure. The numerical simulations provide a qualitative basis to analyze the results in terms of the magnetization of the twin domains.

The magnetization of twin domains is driven by the external field, but depends on the twin boundaries and crystal surface. The interfaces at the twin boundaries and crystal surfaces create a stray field if there is a divergence of magnetization. At crystal surfaces, any normal component of magnetization at the surface results in stray field energy. At the twin boundary, the stray field vanishes if the component of magnetization normal to the interface is constant across the interface. A discontinuity of the normal component of the magnetization increases the stray field energy.

In the BAB microstructure, the twin domains saturate fully while at the same angle and field magnitude the ABA microstructure does not. In the BAB microstructure, any 180° magnetic domain wall must pass through all three twin domains in order to

maintain continuity across the twin boundaries because 180° boundaries in the A twin domain are parallel to the lateral crystal surfaces and span from one twin boundary to the other. If continuity is not maintained, the divergence of magnetization creates a large stray field energy. Therefore, the formation of 180° magnetic domains would result in a relatively large volume of demagnetizing magnetic domains and, thus, an increase in Zeeman energy. In contrast, in the ABA microstructure, the 180° magnetic domain boundaries are perpendicular to the lateral surfaces. Therefore, these domain boundaries can extend from surface to surface without interacting with the twin boundaries in the B twin domain. The central B twin domain formed magnetic domains while not impacting the magnetic domain structure of the A twin domains. The blue magnetic domains in the A domains impact the magnetic domain structure in the intermediate B domain. The blue magnetic domains are positioned at the lateral surface of the A twin domain such that the enforced green magnetic domains in the B twin are minimal, and only one magnetic domain wall forms. For the ABA microstructure, the magnetic domains have more freedom to minimize the total energy compared to the BAB microstructure. Consequently, the total energy rises more quickly with deviation from the equilibrium orientation and the torque is larger for the BAB microstructure than for the ABA microstructure.

Simulation results revealed the interaction of the twin domain boundary with 180° magnetic domain walls when magnetic domain walls do not intersect the twin boundary. In the AB twin microstructure, the B twin domain has two green magnetic domains and four 180° magnetic domain walls (Figure 5.9b). The three 180° magnetic domain walls on the right are straight; they are perpendicular to the lateral surfaces and extend through

the width of the B twin domain in a straight line. The leftmost green domain is curved. It is thin on the top such that it does not intersect the twin boundary, and gets wider toward the bottom where the twin boundary angles away from the 180° magnetic domain wall. The green domain in the ABA twin microstructure has a similar shape (Figure 5.6c). Both 180° magnetic domain walls curve such that the green magnetic domain shifts further away from the twin boundary near the top and bottom lateral surfaces. This constitutes a second, long range interaction between twin boundaries and magnetic domain boundaries in addition to the continuity requirement discussed above.

Besides the twin boundaries, the surfaces also add to the difference in magnetic domain structures. The direction of easy magnetization stands perpendicular to the lateral surfaces for the B twin domains and perpendicular to the end faces for the A twin domains. At 3% strain, the B domain has direction of easy magnetization normal to half of the lateral surfaces. In the ABA microstructure, the A domains have direction of easy magnetization normal to both end faces while the BAB microstructure the A domain does not interact with the crystal surface. The BAB microstructure has magnetization normal only to half of the lateral surfaces; the ABA microstructure has magnetization normal to half the lateral surfaces plus the end faces. If the twin domains are individually saturated (such as in Figure 5.8b for the BAB twin microstructure) and for an aspect ratio of 3:1, the BAB microstructure has magnetization normal to 3/8 the perimeter sample surface while the ABA microstructure has magnetization normal to 5/8 of the perimeter sample surface. Therefore, the free surfaces create an additional driving force for the formation of magnetic domains which is 67% larger for ABA microstructure compared with the BAB microstructure.

In the sample with the AB microstructure (single twin boundary), twin domain A saturates at low magnetic fields due to the small stray field. When saturated, the magnetization of the A domain is perpendicular to a small surface area, which results in small internal field. The B domain has 180° magnetic domains since the direction of easy magnetization is perpendicular to a larger surface area. The saturation of domain A forces the portion of domain B with direction of easy magnetization normal to the twin boundary to have no magnetic domain walls. This is the yellow area of the B domain under the twin boundary in Figure 9b. This minimizes the divergence of magnetization at the twin boundary which minimizes the stray field energy. With decreasing strain, the volume fraction of the B domain decreases. The volume of the B domain forced to have no domain walls by the twin boundary (yellow area under the twin boundary) stays constant. Thus, as the strain decreases, the net magnetization of B increases. The net magnetization of the B domain is inversely proportional to the strain. As evidenced by the sample with two twin boundaries, larger net magnetization results in larger torque. In experiments, at 3% strain and above, the torque required to rotate the specimen with one twin boundary is smaller than for with the sample with the BAB microstructure. In contrast at 2% strain, the torque for the AB microstructure is similar to the BAB microstructure. The twin boundary causes a higher net magnetization of the B domain at 2% strain than at 3% strain; and this higher net magnetization results in a higher torque.

At 200 mT and above, the experimental torque is asymmetric about the equilibrium angle. The torque rises monotonically in the negative γ direction but goes through two inflections in the positive γ direction (Figure 5.4a). For magnetic fields larger than 500 mT, the torque goes through a local maximum and then through a local

minimum. This causes a bifurcation in the torque-controlled experiment (Figure 5.4b). The simulated results for a sample with one twin boundary at 2% strain in an external field of 500 mT shows a decrease in energy in the positive γ direction (Figure 5.10). The total energy forms a biased double well with a lower minimum in the negative and a higher minimum in the positive γ direction. This double well potential corresponds to the experimental results of the sample with one twin boundary and 4% strain. In contrast, the experimental behavior of the sample with 2% strain corresponds to a potential as indicated by the black dotted line in Figure 5.10a. Thus, the calculations overestimate the energy depression in the positive γ direction.

The angular width of the bifurcation decreases with increasing external magnetic field above 500 mT. The equilibrium angle depends on the external magnetic field, and decreases in magnitude above 500 mT as well. The jump in angle in the clockwise direction is roughly twice the equilibrium angle. Considering the energy double well as the sum of two parabolas with minima in positive and negative γ, the width of bifurcation depends on the position of the minimum in the positive γ direction. As the external magnetic field increases, the position of the minimum increases. As the external field increases above saturation, the torque due to Zeeman energy goes to zero as the magnetization and magnetic field are parallel. The magnetocrystalline anisotropy and stray field energies increase toward a constant relationship with γ, where the stray field depends on $\sin(\gamma)$ and the magnetocrystalline anisotropy energy depends on $\sin(2\gamma)$. The increase of two energies and decrease of the other leads to the dependence of the angle jump on magnetic field magnitude, but more simulations are required to fully understand the contributions.

The equilibrium angle always occurs such that the component of the magnetic field perpendicular to the twin boundary is larger than the component parallel to the twin boundary. The change in magnetization perpendicular to the twin boundary is similar in the positive and negative γ directions (Figure 5.10b). The divergence of the magnetization perpendicular to the twin boundary is almost a factor 4 less when the magnetic field is perpendicular to the twin boundary than when it is parallel to the boundary (Figure 5.10c). Although the change in magnetization is similar for each case, the field parallel to the twin boundary (positive γ) creates a larger magnetization divergence and larger stray field energy than the field perpendicular to the twin boundary (negative γ). The smaller divergence in the positive γ direction contributes to the asymmetry of the double well.

The divergence in magnetization at the twin boundary results in effective positive magnetic charges at the twin boundary interface. These charges have a magnetic field which works to rotate the heads of the magnetic vectors away from the twin boundary. This increase in rotation results in larger magnetocrystalline anisotropy energy. This is why the magnetocrystalline anisotropy energy has a higher local minimum energy in the positive γ direction (Figure 5.10d). The rotation of the magnetization also rotates the magnetic vectors more parallel to the external magnetic field. Figure 5.10d shows the Zeeman energy is slightly less in the positive than in the negative γ direction. While the change in total stray field slightly increases in the positive γ direction, the divergence at the twin boundary results in a larger total increase in the magnetocrystalline anisotropy energy. If the divergence in magnetization was equal for both positive and negative γ, the sample at 2% strain would have two unique equilibrium angles. The angle of the twin

boundary and difference in magnetization divergence for perpendicular or parallel orientation of the external magnetic field is the reason for the single equilibrium angle.

These results have direct implications on the design of actuators. For example, the BAB microstructure has the lowest total energy and largest torque for 3% strain and above. This suggests a twin domain microstructure might form which minimizes energy and maximizes torque. In linear actuators, torque leads to friction and loss of work output [27,28] and potentially to wear and fatigue [29]. The sample with a single twin domain had the largest torque at 2% sample strain, but the least torque at 3% strain. In an application where torque must be minimized, a single twin boundary is better at high sample strains. If possible, an actuator designer should target the ABA microstructure to minimize torque in a sample with an unconstrained end.

The magnetization in the A domain saturates at low fields. This makes the magnetization in the long dimension of the sample predictable. The twin domains in the BAB microstructure area saturates for low fields due to the stray field. A two-dimensional strain sensor would benefit from this microstructure. For sensing applications which sense with the magnetic flux, many twin boundaries will decrease the flux through the material [30]. The BAB microstructure, containing only two twin boundaries, is completely saturated for low fields due to the stray field. Targeting a microstructure which saturates at low fields but contains few twin boundaries would benefit sensing applications which sense with magnetic flux.

Kucza *et al.* proposed a microstructure in a bending sample with two twin domains and non-parallel twin boundaries [3]. Twin boundaries between the same two domains and non-parallel twin boundaries would result in large magnetization divergence

at the boundary more parallel to the external field. It is possible that, small twin domains with direction of easy magnetization perpendicular to the field would form in order to minimize the stray field energy at the expense of increased Zeeman energy. This adds another variable to the complexity of modeling these actuators.

5.9 Conclusions

The magnetization of and, hence, torque on a single crystal Ni-Mn-Ga sample in a magnetic field and constrained with respect to bending depends on the strain and twin boundary structure. The twin boundary structure changed the torque by a factor of up to 1.7 for samples with equivalent strain and in the same external magnetic field. The results of numerical micromagnetic simulations qualitatively matched experimental results. Simulations predicted larger torque in the twin structure which showed larger torque in experiments. The simulations further revealed the microstructure with larger torque had smaller total energy, which suggests a twin structure may form in an unconstrained sample which minimizes energy but maximizes torque.

Micromagnetic simulations showed that the twin boundary interface forces homogeneous magnetization in twin domains when the magnetization impinged on the twin boundary. In cases where the axis of easy magnetization was normal to the surface of the specimen, the twin domain split into multiple 180° magnetic domains. If the axis of easy magnetization was parallel to the lateral surface, the twin domain did not split into 180° magnetic domains if the neighboring twin domain was homogeneously magnetized. Although a homogenously magnetized domain is not energetically favorable according to the external field energy, the twin boundary interface forced this magnetic domain structure to avoid magnetization divergence at the interface. The divergence of

magnetization at the twin boundary interface is maximum when the magnetic field is parallel to the twin boundary. The equilibrium angle always occurred such that the magnetic field made an angle less than 45° with the normal to the twin boundary. This was the case for samples containing one or two twin boundaries.

This study demonstrates a large dependence of the torque and magnetic energies on the twin microstructure. Thus, the design of MSMA-based actuators and sensors must include design of the twin microstructure and a strategy to maintain this twin microstructure over the duration of the operation of the device.

5.10 Acknowledgements

The authors would like to thank Eric Rhoads for single crystal growth and sample preparation, Danielle Nichols and Justina Freilich for help conducting experiments, Andrew Armstrong for shot-peening, Tammy Jackson for machining sample holders, and Juan Manuel Hernandez Calderon for helpful discussions. We thank Nanosteel for donation of equipment and the Micron School of Materials Science and Engineering for financial support.

5.11 References

[1] O. Heczko, Materials Science and Technology 30, 1559 (2014).

[2] P. Zheng, N. J. Kucza, C. L. Patrick, P. Mullner, and D. C. Dunand, Journal of Alloys and Compounds 624, 226 (2015).

[3] N. J. Kucza, C. L. Patrick, D. C. Dunand, and P. Mullner, Acta Materialia 95, 284 (2015).

[4] P. Mullner and K. Ullakko, Physica Status Solidi B-Basic Research 208, R1 (1998).

[5] P. Mullner, V. Chernenko, M. Wollgarten, and G. Kostorz, Journal of Applied Physics 92, 6708 (2002).

[6] R. C. O'Handley, Modern Magnetic Materials (Wiley, New York, 2000).

[7] R. C. O'Handley, S. J. Murray, M. Marioni, H. Nembach, and S. M. Allen, Journal of Applied Physics 87, 4712 (2000).

[8] B. Kiefer and D. C. Lagoudas, Philosophical Magazine 85, 4289 (2005).

[9] N. S. Kiselev, I. E. Dragunov, A. T. Onisan, U. K. Roessler, and A. N. Bogdanov, European Physical Journal-Special Topics 158, 119 (2008).

[10] A. T. Onisan, A. N. Bogdanov, and U. K. Roessler, Acta Materialia 58, 4378 (2010).

[11] N. N. Sarawate and M. J. Dapino, Journal of Applied Physics 101, 123522 (2007).

[12] B. Kiefer and D. C. Lagoudas, Journal of Intelligent Material Systems and Structures 20, 143 (2009).

[13] Y. W. Lai, N. Scheerbaum, D. Hinz, O. Gutfleisch, R. Schafer, L. Schultz, and J. McCord, Applied Physics Letters 90, 192504 (2007).

[14] Y. C. Liang, H. Kato, M. Taya, and T. Mori, Scripta Materialia 45, 569 (2001).

[15] A. Hobza and P. Müllner, Shape Memory and Superelasticity (2017).

[16] E. M. Lifshits and L. D. Landau, Phys. Zeitsch. der Sow 8, 153 (1935).

[17] D. Kellis, A. Smith, K. Ullakko, and P. Muellner, Journal of Crystal Growth 359, 64 (2012).

[18] X. P. Wang, C. J. Garcia-Cervera, and E. Weinan, Journal of Computational Physics 171, 357 (2001).

[19] C. J. Garcia-Cervera and W. E, Ieee Transactions on Magnetics 39, 1766 (2003).

[20] D. I. Paul, W. McGehee, R. C. O'Handley, and M. Richard, Journal of Applied Physics 101, 123917 (2007).

[21] O. Heczko, V. Kopecky, L. Fekete, K. Jurek, J. Kopecek, L. Straka, and H. Seiner, Ieee Transactions on Magnetics 51, 2505304 (2015).

[22] V. Kopecky, L. Fekete, O. Perevertov, and O. Heczko, Aip Advances 6, 056208 (2016).

[23] A. Diestel, V. Neu, A. Backen, L. Schultz, and S. Fahler, Journal of Physics-Condensed Matter 25, 266002 (2013).

[24] A. Budruk, C. Phatak, A. K. Petford-Long, and M. De Graef, Acta Materialia 59, 4895 (2011).

[25] Y. W. Lai, R. Schafer, L. Schultz, and J. McCord, Applied Physics Letters 96, 022507 (2010).

[26] V. A. Chernenko, R. L. Anton, J. M. Barandiaran, I. Orue, S. Besseghini, M. Ohtsuka, and A. Gambardella, Ieee Transactions on Magnetics 44, 3040 (2008).

[27] T. Schiepp, V. Detkov, M. Maier, E. Pagounis, and M. Laufenberg, in 4th Int Conf on Ferromagnetic Shape Memory Alloys, ICFSMA, edited by P. Müllner, and W. B. KnowltonBoise, ID, 2013), pp. 48.

[28] M. Chmielus, I. Glavatskyy, J.-U. Hoffmann, V. A. Chernenko, R. Schneider, and P. Muellner, Scripta Materialia 64, 888 (2011).

[29] M. Chmielus, V. A. Chernenko, W. B. Knowlton, G. Kostorz, and P. Mullner, European Physical Journal-Special Topics 158, 79 (2008).

[30] N. Gabdullin and S. H. Khan, Ieee Transactions on Magnetics 53, 4900108 (2017).

[31] V. A. Chernenko, V. A. L'Vov, P. Mullner, G. Kostorz, and T. Takagi, Physical Review B 69, 134410 (2004).

[32] V. Runov and U. Stuhr, Journal of Magnetism and Magnetic Materials 323, 244 (2011).

[33] A. Sozinov, A. A. Likhachev, and K. Ullakko, IEEE Transactions on Magnetics 38, 2814 (2002).

CHAPTER SIX: DISCUSSION

The relationship between the twin boundary interfaces and the crystal surface drive the magnetization and subsequent magneto-mechanical response of magnetic shape memory alloys. The relative orientation of the twin boundary with the axis of easy magnetization (AEM) and the surface allows or forbids magnetic domains and domain walls to maintain continuity across twin boundaries. Continuity of magnetic domains results in small stray field energy at twin boundary interfaces. In contrast, any discontinuity of the magnetic domains causes a large contribution to the stray field energy. The combination of the magnetocrystalline anisotropy energy and stray field energy determines the component of the magnetization normal to the crystal surface. The component of magnetization normal to the crystal surface contributes to the stray field energy as does magnetization divergence in the crystal. Depending on the twin microstructure and on the geometry, one or the other effect dominates.

Consider for example the difference in ABA and BAB twin microstructures, discussed in Chapter 5. We assume a length to width aspect ratio of 3:1. At 3% strain, the BAB microstructure has the AEM normal to half of the lateral crystal surfaces, while the ABA microstructure has AEM normal to half of the lateral crystal surfaces and to the entire crystal end faces. The ABA microstructure has AEM normal to 67% more surface area than the BAB microstructure. Therefore, the surfaces in the ABA microstructure provide a larger stray field energy to drive the twin domains to demagnetize. The larger stray field energy causes the ABA microstructure to split into 180° magnetic domains. In

the BAB microstructure, the interaction of the magnetization with the surface does not produce a large enough stray field to drive demagnetization in the BAB microstructure. Therefore, the BAB twin microstructure does not develop 180° magnetic domains.

The surface drives the demagnetization of twin domains to decrease the stay field energy. In both twin microstructures, discontinuous 180° magnetic domains do not form such as to demagnetize one domain, but increase the stray field energy at the twin boundary. As the angle between magnetic field and long axis of the sample increases, the external magnetic field becomes more parallel to the direction of easy magnetization in the B twin domain. As the angle increases, in the ABA twin microstructure, 180° magnetic domains grow to decrease the stray field energy the surfaces cause in the A twin domain. The magnetic domain walls maintain continuity, which causes the demagnetizing domain in the neighboring B twin domain to grow as well. The demagnetizing domain in twin domain A grows, even though this corresponds with demagnetizing magnetic domain growth in the B twin domain. The demagnetizing green domain increases the Zeeman energy. The increase in Zeeman energy is energetically favorable compared with the case where the blue and yellow magnetic domains intersect at the twin boundary, which would result in diverging magnetization and large stray field energy at the twin boundary.

In the case of the BAB microstructure, if one 180° magnetic domain wall forms in twin domain A, the twin domain configuration would force the magnetic domain walls to maintain continuity across both twin boundaries and span all three twin domains (Figure 6.1). If a small blue domain nucleates to demagnetize the A twin domain, the domain boundary continuity would force a large green domain to nucleate in the right B twin

domain. Due to the magnetic domain continuity across the twin boundaries, the A twin domains are not able to form small, demagnetizing magnetic domains without greatly increasing the area of demagnetizing magnetic domains in the B twin domain. The nucleation of one magnetic domain wall would lead to a large area of demagnetizing magnetic domains in the B twin domain. Thus, the twin domains remain magnetically saturated. This occurs instead of only the central A twin domain demagnetizing, which would result in magnetization divergence and a large stray field at the twin boundaries. The twin domains do not have the freedom to demagnetize with small 180° magnetic domains due to the stray field energy, which causes a large increase in energy away from the equilibrium angle. Therefore, the BAB microstructure required larger torque to rotate than the ABA microstructure. The magnetization and occurrence of 180° magnetic domains is driven by both the stray field at the surface and at the twin boundaries.

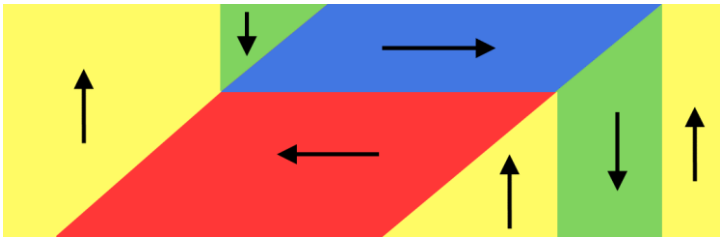

Figure 6.1 A schematic of magnetic domain nucleation in the BAB twin microstructure with a continuous magnetic domain wall. If a small demagnetizing magnetic domain nucleates in the left B twin domain, 180° magnetic domain with large area must also nucleate in the A domain and in the right B twin domain.

In the torque experiments, the equilibrium angle always occurs such that the directions of the magnetic field and of the twin boundary normal included an acute angle. The sample microstructure is constrained but the sample is free to rotate in the magnetic field. Although the angle of the magnetic field is measured relative to the sample edge, the important relationship is the field to the twin boundary. At $\gamma = 0°$, the field has a 45°

angle with the twin boundary. The equilibrium angle occurs such that the angle between the field and twin boundary is between 45° and 90°. The angle γ_{eq} depends on the orientation of the twin boundary to the external magnetic field. The geometry of the sample and the strain determine the magnitude of the equilibrium angle, but the twin boundaries determine whether the equilibrium angle occurs in the positive or negative γ direction.

Simulations reveal the dependence of the local stray field on the angle between the external magnetic field and twin boundary. The AEM changes orientation across the twin boundary. The change in magnetization perpendicular to the twin boundary for a sample at 2% strain containing one twin boundary in an external magnetic field of 500 mT is given in Figure 6.2a. The magnetic field is perpendicular to the twin boundary at γ = -45° and parallel to the twin boundary at γ = +45°. The change in magnetization is nearly symmetric about γ = 0°. However, the divergence of magnetization is asymmetric about γ = 0° (Figure 6.2b). The divergence is maximum near γ = +45°, which is when the magnetic field is parallel to the twin boundary. The divergence has an absolute minimum near -45°, the perpendicular orientation. The change in magnetization and divergence at the twin boundary at γ = 0° is zero because the sample was nearly saturated at that angle. At a smaller magnetic field where the sample was less saturated, there would still be a finite difference in magnetization direction and divergence in magnetization at γ = 0°.

Color plots and magnetization vectors across the twin boundary are given for the external magnetic field nearly parallel to the twin boundary (+40°, Figure 6.3a) and nearly perpendicular to the twin boundary (-40°, Figure 6.3b). The red boxes denote the areas that the magnetic vectors depict. The magnetic vectors line up head to tail for the

perpendicular orientation, but slightly head to head for the parallel orientation. Head to head orientation results in a divergence of magnetization across the twin boundary. The divergence in magnetization creates effective "magnetic charges" at the twin boundary, which have a magnetic field (stray field) that points in the opposite direction of the magnetization. The stray field works to rotate the magnetic moments away from the charges, decreasing the magnetization divergence. This rotation also increases the magnetocrystalline anisotropy energy and decreases the Zeeman energy since the magnetic vectors rotate more parallel to the external magnetic field. The increase in the total stray field energy due to magnetic charges at the twin boundary is relatively small, but the stray field affects both the Zeeman and magnetocrystalline anisotropy energies as well. Therefore, the sample energy is strongly asymmetric about the angle $\gamma = 0°$.

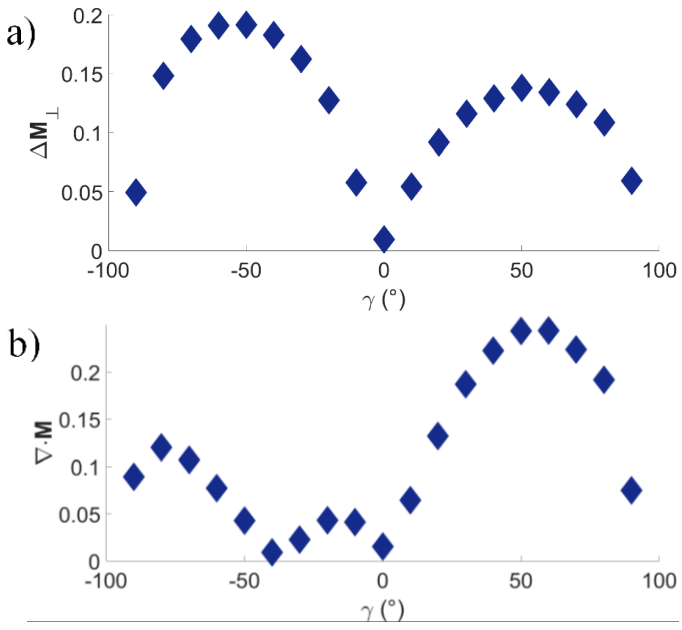

Figure 6.2 The change in perpendicular magnetization (a) at the twin boundary and the divergence of the magnetization (b) are given as a function of gamma. The units of magnetization are the normalized magnitude of the magnetic vector. The simulation was done for a sample at 2% strain containing one twin boundary in an external magnetic field of 500 mT. While the change in magnetization perpendicular

to the twin boundary is nearly symmetric about γ = 0°, the divergence has an absolute minimum near γ = -45° and a maximum near γ = +45°.

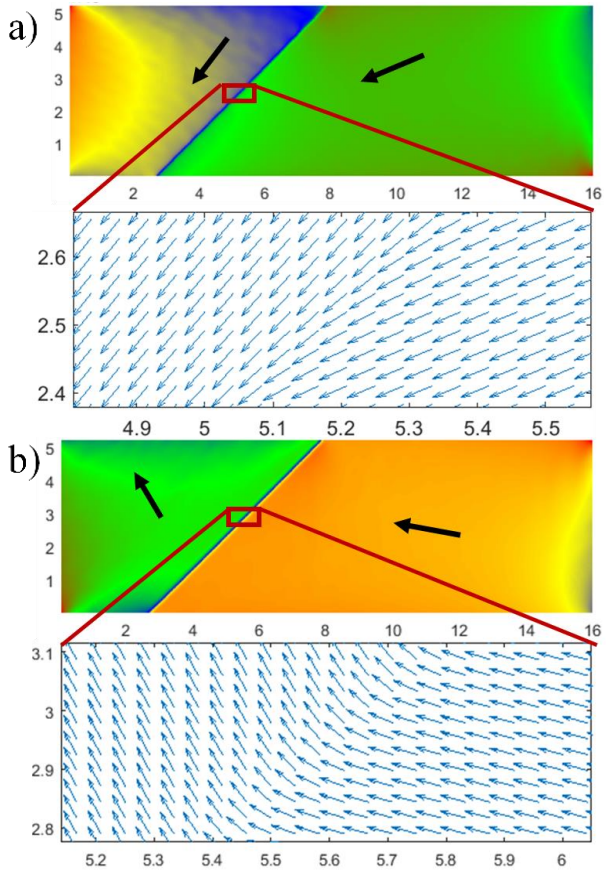

Figure 6.3 Simulation results for the magnetization of a sample with one twin boundary at 2% strain in an external magnetic field of 500 mT is given for γ = +40° (a) and γ = -40° (b). For γ = +40°, the external magnetic field is nearly parallel to the twin boundary and the divergence of the magnetization at the twin boundary is close to a maximum (Figure 6.2b). At γ = -40° the external magnetic field is nearly perpendicular to the external magnetic field and the divergence of mangetization is nearly zero. For both angles, the direction of magnetic vectors across the twin boundary are shown in a location denoted by the red box in the color plot.

In the case of a single twin boundary, the A twin domain saturates at low fields, while the B domain contains 180° magnetic domains (Figure 6.4). The B domain has direction of easy magnetization perpendicular to half of the lateral surface area, while the A domain has direction of easy magnetization perpendicular only to one edge. The interaction of the magnetization in the B domain with the surface causes a larger stray

field if the B domain has a net magnetization. At 3% strain, the B domain has direction of easy magnetization perpendicular to three times the surface area as the A domain, and therefore the driving force to demagnetize is larger. The B domain tends to demagnetize since the direction of easy magnetization in the B domain is normal to a large lateral surface area. At large strains, the B twin domain has the freedom to demagnetize while not increasing the energy in neighboring twin domains, which decreases the energy and torque at large strains. In experiments, the torque required to rotate a sample with one twin boundary and strains larger than 3% was comparable to the ABA twin microstructure which has lower torque than the BAB domain and less surface area with AEM perpendicular to it.

The continuity of magnetization across the twin boundary forces a certain portion of domain B to contain no 180° magnetic domain walls due to the saturation of twin domain A. This driving force for no domain walls counteracts the driving force of the surface to create 180° magnetic domain walls in twin domain B, which demagnetizes to decrease the stray field energy. As the strain decreases, the total volume of the B domain decreases. The volume of the B domain forced by the twin boundary and saturated A twin domain to have no magnetic domain walls stays the same. Thus, the fraction of domain B forced to have no domain walls increases with decreasing strain. At 1% strain or less, the B twin domain would be fully saturated because in this case there is no sliver that spans from lateral surface to lateral surface without containing a twin boundary. Therefore, at strains of 1% or less both twin domains are saturated; the torque should be comparable to the BAB microstructure.

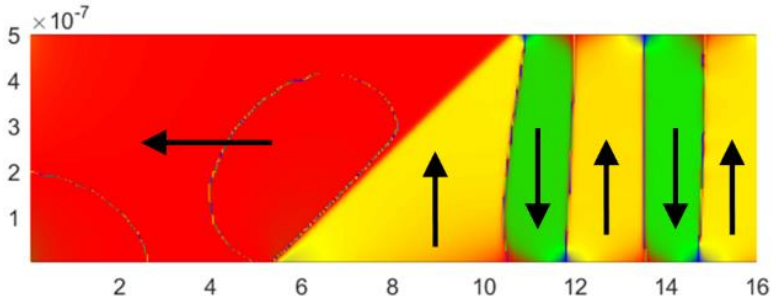

Figure 6.4 A sample containing one twin boundary at 3% strain in an external field of 75 mT at an angle of γ = -30°

At larger strains, the magnetization saturates at larger fields because of the large driving force to create green 180° magnetic domains in the B twin domain. From the simulation results for the ABA and BAB microstructures, larger torque is required to rotate the sample when the twin domains are saturated. As the strain decreases, the sample saturates more quickly. This explains why the torque increases more quickly with increasing field as strain decreases (Figure 6.5).

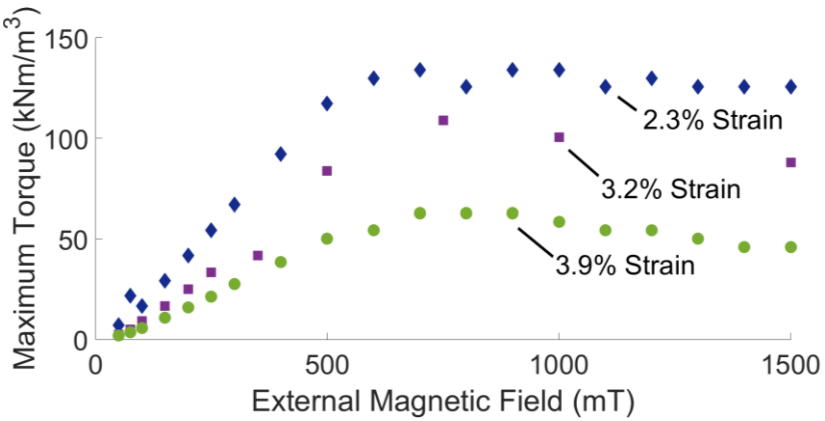

Figure 6.5 The maximum torque as a function of external magnetic field for a sample with one twin boundary at 3 different strains.

One might infer that the torque increases to the same level as the sample saturates; however, this was not seen in experiments. The largest torque occurs for an external magnetic field of approximately 700 mT, which is very close to the field needed to saturate the crystal perpendicular to the AEM. The maximum torque at 700 mT increases

with decreasing strain. As the field increases above the saturation field, the torque decreases slightly. We analyze the contribution of each energy term to the torque above magnetic saturation to understand why the torque does not tend toward the same value for different strains, and why the torque decreases above saturation.

Above the saturation field, we assume the net magnetization is constant and parallel to the external magnetic field. If **M** and the angle between **M** and $\mathbf{H_e}$ are constant, then the Zeeman energy does not change as γ changes and does not contribute to torque above saturation. At low fields, the Zeeman energy changes the most and contributes the most to the torque on the specimen. As the field increases close to the saturation field, the torque due to Zeeman energy decreases until it reaches the minimum at the saturation field. This applies to all strain values.

To understand the dependence of the decrease in torque on the strain, we investigate the interaction of the stray field and the magnetocrystalline anisotropy. In Chapter 4, the dependence of the torque on strain was attributed to the interaction of these two driving forces and the relationship between the AEM and crystal surface. This interaction changes drastically if the magnetic moments are parallel to the field and not the AEM.

If the crystal is homogeneously magnetized, we can calculate the stray field energy in terms of the geometry-dependent demagnetization factor. The demagnetization factor is small in the long dimension of the crystal and large in the short dimension. The energy is smallest when the field and magnetization are parallel to the direction with the small demagnetizing factor (i.e. at $\gamma = 0$ and 180°). The stray field energy depends on γ as

a -cosine function. The torque on the sample due to the stray field energy depends on γ following a sine function.

Using the convention for strain in Chapter 4, the volume fraction of domain B is proportional to E = $\varepsilon/\varepsilon_{max}$ and the volume fraction of domain A is proportional to 1-E. The magnetocrystalline anisotropy energy for the entire crystal is given by

$$\mathrm{E}_{\mathrm{anis}} = K_u(E\cos^2\gamma + (1-E)\sin^2\gamma) \tag{6.1}$$

The torque due to the magnetocrystalline anisotropy energy is

$$\theta_{\mathrm{anis}} = K_u(2\sin 2\gamma - 4E\sin 2\gamma) \tag{6.2}$$

The torque due to mangetocrystalline anisotropy energy has a sine dependence on γ as well, but with half the period. The torque decreases with sample strain. At 2% strain (E = 1/3), the torque due to magnetocrystalline anisotropy and stray field energy act synergistically, while at 4% strain (E = 2/3) the two act antagonistically. i.e. the two driving forces work against each other. At 3% strain (E = ½), the torque due to magnetocrystalline anisotropy is zero. At 3% strain, the torque on the sample is solely due to the shape anisotropy, which changes the stray field energy as a function of γ.

At 3% strain and above saturation, the torque is solely due to the shape anisotropy and difference in stray field for different orientations of the sample in the external magnetic field. At smaller strains, the magnetocrystalline and shape anisotropy energies act synergistically as both are proportional to plus sineγ, leading to larger torque than for 3% strain. At larger strains, the torque due to magnetocrystalline anisotropy is proportional to negative sineγ while the shape anisotropy is still proportional to plus sineγ. The two energies act antagonistically, leading to a smaller torque than for 3%

strain. This explains why the torque does not tend toward the same value above saturation for different sample strains.

The torque required to rotate the sample decreases above saturation. For 2% strain, this decrease is only 6% of the maximum torque (near 700 mT), while at 4% strain the decrease is over 25% of the maximum torque (near 700 mT). Some of the decrease in torque is attributed to the decrease in torque due to Zeeman energy above saturation. Analyzing the energy contributions above saturation does not explain the dependence of the decrease in torque above saturation on the strain. We must know how the energies depend on γ approaching saturation to relate to the dependence above saturation. More simulations must be performed, as analytical solutions are not available since we cannot assume a linear relationship between γ and the orientation of the magnetic vectors in the sample.

6.1 Strain Sensing

The sample in the torque experiments has a constrained twin microstructure and strain, but rotates freely in the magnetic field. The freedom to rotate allows the sample to take an angle which enables the magnetic domain walls to maintain continuity across twin boundaries. This is not the case during the strain sensing experiments. Here, the sample is not free to rotate, and has a changing twin domain microstructure. The magnetic energy is not minimized by sample rotation, and, therefore, there occurs large magnetization divergence at twin boundaries which results in larger stray field energy.

In the strain sensing experiments, the RMS amplitude of the voltage on the measurement coil increases non-linearly with decreasing strain. The time-varying magnetic flux through the coil creates a proportional voltage. The magnetic flux is the

sum of the magnetic field and magnetization. The magnitude of the change in field and magnetization determine the amplitude of the output voltage. If the twin domains are magnetically saturated, the magnetization changes linearly with strain. The sample strain also affects the magnetic field through the sample, since the voltage depends non-linearly on strain.

Dynamic magneto-mechanical testing results in many twin boundaries [117]. Simulations shows that, for a sample with many twin boundaries, the twin domains saturate. If twin domains are saturated), a value for the stray field can be approximated by the geometry-dependent demagnetization factor. The stray field increases with increasing demagnetization factor.

The change of magnetization (which changes the internal magnetic field) in the axis of the coil, which is the *x* direction, affects the voltage. The voltage of the pickup coil varies with the volume fraction of the A twin domain. As the sample strain decreases, the width of A twin domains increases. With increasing width, the demagnetization factor in the *x* direction in these domains decreases. Figure 6.6 gives the demagnetization factor in the *x* direction of the A twin domain [118], assuming the sample contains one twin boundary and rectangular twin domains. As the volume fraction of the A twin domain increases, the stray field decreases. The stray field works to decrease the flux in the coil. As the strain decreases, the flux increases with the magnetization of the A domain and because of the smaller stray field. The increase in flux gives a larger voltage amplitude in the pickup coil at smaller strains. The experiments show a non-linear increase in voltage with decreasing strain, which is caused by the increase in flux with decreasing strain.

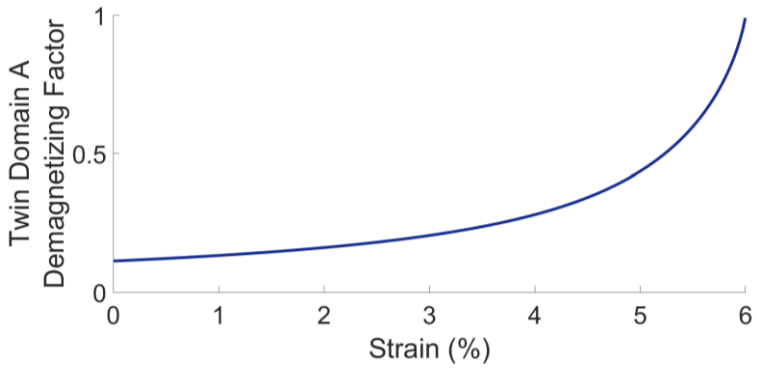

Figure 6.6 The demagnetizing factor for twin domain A in a single twin boundary specimen is given as a function of sample strain. At 0% strain, the sample contains only twin domain A, and at 6% strain twin domain A does not exist. The demagnetizing factor and stray field increase with increasing strain. The demagnetizing factor was calculated based on the continuous function given by Equation 1 in Ref. 118.

The dynamic voltage across the drive coil produces a magnetic field of approximately 15 mT in the center of the coil. This voltage works to change the magnetization of the sample to produce a voltage in the pickup coil. If the sample contains many small twin domains, the stray field energy forces the A twin domains into saturation in a direction determined by the twin boundary. The 15 mT external field does not reverse the direction of magnetization, because the internal field is too large to overcome at this small field. The change in magnetization is small and varies the voltage only to a small extent. The ideal sensor produces a large change in voltage with a small strain change. The voltage signal is proportional to the change in magnetization. A large change in magnetization occurs if the sample contains mobile 180° magnetic domain walls. The ABA microstructure has large twin domains with mobile 180° magnetic domain walls. In a sample containing large twin domains with mobile 180° domain walls, the small external field moves 180° domain walls. This magnetizes the sample in the positive and negative direction in the axis of the coil. The large change in magnetization produces a large voltage signal, which increases the resolution of the strain sensor.

The stray field energy leads to a reduction in the voltage change and therefore reduces the strain sensing capability of the material if the sample contains many twin domains. The change in RMS amplitude of the pickup coil and strain sensing resolution increases with a coarse twin domain microstructure compared with a fine twin microstructure. In practice, the sample does not require an external magnetic field to elongate, and the twin domains with AEM in the axis of the coil is not forced into saturation. The strain sensing resolution is drastically different than in the experiments outlined in Chapter 3.

CHAPTER SEVEN: CONCLUSIONS AND OUTLOOK

The goal of this study was to characterize the influence of the internal magnetic field on the magnetization in single crystals of Ni-Mn-Ga martensite. The torque was measured as a function of external magnetic field, sample strain, and twin domain microstructure. The torque is the change in total magnetic energy as a function of the change in angle between the sample and external field. Micromagnetic simulation were performed to gain a qualitative understanding of the dependence of the energy and torque on the twin microstructure. The continuity of magnetization at twin boundaries to reduce stray field energy resulted in a strong dependence of the net magnetization and total energy on the twin domain microstructure. This qualitative understanding was applied to the strain sensing application to better understand the magnetic response from the sample and suggest improvements based on twin microstructure.

Torque experiments demonstrated a strong dependence of the twin microstructure on the torque and magnetic energy on samples with the same strain and external magnetic field. Micromagnetic simulations revealed the internal magnetic field distribution and the relationship between twin boundaries and sample surface, which leads to different magnetization response depending on the formation of 180° magnetic domains and relative orientation of the field with twin boundaries. In a sample with two twin boundaries, one microstructure resulted in completely saturated twin domains and the other contained 180° magnetic domains and a larger total energy. Therefore, we must

consider the twin microstructure when implementing magnetic shape memory elements into applications.

For instance, strain sensing applications use the magnetic response to detect the strain of the sample. In a sample with a fine twin microstructure all A twin domains which do not interact with the crystal ends saturate. The strain sensing method in the experiments reported in Chapter 5 have better resolution if a large change in magnetization occurs under a small alternating magnetic field. This happens only if the A twin domain had mobile 180° magnetic domain walls. The magnetic domain walls move to magnetize the A twin domains in different directions, resulting in a large change in magnetization. An actual application of this strain sensing measurement method does not require an orthogonal bias field to extend the sample. If the sample contains 180° magnetic domain walls and the voltage response would offer much better sensing resolution.

The twin domain microstructure could be manipulated such that the magnetization response is optimized for a given application. In linear actuators where torque and bending inhibits strain and leads to shorter lifetime, a microstructure should be targeted which reduces torque. In a bending actuator, such as a flap or valve, a twin microstructure which promotes bending is optimal. A twin microstructure forced into saturation is beneficial in an application which requires large flux or magnetic saturation such as energy harvesting. Constraints which keep the twin microstructure over the lifetime of the element must be included in system design.

The experiments and micromagnetic simulations reveal the strong dependence of magnetic energy on twin microstructure and provide a starting point to understand which

twin microstructures lead to optimal performance in a certain application. The experiments and simulations all contained one twin boundary, or multiple parallel twin boundaries. Studies should be carried out on specimen which contain non-parallel twin boundaries, as this will create a large divergence in magnetization at one twin boundary as exemplified in a wedge twin shown in Figure 7.1. Here, the left twin boundary has a low magnetic stray field energy since the magnetic moments meet head to tail on it. In contrast the right twin boundary has a high stray field energy since magnetic moments meet tail to tail on it (creating magnetic charges as indicated with negative symbols.) Such twin microstructures were produced by Straka *et al.* [22,119]. Possibly, a twin microstructure could be developed which manipulates the magnetization divergence and internal field energy such as to impose internal constraints on twin boundary motion and torque.

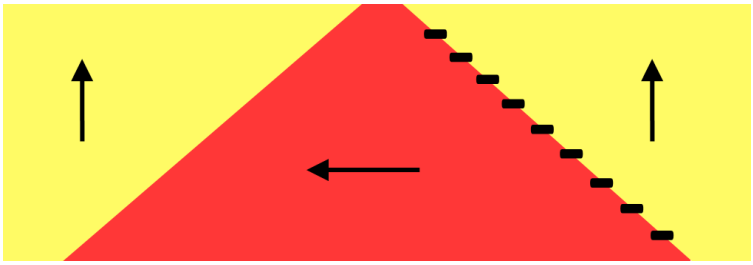

Figure 7.1 A sample containing two non-parallel twin boundaries would have a large divergence in magnetization at one twin boundary, depicted by negative signs on the right twin boundary.

The simulations for different twin microstructures were done at an external field of 75 mT. It would be most helpful to continue simulations in arrangements relevant for actuators, *i.e.* above the twinning stress. This would be the most helpful for future actuator design, and decrease the simulation time. Multiple angle sweeps would not be needed when the external field provides a large enough driving force for the

magnetization to reach equilibrium in 20,000 iterations of the energy minimization scheme. It may also be helpful to simulate a larger sample size to gain an understanding of the difference in magnetization with increased sample size. This is important because the torque in simulation and experiments were different by a factor of 50. We must know the origin of the differences in order to make assumptions when comparing simulations to macroscopic sample sizes.

The simulation does not currently account for interactions between defects or elastic strain fields and magnetic vectors near twin boundaries. Integrating defects would require knowing the local changes in the exchange and magnetocrystalline anisotropy energy constants near the twin boundary due to local differences in order and symmetry. This would require first-principles calculations for these energy constants, which is beyond the scope of this study. These interactions may become substantial in cases with more complex twin microstructures or intersecting twin boundaries which have high defect content and complex magnetic domain microstructures.

The twin boundaries in this study had large spacing; they were millimeters apart in experiments and on the order of one micrometer apart in simulations. The non-modulated phase of Ni-Mn-Ga with small amounts of cobalt and copper has shown MFIS [6], and forms nano-twins on the scale of nanometers and hierarchical microstructures [120-123]. This presents a unique situation to analyze, since the twin domain microstructure has many closely spaced changes in direction of easy magnetization and large defect content. The small scale of twinning means it is accessible to micromagnetic simulations.

Muntifering *et al.* [120-123] characterized the defect content of intra-variant boundaries in non-modulated martensite. These experimental results can be used to calculate changes in exchange and magnetocrystalline anisotropy energy constants. We may use this information to simulate the magnetic energetics of nano-twinned and hierarchical twinned microstructures in non-modulated martensite. This would give an understanding of magnetization processes with closely spaced changes in direction of easy magnetization and large defect content. Such a study may reveal the role magnetism plays in the formation and detwinning process of hierarchically twinning martensite.

References

[1] V. A. Chernenko, E. Cesari, V. V. Kokorin, and I. N. Vitenko, Scripta Metallurgica Et Materialia **33**, 1239 (1995).

[2] K. Ullakko, J. Huang, C. Kantner, R. OHandley, and V. Kokorin, Applied Physics Letters **69**, 1966 (1996).

[3] S. J. Murray, M. Marioni, S. M. Allen, R. C. O'Handley, and T. A. Lograsso, Applied Physics Letters **77**, 886, Pii [s0003-6951(00)00832-9] (2000).

[4] P. Mullner, V. Chernenko, M. Wollgarten, and G. Kostorz, Journal of Applied Physics **92**, 6708 (2002).

[5] A. Sozinov, A. A. Likhachev, N. Lanska, and K. Ullakko, Applied Physics Letters **80**, 1746 (2002).

[6] A. Sozinov, N. Lanska, A. Soroka, and W. Zou, Applied Physics Letters **102**, 021902 (2013).

[7] K. Ullakko, Journal of Materials Engineering and Performance **5**, 405 (1996).

[8] E. Faran and D. Shilo, Journal of the Mechanics and Physics of Solids **59**, 975 (2011).

[9] E. Faran and D. Shilo, Journal of the Mechanics and Physics of Solids **61**, 726 (2013).

[10] A. R. Smith, J. Tellinen, and K. Ullakko, Acta Materialia **80**, 373 (2014).

[11] *Encyclopedia of Smart Materials* (John Wiley and Sons, Inc., New York, 2002).

[12] G. H. Haertling, Journal of the American Ceramic Society **82**, 797 (1999).

[13] A. Sozinov, A. Likhachev, N. Lanska, K. Ullakko, and V. Lindroos, Journal De Physique Iv **112**, 955 (2003).

[14] I. Suorsa, E. Pagounis, and K. Ullakko, Applied Physics Letters **84**, 4658 (2004).

[15] P. Mullner, V. Chernenko, and G. Kostorz, Scripta Materialia **49**, 129 (2003).

[16] I. Suorsa, J. Tellinen, K. Ullakko, and E. Pagounis, Journal of Applied Physics **95**, 8054 (2004).

[17] I. Karaman, B. Basaran, H. Karaca, A. Karsilayan, and Y. Chumlyakov, Applied Physics Letters **90**, ARTN 172505 (2007).

[18] M. Chmielus, V. A. Chernenko, W. B. Knowlton, G. Kostorz, and P. Mullner, European Physical Journal-Special Topics **158**, 79 (2008).

[19] M. Chmielus, K. Rolfs, R. Wimpory, W. Reimers, P. Mullner, and R. Schneider, Acta Materialia **58**, 3952 (2010).

[20] T. Schiepp, V. Detkov, M. Maier, E. Pagounis, and M. Laufenberg, in *4th Int Conf on Ferromagnetic Shape Memory Alloys, ICFSMA*, edited by P. Müllner, and W. B. KnowltonBoise, ID, 2013), pp. 48.

[21] T. Lawrence, P. Lindquist, K. Ullakko, and P. Mullner, Materials Science and Engineering a-Structural Materials Properties Microstructure and Processing **654**, 221 (2016).

[22] L. Straka, N. Lanska, K. Ullakko, and A. Sozinov, Applied Physics Letters **96**, 131903 (2010).

[23] O. Heczko, D. Vokoun, V. Kopecky, and M. Beleggia, IEEE Magnetics Letters **6**, 1000204 (2015).

[24] N. J. Kucza, C. L. Patrick, D. C. Dunand, and P. Mullner, Acta Materialia **95**, 284 (2015).

[25] P. Zheng, N. J. Kucza, C. L. Patrick, P. Mullner, and D. C. Dunand, Journal of Alloys and Compounds **624**, 226 (2015).

[26] Y. C. Liang, H. Kato, M. Taya, and T. Mori, Scripta Materialia **45**, 569 (2001).

[27] P. Mullner and K. Ullakko, Physica Status Solidi B-Basic Research **208**, R1 (1998).

[28] R. C. O'Handley, Journal of Applied Physics **83**, 3263 (1998).

[29] R. C. O'Handley, S. J. Murray, M. Marioni, H. Nembach, and S. M. Allen, Journal of Applied Physics **87**, 4712 (2000).

[30] S. J. Murray, M. Farinelli, C. Kantner, J. K. Huang, S. M. Allen, and R. C. O'Handley, Journal of Applied Physics **83**, 7297 (1998).

[31] R. Tickle, R. D. James, T. Shield, M. Wuttig, and V. V. Kokorin, IEEE Transactions on Magnetics **35**, 4301 (1999).

[32] B. Kiefer, H. E. Karaca, D. C. Lagoudas, and I. Karaman, Journal of Magnetism and Magnetic Materials **312**, 164 (2007).

[33] O. Heczko, Materials Science and Technology **30**, 1559 (2014).

[34] N. S. Kiselev, I. E. Dragunov, A. T. Onisan, U. K. Roessler, and A. N. Bogdanov, European Physical Journal-Special Topics **158**, 119 (2008).

[35] A. T. Onisan, A. N. Bogdanov, and U. K. Roessler, Acta Materialia **58**, 4378 (2010).

[36] D. I. Paul, J. Marquiss, and D. Quattrochi, Journal of Applied Physics **93**, 4561 (2003).

[37] D. I. Paul, W. McGehee, R. C. O'Handley, and M. Richard, Journal of Applied Physics **101**, 123917 (2007).

[38] B. Kiefer and D. C. Lagoudas, Journal of Intelligent Material Systems and Structures **20**, 143 (2009).

[39] N. N. Sarawate and M. J. Dapino, Journal of Applied Physics **101**, 123522 (2007).

[40] A. Neudert, Y. W. Lai, R. Schafer, M. Kustov, L. Schultz, and J. McCord, Advanced Engineering Materials **14**, 601 (2012).

[41] V. Runov and U. Stuhr, Journal of Magnetism and Magnetic Materials **323**, 244 (2011).

[42] R. Tickle and R. D. James, Journal of Magnetism and Magnetic Materials **195**, 627 (1999).

[43] A. Sozinov, A. A. Likhachev, and K. Ullakko, IEEE Transactions on Magnetics **38**, 2814 (2002).

[44] F. Bitter, Physical Review **38**, 1903 (1931).

[45] P. Weiss, Comptes Rendus Hebdomadaires Des Seances De L Academie Des Sciences **145**, 1155 (1907).

[46] P. A. M. Dirac, Proceedings of the Royal Society of London Series a-Containing Papers of a Mathematical and Physical Character **112**, 661 (1926).

[47] W. Heisenberg, Zeitschrift Fur Physik **38**, 411 (1926).

[48] K. J. Sixtus and L. Tonks, Physical Review **37**, 930 (1931).

[49] E. M. Lifshits and L. D. Landau, Phys. Zeitsch. der Sow **8**, 153 (1935).

[50] F. Bloch, Zeitschrift Fur Physik **74**, 295 (1932).

[51] W. Heisenberg, Zeitschrift Fur Physik **69**, 287 (1931).

[52] E. C. Stoner and E. P. Wohlfarth, Philosophical Transactions of the Royal Society of London Series a-Mathematical and Physical Sciences **240**, 599 (1948).

[53] W. C. Elmore, Physical Review **53**, 757 (1938).

[54] W. F. Brown, Journal of Applied Physics **49**, 1937 (1978).

[55] W. F. Brown, Physical Review **105**, 1479 (1957).

[56] R. H. Victora, Physical Review Letters **58**, 1788 (1987).

[57] L. Straka, O. Heczko, and N. Lanska, IEEE Transactions on Magnetics **38**, 2835 (2002).

[58] O. Heczko, L. Straka, N. Lanska, K. Ullakko, and J. Enkovaara, Journal of Applied Physics **91**, 8228 (2002).

[59] S. Ghosh and B. Sanyal, Journal of Physics-Condensed Matter **22**, 346001 (2010).

[60] P. Lazpita, J. M. Barandiaran, J. Gutierrez, J. Feuchtwanger, V. A. Chernenko, and M. L. Richard, New Journal of Physics **13**, 033039 (2011).

[61] A. Diestel, V. Neu, A. Backen, L. Schultz, and S. Fahler, Journal of Physics-Condensed Matter **25**, 266002 (2013).

[62] A. DeSimone and R. D. James, Journal of the Mechanics and Physics of Solids **50**, 283, Pii s0022-5096(01)00050-3 (2002).

[63] O. Heczko, Journal of Magnetism and Magnetic Materials **290**, 846 (2005).

[64] V. A. Chernenko, V. A. L'Vov, P. Mullner, G. Kostorz, and T. Takagi, Physical Review B **69**, 134410 (2004).

[65] V. A. L'Vov, E. V. Gomonaj, and V. A. Chernenko, Journal of Physics-Condensed Matter **10**, 4587 (1998).

[66] A. A. Likhachev and K. Ullakko, European Physical Journal B **14**, 263 (2000).

[67] A. Likhachev and K. Ullakko, Journal of Magnetism and Magnetic Materials **226**, 1541 (2001).

[68] A. A. Likhachev and K. Ullakko, Journal De Physique Iv **11**, 293 (2001).

[69] N. Sarawate and M. Dapino, Applied Physics Letters **88**, ARTN 121923 (2006).

[70] N. Sarawate and M. Dapino, Ieee Transactions on Magnetics **44**, 566 (2008).

[71] N. Sarawate and M. Dapino, Applied Physics Letters **93**, ARTN 062501 (2008).

[72] N. Sarawate and M. Dapino, Smart Materials & Structures **18**, ARTN 104014 (2009).

[73] M. R. Sullivan and H. D. Chopra, Physical Review B **70**, 094427 (2004).

[74] Y. W. Lai, N. Scheerbaum, D. Hinz, O. Gutfleisch, R. Schafer, L. Schultz, and J. McCord, Applied Physics Letters **90**, 192504 (2007).

[75] O. Heczko, K. Jurek, and K. Ullakko, Journal of Magnetism and Magnetic Materials **226**, 996 (2001).

[76] V. A. Chernenko, R. L. Anton, M. Kohl, J. M. Barandiaran, M. Ohtsuka, I. Orue, and S. Besseghini, Acta Materialia **54**, 5461 (2006).

[77] V. Golub, K. M. Reddy, V. Chernenko, P. Mullner, A. Punnoose, and M. Ohtsuka, Journal of Applied Physics **105**, 07a942 (2009).

[78] A. M. Jakob, M. Hennes, M. Mueller, D. Spemann, and S. G. Mayr, Advanced Functional Materials **23**, 4694 (2013).

[79] Q. Pan and R. D. James, Journal of Applied Physics **87**, 4702 (2000).

[80] M. De Graef, Y. Kishi, Y. Zhu, and M. Wuttig, Journal De Physique Iv **112**, 993 (2003).

[81] A. Budruk, C. Phatak, A. K. Petford-Long, and M. De Graef, Acta Materialia **59**, 4895 (2011).

[82] M. De Graef, M. A. Willard, M. E. McHenry, and Y. M. Zhu, IEEE Transactions on Magnetics **37**, 2663 (2001).

[83] C. Mennerich, F. Wendler, M. Jainta, and B. Nestler, European Physical Journal B **86**, 171 (2013).

[84] T. Koyama, Science and Technology of Advanced Materials **9**, 013006 (2008).

[85] L. Daniel, O. Hubert, N. Buiron, and R. Billardon, Journal of the Mechanics and Physics of Solids **56**, 1018 (2008).

[86] S. Conti, M. Lenz, and M. Rumpf, Journal of the Mechanics and Physics of Solids **55**, 1462 (2007).

[87] S. Conti, M. Lenz, and M. Rumpf, Materials Science and Engineering a-Structural Materials Properties Microstructure and Processing **481**, 351 (2008).

[88] C. M. Landis, Journal of the Mechanics and Physics of Solids **56**, 3059 (2008).

[89] M. Luskin and T. Zhang, Computer Methods in Applied Mechanics and Engineering **196**, 3759 (2007).

[90] Y. M. Jin, Acta Materialia **57**, 2488 (2009).

[91] Y. M. Jin, Applied Physics Letters **94**, 062508 (2009).

[92] Y. M. Jin, Philosophical Magazine **90**, 169 (2010).

[93] Y. M. Jin, Applied Physics Letters **99**, 062507 (2011).

[94] J. X. Zhang and L. Q. Chen, Philosophical Magazine Letters **85**, 533 (2005).

[95] N. Gabdullin and S. H. Khan, Ieee Transactions on Magnetics **53**, 4900108 (2017).

[96] K. Haldar, B. Kiefer, and D. C. Lagoudas, Philosophical Magazine **91**, 4126 (2011).

[97] Q. Peng, J. J. Huang, and M. X. Chen, Materials & Design **107**, 361 (2016).

[98] D. X. Chen, E. Pardo, and A. Sanchez, IEEE Transactions on Magnetics **41**, 2077 (2005).

[99] S. K. Wu and S. T. Yang, Materials Letters **57**, 4291 (2003).

[100] V. A. Chernenko, Scripta Materialia **40**, 523 (1999).

[101] X. Jin, M. Marioni, D. Bono, S. M. Allen, R. C. O'Handley, and T. Y. Hsu, Journal of Applied Physics **91**, 8222 (2002).

[102] M. Richard, J. Feuchtwanger, D. Schlagel, T. Lograsso, S. M. Allen, and R. C. O'Handley, Scripta Materialia **54**, 1797 (2006).

[103] R. Niemann, U. K. Rossler, M. E. Gruner, O. Heczko, L. Schultz, and S. Fahler, Advanced Engineering Materials **14**, 562 (2012).

[104] V. V. Kokorin, V. V. Martynov, and V. A. Chernenko, Scripta Metallurgica Et Materialia **26**, 175 (1992).

[105] N. Lanska, O. Soderberg, A. Sozinov, Y. Ge, K. Ullakko, and V. K. Lindroos, Journal of Applied Physics **95**, 8074 (2004).

[106] D. Lagoudas, Shape Memory Alloys: Modeling and Engineering Applications (Springer, College Station, 2008).

[107] M. S. Wechsler, D. S. Lieberman, and T. A. Read, Transactions of the American Institute of Mining and Metallurgical Engineers **197**, 1503 (1953).

[108] J. S. Bowles and J. K. Mackenzie, Acta Metallurgica **2**, 129 (1954).

[109] J. P. Hirth and J. Lothe, *Theory of Dislocations* (McGraw-Hill Book Company, New York, 1968).

[110] J. W. Christian and S. Mahajan, Progress in Materials Science **39**, 1 (1995).

[111] A. Sozinov, N. Lanska, A. Soroka, and L. Straka, Applied Physics Letters **99**, 124103 (2011).

[112] D. Kellis, A. Smith, K. Ullakko, and P. Muellner, Journal of Crystal Growth **359**, 64 (2012).

[113] L. Straka, O. Heczko, H. Seiner, N. Lanska, J. Drahokoupil, A. Soroka, S. Fahler, H. Hanninen, and A. Sozinov, Acta Materialia **59**, 7450 (2011).

[114] L. Straka, H. Hanninen, and O. Heczko, Applied Physics Letters **98**, 141902 (2011).

[115] L. Straka, A. Soroka, H. Seiner, H. Hanninen, and A. Sozinov, Scripta Materialia **67**, 25 (2012).

[116] O. Heczko, V. Kopecky, A. Sozinov, and L. Straka, Applied Physics Letters **103**, 072405 (2013).

[117] P. Lindquist and P. Müllner, Shape Memory and Superelasticity (2015).

[118] A. Aharoni, Journal of Applied Physics **83**, 3432 (1998).

[119] L. Straka, H. Hanninen, N. Lanska, and A. Sozinov, Journal of Applied Physics **109**, 063504 (2011).

[120] R. C. Pond, B. Muntifering, and P. Muellner, Acta Materialia **60**, 3976 (2012).

[121] B. Muntifering, R. C. Pond, L. Kovarik, N. D. Browning, and P. Muelliner, Acta Materialia **71**, 255 (2014).

[122] B. Muntifering, Bochum, 2014.

[123] B. Muntifering, L. Kovarik, N. D. Browning, R. C. Pond, W. B. Knowlton, and P. Muellner, Journal of Materials Science **51**, 457 (2016).